Title
Integration of Bioassays on Microfluidic Platforms and Analysis of Detection Performance

Author
Bauer, Maria Elisabeth

Publication Date
2019

UNIVERSITY OF CALIFORNIA,
IRVINE

Integration of Bioassays on Microfluidic Platforms and Analysis of Detection Performance

DISSERTATION

submitted in partial satisfaction of the requirements
for the degree of

DOCTOR OF PHILOSOPHY

in Mechanical and Aerospace Engineering

by

Maria Elisabeth Bauer

Dissertation Committee:
Professor Marc J. Madou, Chair
Professor Lawrence Kulinsky
Professor J. Michael McCarthy

2019

TABLE OF CONTENTS

LIST OF FIGURES vi

LIST OF TABLES xi

ACKNOWLEDGMENTS xii

CURRICULUM VITAE xiii

ABSTRACT OF THE DISSERTATION xv

1. Introduction – Point of Care Diagnostics 1

2. Comparison of Methods for Detection of HRP 3

    2.1. Need for (improved) Diagnosis in View of Drug Resistance 3

    2.2. Background on HRP Detection 5

    2.3. Materials and Methods for Detection of HRP 6

        2.3.1. Absorbance Measurements 7

        2.3.2. Chemiluminescence Measurements 7

        2.3.3. Amperometric Measurements 8

        2.3.4. Calculation of LOD, Sensitivity, DR 8

    2.4. Results of HRP Detection – Absorbance, Chemiluminescence, Amperometry 9

3. Prototyping of a Diagnostic Platform and Demonstration via Malaria Immunoassay 13

    3.1. Background 13

        3.1.1. Lab-on-Chip Platforms 13

        3.1.2. Lab-on-Chip Devices for POC based on Molecular Detection and Immunoassays 14

        3.1.3. 3D Printing for LOC Devices 15

    3.2. Materials and Methods 20

- 3.2.1. Components and Operation Principle 20
- 3.2.2. Control and Electronics 26
- 3.2.3. ELISA Steps and Implementation 28
- 3.3. Results & Discussion 31
  - 3.3.1. Optimization of FDM Print Settings 31
  - 3.3.2. Postprocessing for Leakage Reduction 34
  - 3.3.3. Colorimetric Malaria-ELISA Test Results 36
- 3.4. Conclusions 37

4. CD Microfluidics 40
- 4.1. Burst Valves 40
  - 4.1.1. Introduction to Burst Valves on the CD 40
  - 4.1.2. Burst Model 42
  - 4.1.3. Experimental Methods 46
    - 4.1.3.1. Fabrication of Channels 46
    - 4.1.3.2. Molding of Burst Valve Geometry 48
    - 4.1.3.3. Measurement of Contact Angles 49
    - 4.1.3.4. Measurement of Burst Frequencies 50
    - 4.1.4. Results and Discussion 51
    - 4.1.4.1. Comparison of Predicted and Experimental Burst Frequencies 51
    - 4.1.4.2. Discussion of Factors influencing Burst Pressure 55
  - 4.1.5. Conclusion 63
- 4.2. Laser Valve 65
- 4.3. Fluid Reciprocation 67
  - 4.3.1. Introduction 67

4.3.2. Materials and Methods 70

4.3.3. Results and Discussion 71

4.3.4. Conclusions 79

5. Electrochemistry on the CD 80

5.1. Basics of Electrochemical Sensing 80

5.1.1. Amperometry 80

5.1.2. Cyclic Voltammetry 81

5.1.3. Microelectrodes 84

5.2. Effect of Flow on Electrochemical Signal 86

5.2.1. Introduction - Detection on CD Microfluidic Platform 86

5.2.2. Background 86

5.2.2.1. Current Methods for Interfacing Electrodes on a Microfluidic CD 86

5.2.2.2. Redox Cycling Amplification using Interdigitated Microelectrode Arrays 88

5.2.3. Materials and Methods 90

5.2.3.1. Microfluidic Disc Design and Fabrication 90

5.2.3.2. Setup for Rotating Electrochemical Measurements 92

5.2.3.3. Procedures for Electrochemical Measurements 92

5.2.3.1. Data Analysis 94

5.2.4. Results and Discussion 96

5.2.4.1. Stationary Electrochemical Sensor Performance 96

5.2.4.2. Effect of Flow Velocity on Redox Cycling 100

5.2.4.3. Flow-enhanced Electrochemical Sensor Performance 101

5.2.5. Conclusion 103

6. Demonstration of Malaria Assay on the CD 105

6.1. Integration of Sample-to-Answer Malaria-Assay on the CD 105

6.1.1. Assay Procedure 105

6.1.2. Integration of the Assay Steps on the CD 106

6.2. Results and Discussion 110

7. Conclusions 113

REFERENCES 117

LIST OF FIGURES

Figure1: Calibration Curves for absorbance, chemiluminescence and amperometric detection of HRP 11

Figure 2: a) Flashforge Original Creator, the fused deposition modeling (FDM) system used for building devices in this work. b) Principle of material extrusion: Thermoplastic filament is heated while extruded through a nozzle onto the build plate. It re-solidifies as it cools down, and after the build plate is lowered, the next layer is deposited atop, thus forming the desired geometry. 18

Figure 3: First design moving fluid through enclosed channels by servomotor actuation controlled from a smartphone audio jack. 22

Figure 4: Second design powered by portable battery and controlled via smartphone. The design implements fluid actuation, lighting, incubation (heating and temperature control). a) Major dimensions of prototype in mm. b) Printed cartridge with colored water. c) Reusable frame holding electronics. d) Fully assembled device with electronics connected to portable battery and audio outlet of smartphone. 23

Figure 5: a) Top view of the third prototype incorporating a 3D-printed set of racks, gears and waste syringes (two waste syringes are stacked one atop the other). b) Side view of the third prototype (gears, motors and syringes are removed to facilitate the clear view of the fluidic platform). 25

Figure 6: LED backlighting for readout; empty cartridge. 28

Figure 7: Schematic malaria ELISA steps. Test wells contained in the malaria kit are precoated with specific antigens. Primary antibodies (present in infected blood due to a patient's immune reaction to malaria pathogens) bind to antigens. Secondary antibodies (contained in malaria conjugate) are employed for optical detection as they are conjugated to the enzyme, effecting the color change of the solution after TMB substrate is added. The presence or absence of the color change of the solution in the detection wells is evaluated after the stop solution is added. 29

Figure 8: Printed part with leakages showing red. Dyed water marks the hexagonal infill structures filled with water through leakages from chambers and enclosed channels into the part. 31

Figure 9: Top: Test cubes with leakage after submerging in dyed water. Bottom: Major dimensions of test cubes in mm. Channel C is inclined 75° with respect to the side of the cube. Channels have elliptical cross sections (major axis (mm) × minor axis (mm)): A, C: 3 × 1.5, B: 2 × 1, D: 4 × 2. 33

Figure 10: 3D-printed device with colorimetric malaria ELISA. a) Laser-cut lid to hold tubes for emptying of wells. b) Colorimetric results after application of stop solution. Left: negative control well, middle: blank well, right: positive control well. 37

Figure 11: a) Channel layout on tested parts and widths of channels with nominal channel width in mm. Channel widths subscript relates to distance of the valve from the center with subscript i indicating a distance between center and channel inlet of 20mm, subscript m indicating a distance of 30mm and subscript o indicating a distance of 40mm; b) Variables in burst frequency calculation; c) Schematic of burst scenarios with (left to right) burst dependent on liquid entering the channels, liquid creeping into the channel along imperfections, and burst dependent on liquid overcoming capillary holding forces at the channel outlet 45

Figure 12: Optical microscope images of channel $.25_m$ in PMMA CNC milled disc with dyed 1xPBS solution right before burst in parts with a) no radius at channel ends b) 400µm radius at channel ends; resulting expansion angles, β and width, w^* 47

Figure 13: Process for producing molded parts of this work: left to right – 3D Model of mold components, machining of physical mold, molding of plastic granules plastic injector, measurement and analysis of molded parts 49

Figure 14: Maximum predicted burst frequency in RPS and respective experimental results for PMMA and PC parts, CNC milled and rapid injection molded 53

Figure 15: Pressures for fluid flow through channels in rapid injection molded PMMA part, channel $.75_i$; C.M.: Burst pressure based on fluid front at channel middle according to Equation 4, EXP: Experimentally obtained, averaged burst pressure, C. I.: Burst pressure according to Equation 5, C.O.: Burst pressure according to Equation 6 54

Figure 16: Predicted burst frequency in RPS and experimental results for channels on PMMA and PC parts, CNC milled, and rapid injection molded. Predicted values are based on Equation 7 55

Figure 17: Average experimental burst pressure for tested parts with error bars representing the range of burst pressures for varying channel widths 57

Figure 18: Example of PMMA rapid injection molded part: Influence of replacement of the adhesive cover with a PMMA rapid injection molded cover 58

Figure 19: a) Effect of decrease in widths for parts with constant channel depth of 0.1mm onto burst pressure. Calculation based on PC rapid injection molded part; b) Effect of decrease in channel height with constant channel widths of 0.1mm; Decrease in height has more effect due to hydrophobic top adhesive 59

Figure 20: Surface Profile of channel E in a PMMA CNC machined and a PP rapid injection molded part measured with confocal microscope VK-X200K, Keyence, Corp.) 62

Figure 21: Principle of laser valves, energy from a laser transmits clear layers and is absorbed by a black thin film, melting a hole in the latter and allowing fluid to pass. 67

Figure 22: Basic principle of air compression chamber for reciprocation of fluid on a microfluidic disc 69

Figure 23: Embedded rubber-like membrane. Embedding the second material component was necessary to avoid delamination. 72

Figure 24: Three different reciprocation inserts are shown as mounted on the spin stand (the largest dimension of the inserts is between 4-6 cm): a) Reciprocation insert based on compression of air and elastic deformation of rubber-like membrane; b) Straight-channel reciprocation insert to decouple printed micro-balloon performance; c) Mixing coupon allowing for mixing of two components and reciprocation of the mixture until expelled via a siphon to a waste chamber. 73

Figure 25: Channel of the mixing insert (as shown in Figure 24c) orange marks show locations of increased liquid interchange between merging and separating channels; a) Major dimensions of the mixing channel [in mm], b) Water flow path during reverted flow simulation at a 200µL/min flow rate, yellow marks show locations with less liquid interchange between merging channels (compare over-crossing of green lines) 73

Figure 26: Minimal fatigue of rubber-like material after 25 reciprocation cycles: a) Fluid position when spinning at 200RPM, 750RPM and 1000RPM respectively; b) Reciprocation repeated between 700RPM and 1000RPM over 25 cycles. Fluid position is indicated with red line; c) Fluid position at 200RPM before and after 25 cycles between 700 and 1000RPM. Only minimal fatigue observed 75

Figure 27: 3D images of the 3D printed surfaces, a) VeroWhite, glossy, b)VeroWhite, matte, c) TangoBlack, glossy, d) TangoBlack matte. 76

Figure 28: Burst frequency testing of 3D printed inserts with glossy and matte surface finish. a) inserts with different surface finish in laser-cut acrylic holder; b) Naming convention of channels with decreasing channel widths left to right; 5c Average burst frequencies for channels A through E. Channel E did not print in glossy surface finish part due to limited resolution. d) Graph of burst frequency depending on channel width. Blue/round is burst frequency of glossy and orange/triangular symbols indicate burst frequency of matte part. Error bars represent standard deviation. Number of tests for each channel was 10 and volume of deionized, dyed water per channel was 20uL 78

Figure 29: a) Amperometry: applied potential step and resulting current profile, b) Cyclic voltammetry: applied potential sweep and resulting current profile (at slow scan rates) 82

Figure 30: Cyclic Voltammogram of TMB, blue line shows two electron transfer (two peaks) of TMB^{+} (TMB blue) while the yellow curve shows one electron transfer voltammogram after adding stop solution to TMB^{+}, thus redox cycling of TMB^{2+} (TMB yellow) 83

Figure 31: a) radial diffusion to a microelectrode, b) quasi planar diffusion to a macroelectrode, blue arrows indicate direction of diffusion, black lines areas of constant concentration. 84

Figure 32: a) Fluidics on CD and positioning of the electrode underneath the disc, b) Assembly of modular CD. Electrodes can be removed for cleaning and replacement, c) Test setup for non-contact measurements 91

Figure 33: Single and dual mode CVs for a) Platinum IDA and b) carbon IDA, c) Single mode CV for platinum IDA with concentrations 1mM through 9mM ferricyanide, ferrocyanide redox-couple, d) Dual mode CV for platinum IDA with concentrations 1mM through 9mM ferricyanide, ferrocyanide redox-couple. 98

Figure 34: Calibration curve for single and dual mode, platinum IDA, stationary measurements 99

Figure 35: a) Single mode platinum IDA CV for increasing flowrates, b) Dual mode CV for platinum IDA for different flowrates. The baseline was subtracted from curves in dual mode for better visibility of the current increase with increasing flowrate 100

Figure 36: a) Relation between angular frequency and flow rate, b) Calculated (blue) and experimental Single Mode currents for increasing flow rate (platinum IDA), c) Measured RA versus flow rate (Platinum IDA), d) Measured CE versus flow rate (platinum IDA) 101

Figure 37: a) Disc assembly with black adhesive layer to enable use of laser valves, b) assembled disc with dyed water in reagent chambers (green is reaction chamber with break apart, pre-coated detection well), c) model of disc layout. 108

Figure 38: High speed images of critical steps: a) sample incubation, b) first wash, c) incubation of malaria conjugate (primary antibody), d) second wash, e) incubation TMB substrate, f) electrochemical detection during flow 109

Figure 39: a) On disc amperometric results for blank, negative control, cut-of control, and positive control, b) comparison of on disc and off the disc currents 110

LIST OF TABLES

Table 1: Performance characteristics of evaluated detection methods 10

Table 2: ELISA steps implemented on the 3D-printed automated bioassay platform. 30

Table 3: Optimization of print settings for the Flashforge Original Creator using 1.75mm acrylonitrile butadiene styrene (ABS) filament. Geometry is qualitatively categorized into three types: large deformations (--), small deformations (-), negligible deformations (+). 32

Table 4: Contact angle measurements of different surface treatments of FDM-printed ABS parts. 36

Table 5: Contact angle measurements in degrees with 1x phosphate-buffered saline (PBS) solution (Drop Shape Analyzer DSA25, Kruess GmbH); Standard deviations in measurements are indicated in parenthesis 50

Table 6: Standard Deviations of experimental burst frequencies within part groups 56

Table 7: Surface roughness and contact angles of printed materials 77

Table 8: Stationary measurements in dual and single mode on platinum and carbon IDAs 97

Table 9: Single versus dual mode sensitivities and LOD for platinum IDA under flow 102

Table 10: Comparison of predicted and measured currents in dual mode at spin speed of 400RPM at various concentrations 103

Table 11: CV for different assay integration levels 111

ACKNOWLEDGMENTS

I would like to express my gratitude to my committee chair, Professor Marc Madou, who has not only given me the opportunity to join and research in the BioMEMS lab but also enabled me to gain valuable experience in industry throughout my studies. In addition, I would like to thank my committee members Professor Lawrence Kulinsky and Professor J. Michael McCarthy for their valuable advice and guidance with this thesis. Professor Marc Madou and Professor Lawrence Kulinsky not only advised my thesis but together with Ed Tacket introduced me to my field of research.

During the past years I had the pleasure to work with a number of talented aspiring researchers including Sepehr Haerian, Adrian Bahani, Tracy Ogata, Maria Caicedo, Daniel Schuder, Jaume Bartoli and Marzieh Ataei. Thanks to you for your hours of dedication and hard work. Furthermore, I thank Professor Michelle Khine and Professor Rufus D. Edwards for allowing me to use their equipment for micro-characterization and optical detection respectively and Michael Chu, Lancy Lin, and Jessica Monterrosa Mena for their help and time setting up equipment.

I am grateful for all partners at university and in industry who not only helped to fund my work but also allowed me to enhance academic education with practical experience while always allowing me the flexibility to conduct my studies.

Finally, I thank Springer Verlag and MDPI for permission to include published material in my dissertation.

CURRICULUM VITAE

EDUCATION

2019 Ph.D. in Mechanical and Aerospace Engineering, University of California Irvine
2014 M.Sc. in Mechanical Engineering and Management, Technical University of Munich, Germany
2012 B.Sc. in Mechanical Engineering and Management, Technical University of Munich, Germany

EXPERIENCE

Since 2019: Program Manager 2018-2019: Project Engineer	Design West Technologies, Inc., Tustin
2018-2019: Graduate Student Researcher	Nexus Dx, San Diego
2017-2018: Product Development Engineer 2016-2017: Graduate Student Researcher	Toolbox Medical Innovations, Inc., Carlsbad
2018: Teaching Assistant	Computer Aided Engineering, University of California Irvine
2016 & 2018: Teaching Assistant	Advanced Manufacturing Choices, University of California Irvine
2015-2016: Graduate Student Researcher 2014: Junior Specialist	RapidTech, Irvine
2011-2012: Student Trainee 2010-2011: Engineering Intern	MAN Truck & Bus AG, Munich, Germany
2008: Manufacturing Intern	gabo Systemtechnik GmbH, Niederwinkling, Germany

PUBLICATIONS

2019	Submitted to Instruments, Maria Bauer, Jaume Bartoli, Daniel Schuder, Marc Madou, “Comparison of common Detection Methods for HRP Label and Demonstration via Amperometric Malaria Assay on the Microfluidic CD “
2019	Submitted to Micromachines, Maria Bauer, Adrian Bahani, Tracy Ogata, Marc Madou, “3D printing of Elastic Membranes for Fluidic Pumping”
2019	Maria Bauer, Marzieh Ataei, Maria Caicedo, Kirsten Jackson, Marc Madou, Luc Bousse, “Burst valves for commercial microfluidics: a critical analysis” Microfluidics and Nanofluidics
2019	Maria Bauer, Jaume Bartoli, Sergio O. Martínez-Chapa, Marc Madou, “Wireless Electrochemical Detection on a Microfluidic Compact Disc (CD) and Evaluation of Redox-Amplification during Flow” Micromachines
2019	Mohammad Mahdi Aeinehvand, Laura Weber, Martín Jiménez, Andrea Palermo, Maria Bauer, Felix F. Loeffler, Fatimah Ibrahim, Frank Breitling, Jan Korvink, Marc Madou, Dario Mager, Sergio O. Martínez-Chapa, “Elastic reversible valves on centrifugal microfluidic platforms” Lab on a Chip
2018	Maria Bauer, Lawrence Kulinsky, “Fabrication of a Lab-on-Chip Device Using Material Extrusion (3D Printing) and Demonstration via Malaria-Ab ELISA” Micromachines

ABSTRACT OF THE DISSERTATION

Integration of Bioassays on Microfluidic Platforms and Analysis of Detection Performance

By

Maria Elisabeth Bauer

Doctor of Philosophy in Mechanical and Aerospace Engineering

University of California, Irvine, 2019

Professor Marc J. Madou, Chair

Life-saving treatment starts with proper diagnosis. This thesis therefore discusses two central aspects: detection methods and integration of fluidic steps onto fully automated diagnostic platforms. To investigate performance of different common commercial detection methods with regard to detection characteristics, such as limit of detection (LOD), sensitivity, and dynamic range (DR), horseradish peroxidase (HRP) was chosen as label and detection was conducted via absorbance, chemiluminescence, and amperometry. While these performance parameters vary for different substrates and depend on specific procedure for each technique, the importance of choosing the proper detection method for a given application is conspicuous. Integration of a colorimetric, HRP-based enzyme-linked immunosorbent assay (ELISA) for detection of malaria is demonstrated on a rapid prototyped platform (3D printed microfluidic structure) and electrochemical detection is integrated on a compact disc (CD) microfluidic device. The latter is most commonly produced via injection molding and thus compatible with mass manufacturing. While CD microfluidics excels in simplicity of pumping principle based on centrifugal force from a single motor and elegance of instrumentation-free, passive valving based on changing capillary forces at cross-section changes (burst valves), this type of valving often shows unreliable. Burst valves are therefore analytically modelled and experimentally analyzed and evaluated. While instrumentation-free principle incites their application, control of burst pressure underlies effects of surface imperfections and dimensional control is critical. While pumping on CD microfluidic platforms inherently enables fluid motion towards the outer perimeter of the disc, reversed flow is demonstrated on material jetted CD-inserts.

Integration of electrochemical detection on the CD, allows for signal amplification via enhanced mass transport. The effect of flow onto electrochemical measurements is investigated in cyclic voltammetry experiments on Interdigitated Electrode Arrays (IDAs) on the CD. While flow generally increases mass transport to the electrode surface, redox amplification suffers. Nevertheless, dual mode cyclic voltammetry during flow results in lowest LOD.

1. Introduction – Point of Care Diagnostics

There is much need and a growing market (expected to reach $22.8 billion by 2025[1]) for improved Point of Care (POC) diagnostics. It spans from so called Extreme Point of Care (EPOC) medicine as for example in the case of rural areas of the developing world without access to laboratory diagnostics[2], to emergency medicine, e.g. portable systems for first responders to initiate fast diagnosis on the spot[3]. Especially in the case of emergency medicine, a condition might still be in an early phase, thus requiring a diagnostic with very low LOD/very high sensitivity for the specific biomarkers. An example for POC diagnosis of biomarkers, benefitting from detection at very early stages, is the detection of Troponin T and I (found in heart muscle fibers) as marker for cardiac arrest[45]. While coronary heart disease and stroke lead the list of causes of deaths across countries of all income classes, infectious diseases such as human immunodeficiency virus (HIV)/acquired immunodeficiency syndrome (AIDS), tuberculosis and malaria are still amongst the top ten causes of deaths in countries of low income, while being a much smaller burden in the developed world[6]. In either scenario proper and early diagnosis is essential for effective and targeted treatment. The ideal diagnostic approach will depend on specific requirements (e.g. expected biomarker concentration, concentration range, acceptable time to result, error, and cost).

The motivation of this research is to contribute to improving diagnostics and making them available to a broader audience, while leveraging advances in manufacturing and microfabrication. This thesis therefore evolves around two central aspects, biomarker detection methods and integration of complete bioassays onto fully automated platforms. Principles and solutions in the fields of microfluidics are investigated, with focus on but not limited to CD microfluidics and means of detection. Especially highlighted is the use of electrochemical diagnostics and a comparison to more commonly used optical detection. Furthermore, prototyping techniques such as 3D printing and manufacturing methods such as injection molding and their impact on the function of these microfluidic devices are discussed. Finally, integration and benefits from integration of electrochemical sensing on CD microfluidic platforms are demonstrated.

2. Comparison of Methods for Detection of HRP

2.1. Need for (improved) Diagnosis in View of Drug Resistance

To allow for proper treatment of a vast number of health conditions, prior diagnosis is indispensable. Targeted treatment is especially crucial with regard to the rapidly increasing drug resistance of various pathogens. Of the 10.4 million infections with tuberculosis in 2016, 600,000 were caused by drug resistant bacteria[7]. Mortality rates for multi-drug-resistant and extensively drug-resistant tuberculosis are 40% and 60% respectively, contributing to a total of 1.7 million tuberculosis fatalities in 2016[7,8]. In the case of malaria, drug resistance against chloroquine treatment developed and spread within a decade after market introduction of the drug, eventually leading to practically all malaria causing parasites being resistant[9,10]. Replacing chloroquine treatment with artemisinin-based combination therapies (ACTs) against malaria, contributed largely to the decreasing global malaria mortality by 30% between 2010 and 2015[11]. However, around 2007 the new treatment of ACTs began to provoke drug resistant mutations of Plasmodium falciparum (the parasite, responsible for the most severe infections and highest number of fatalities), which is especially worrisome as no viable alternative treatment is yet available[11]. Besides drug-related considerations, including the rapidly decaying effect of the drug[12,13], more targeted treatment has enormous potential[14]. Especially in areas of high prevalence of a specific disease, treatment is commonly commenced without prior diagnosis of the pathogen and solely based on symptoms[15]. Besides the high prevalence of malaria in endemic areas, fear of the high mortality due to malaria, especially in young children, fuels overtreatment[15]. A similar scenario exists in the case of tuberculosis in high-incidence countries, where access to proper diagnostics such as sputum smear microscopy is oftentimes poor, leaving symptom-based treatment as the only option. Moreover, many other infections commonly found in the same geographic areas show similar symptoms (e.g. pneumonia shows similar symptoms to malaria and can be deadly[15]). Thus, symptom-based treatment does not only lead to increased drug resistance but may also thwart patients from receiving targeted and possibly life-saving treatment for the actual cause of their symptoms.

The gold standard for diagnostics for infectious diseases like malaria or tuberculosis are immunoassays such as enzyme-linked immunosorbent assays (ELISA)[16,17]. These tests have not only high specificity and sensitivity[16,17], but also allow for fast diagnosis within hours, compared to days, as is the case for diagnosis based on pathogen cultures[18]. Furthermore, preparing costly cultures, which require well equipped laboratories with controlled environmental conditions, is not an option in resource-limited areas which are especially burdened by these diseases[18]. To increase affordability and make ELISA testing of infectious diseases suitable for low-resource settings, integration of ELISA technology into POC devices, which follow the ASSURED (affordable, sensitive, specific, user-friendly, rapid and robust, equipment-free, deliverable to end-users) criteria as defined by the World Health Organization (WHO), is needed to provide proper and timely diagnosis[19–21]. While dipstick tests are highly desirable for POC settings due to their simplicity, low cost and ease-of-use[21], they cannot always provide the sensitivity and quantifiability that is needed[22]. Common dipstick tests employ visual evaluation of a color change based on a chemical reaction, while other handheld and/or portable devices allow for quantifiable detection based on chemical reactions causing a change in absorbance measurement, fluorescent, luminescent, or electrochemical signal. Such information allows for high sensitivity, low LOD and a quantitative result which is independent from human interpretation.

For the design of a highly sensitive and specific assay with the desired LOD, sensitivity and DR, we start by evaluating the detectability of the label with the desired detection system. Only with the label confirmed at the expected concentration range, additional assay steps including its attachment to antibodies should be investigated to tailor a diagnostic procedure to the needed precision and detection window of the assay. We therefore present a comparison of the signals obtained from different optical and electrochemical detection methods with commercial systems for the most commonly used plant-based enzyme HRP[23]. The advantage of utilizing HRP as the label for this comparison is that it can be detected optically as well as electrochemically, thus allowing for a comparison of detection performance of the different techniques for the same label. While the substrates and experimental procedures affect properties of the detection methods, we evaluate the detection method performance based on commonly available commercial platforms.

As the detection method alone does not suffice for diagnosing a disease in POC situations, automated detection of malaria, labelled with HRP is demonstrated on a 3D printed platform and on a CD microfluidic platform. These platforms are described in Section 3 and Section 6 respectively.

2.2. Background on HRP Detection

Many common optical (e.g. absorbance[24], chemiluminescence[25]) as well as electrochemical[26] immunoassays use the plant-based enzyme HRP to obtain a signal. While direct electrochemical detection of HRP has been demonstrated with different electrodes and methods[27–29] the most commonly used method uses the chromogen 3,3′,5,5′-Tetramethylbenzidine (TMB) which is oxidized by HRP/hydrogen peroxide[30] to TMB^{+} from a clear to a blue state and hence, cannot only be detected electrochemically, but also through absorbance measurements at a wavelength of 370 and 652nm. A further oxidation state, TMB^{2+} is stable under acidic conditions (pH<1), thus adding an acid (e.g. H_2SO_4) to TMB^{+} yields, besides the emission of an electron, a color change from any developed blue (TMB^{+}) to yellow (TMB^{2+}), with an absorbance peak at 450nm[31,32]. Yet another detection method applicable to HRP quantification is chemiluminescence, which is based on the HRP-catalyzed oxidation of luminol by hydrogen peroxide under emission of light. An enhancer is oftentimes used to increase the intensity and duration of light emission[33]. Nelson[34] et al. compare the LOD for detection of HRP and evaluate respective DR for different methods. While the LODs for absorbance and chemiluminescence are similar at 3-6pg/mL and 1-3pg/mL respectively, DR varies widely depending on the substrate used. Fanjul-Bolado[23] et al analyze the LOD for amperometric detection of HRP with a result of 0.88pg/mL. While the LOD is a deciding criterion for assays that need to be able to detect very low concentrations, the DR may be just as important to consider in order to avoid the need for prescreening and sample dilution which could significantly increase detection complexity and time to result.

2.3. Materials and Methods for Detection of HRP

Three different methods of detection HRP were compared: absorbance, chemiluminescence, and amperometry. HRP solutions of 30 different concentrations were obtained through serial dilution with deionized (DI) water from a 0.05mg/mL starting solution prepared from lyophilized HRP powder (Santa Cruz, Inc. Dallas, TX, USA) in DI water. The solutions were either used immediately or stored frozen for further use after a single freeze thaw cycle. Furthermore, the pH level was checked before usage and found to be approximately 5 for all solutions. All optical readings were processed via SoftMax Pro 6 Software (Molecular Devices,LLC, San Jose, CA, USA) and all tests in this paper were repeated 3 times to obtain average measurements and standard deviations.

2.3.1. Absorbance Measurements

For absorbance measurements, 20µL of HRP solutions of different concentrations were pipetted in triplets into the wells of a clear 96 well plate. 80µL of TMB substrate solution (Thermo Fisher Scientific, Waltham, MA, USA) were added and the solutions were allowed to incubate for 15 minutes in the dark. Stop solution (1N sulfuric acid, IBL-International, Corp., Hamburg, Germany) was added to all wells to stop the reaction. Absorbance measurements were then conducted on a VersaMax ELISA Microplate Reader (Molecular Devices,LLC, San Jose, CA, USA) by reading absorbance measurements of TMB^{2+} (yellow) at a wavelength of 450nm.

2.3.2. Chemiluminescence Measurements

For the chemiluminescence measurements 20µL of the HRP solutions were pipetted in triplets into white opaque 96 well plates and 80µL of Luminol-and-Enhancer Solution as well as 80µL of Hydrogen Peroxide Solution (both from Super Signal West Femto kit, Thermo Fisher Scientific, Waltham, MA, USA) were added to each well. Luminescence readings were started after 5 minutes of incubation at room temperature and conducted on a Gemini XPS Microplate Reader (Molecular Devices,LLC, San Jose, CA, USA).

2.3.3. Amperometric Measurements

A portable Bluetooth enabled bipotentiostat (uStat400, Metrohm Dropsens, Asturias, Spain) was used for amperometric measurements as this allowed for the integration of electrochemical read-out while spinning the CD platform on a custom-built CD Microfluidics spin-stand (demonstrated in Section 6) [35]. Measurements were furthermore conducted using commercially available screen-printed carbon electrodes (DRP-110, Metrohm Dropsens, Asturias, Spain). 20µL of each HRP concentration level were incubated with 80µL of TMB substrate solution for 15 minutes in the dark before applying approximately 75µL of the resulting solution to the sensing surface of the electrodes. Amperometric measurements were then conducted by stepping the potential from 0 to -0.2V and measuring the current response over 60s. The current signal at 60s was plotted versus the solution concentration. Noise in on disc results was filtered using Fast Fourier Transformation (FFT) filtering (Origin 2018b, Originlab Corp., USA). Basics of amperometric detection are described in Section 5.

2.3.4. Calculation of LOD, Sensitivity, DR

The following equations, which are based on the guideline EP17 published by the Clinical and Laboratory Standards Institute (CLSI)[36], were used to calculate the LOD, limit of blank (LOB) and coefficient of variance (CV). Sensitivity was obtained as the slope of the calibration curve in the linear range and the DR as the range in which changing the concentrations yields a measurable change in signal (the linear dynamic range is the range in which the signal increases linearly with concentration). The DR covers the concentration window between lower and upper limit of quantification (LOQ), where in this work lower LOQ (LLOQ) and upper LOQ (ULOQ) are defined to afford a CV ≤ 20%.

$$LOD = LOB + 1.645\ (SD_{low\ concentration}) \tag{1}$$

$$LOB = mean(blank) + 1.645\ (SD_{blank}) \tag{2}$$

$$CV = \frac{SD}{Average} \tag{3}$$

With SD the standard deviation of measurements.

2.4. Results of HRP Detection – Absorbance, Chemiluminescence, Amperometry

Figure 1 shows the resulting calibration curves for chemiluminescence, amperometry and absorbance respectively. Table 1 shows a comparison of detection characteristics for the evaluated methods. While error bars were added in Figure 1 to show standard deviations, these are hardly visible in the scheme of the shown concentration range. Comparing the shape of the curves, it can be seen that chemiluminescence shows a rather constant sensitivity throughout the DR while amperometry shows two regions with different sensitivities. Sensitivities obtained are based on the respective measurement units: Absorbance Units (AU), Luminescence Units (LU) and micro Amperes (μA) and cannot be compared directly. They are presented in Table 1 as point of comparison for other researchers using the same technique.

Table 1: Performance characteristics of evaluated detection methods

Method	**LOD [mg/mL]**	**Sensitivity**	**LOB [mg/mL]**	**DR**	**Average CV in DR**	**LLOQ (for 20% CV)**
Absorbance	2.13E-7	4.21E5 mg/(mL*AU)	9.75E-8	1-2 orders of magnitude	4.8%	LOD
Chemi-luminescence	2.81E-8	1.17E7 mg/(mL*LU)	2.32E-8	About 4 orders of magnitude	5.0%	LOD
Amperometry	1.50E-6	2.49E4 mg/(mL*uA)	1.12E-6	Not reached in tests, at least 5 orders of magnitude	3.1%	LOD

When comparing the performance of the evaluated HRP detection methods it is evident that within the given set of commercial solutions, the chosen procedures and substrates, chemiluminescence allowed for lowest detection limit (chemiluminescence: 28.1pg/mL, absorbance: 213pg/mL, amperometry: 1.5ng/mL), while only requiring 5min incubation as opposed to 15min for amperometry and absorbance. This combination of properties is most desirable when a very sensitive POC diagnostic is needed with fast results within minutes. However, precise optical components and a very dark environment may be difficult to implement in a portable and low-cost device.

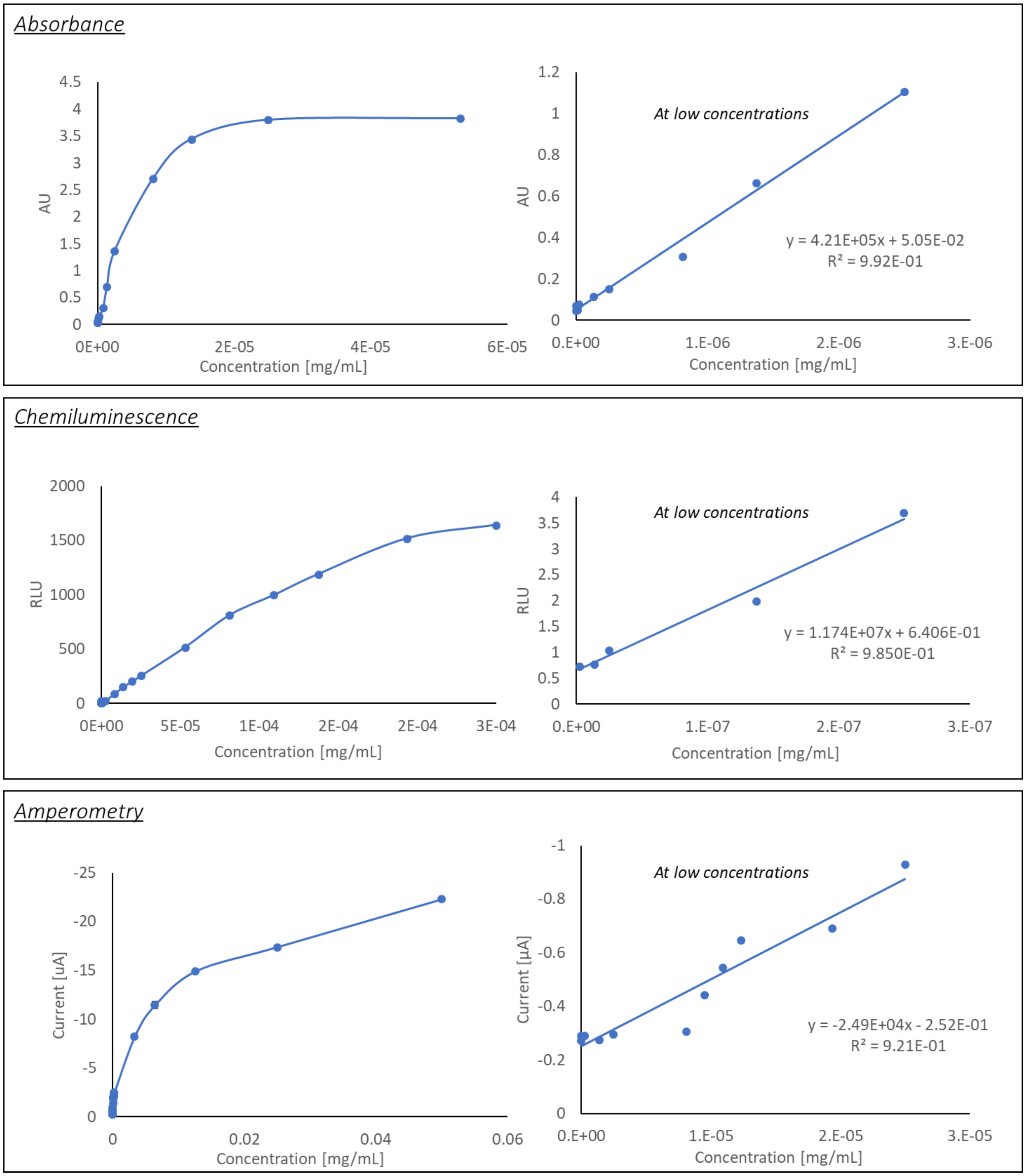

Absorbance

Chemiluminescence

Amperometry

Figure 1: Calibration Curves for absorbance, chemiluminescence and amperometric detection of HRP

While absorbance and chemiluminescence did not allow for quantification of HRP concentrations above 30ng/mL and 350ng/mL respectively, amperometry quantified even the highest tested concentration of 0.05mg/mL and therefore yielded the widest DR. This will especially be useful for applications where a large range of pathogen-concentrations is expected, as it allows for the diagnosis of samples from patients with a wide concentration distribution on a single detection device. Other methods with more limited DR may require prescreening and dilution in order to allow for detection of all patient samples, thus not only increasing complexity and cost of the POC diagnosis but also increasing turnaround time due to additional process steps. For all three methods, the CV was averaged throughout the respective DR and found to be well below 20% for all concentrations within the DR. Therefore, LLOQ with a requirement of less than 20% CV is at the LOD for all detection methods. The average obtained CVs for absorbance, chemiluminescence, and amperometry measurements were comparable at 4.8%, 5.0% and 3.1% respectively.

3. Prototyping of a Diagnostic Platform and Demonstration via Malaria Immunoassay

3.1. Background

3.1.1. Lab-on-Chip Platforms

Lab-on-chip (LOC) platforms containing fluidic networks of microchannels are often utilized for POC testing. These LOC platforms are highly portable, while integrating all necessary reagents to substitute a set of bulky and expensive laboratory equipment[37]. This miniaturization further leads to cost-reduction of tests by eliminating the need for laboratory settings and trained personnel, as well as by reduction in reagent consumption[38].

Haeberle and Zengerle [39] characterize microfluidic platforms (LOC devices) into capillary-driven systems (RDTs), “microfluidic large-scale integration” systems, electrokinetic platforms, centrifugal microfluidics, and “free scalable non-contact dispensing” devices. The main functions integrated on these platforms are: pumping and valving, mixing, separation, reagent storage and sample preparation[40]. A 2013 market review of LOC applications showed blood glucose analysis, electrolytes analysis, HIV diagnostics and determination of cardiac markers as some of the main applications of LOC systems by leading companies such as Abbott, Alere, Arkray, Bayer, LifeScan, Menarini Diagnostics, Roche and Siemens[40]. Diagnostic tests that run on microfluidic devices range from immunoassays (based on immune responses to an antigen of a particular pathogen) to molecular diagnostics (detecting and oftentimes amplifying deoxyribose nucleic acid (DNA) or ribose nucleic acid (RNA))[41]. While both diagnostics have been implemented on microfluidic devices, implementation of molecular diagnostics is generally more challenging due to more complex assay steps. For example, the use of polymerase chain reaction (PCR) for amplification of nucleic acids requires elaborate sample preparation and complex thermal cycling[41]. The following section will review some microfluidic devices for POC.

3.1.2. Lab-on-Chip Devices for POC based on Molecular Detection and Immunoassays

Liao et al.[42] implemented POC testing for herpes simplex virus (HSV-2) on a portable molecular diagnostic device. The so-called “smart cup” combines capillary fluidics and isothermal amplification to carry out a quantitative fluorescent loop-mediated isothermal amplification (LAMP) assay. The design uses the smartphone flashlight to excite the fluorescent dye and the smartphone camera for quantitative readout. Although the heating technique and the readout are very economic (Mg–Fe pouches are only $0.15), the design uses a custom-made microfluidic chip consisting of Qiagen silica membrane as entry port, and solvent-bonded, milled polymethyl methacrylate (PMMA) layers containing the microfluidic structures as described in Liu et al. [42,43].

In another publication by the same group[44], two custom-made, layered microfluidic chips were used for plasma separation and detection of nucleic acids via reverse-transcriptase LAMP. The plasma separation chip consisted of machined PMMA, plasma-separation membranes, and double-sided and single-sided adhesives. Another microfluidic chip was used for nucleic acid extraction and amplification[42–44]. The sample-to-answer testing would include loading the sample into the first chip, transfer of the plasma to the second chip as well as manual placing of the second chip onto a heating platform[44]. Besides a number of manual steps in running this assay, the fabrication sequence to produce these platforms is rather involved.

Microfluidic chips produced via injection molding can present a faster fabrication route and could also be a relatively affordable option for production of large numbers of fluidic chips. This fabrication option for enzyme-linked immunosorbent assay (ELISA) LOCs is discussed by Chin et al.[45]. Injection-molded LOCs were used to run hundreds of samples in Rwanda to detect HIV and syphilis simultaneously from 1μL of whole blood. While injection molding typically is used to produce features above 100μm in size, tight control of process parameters allowed for reduction of feature sizes to 1μm[45]. The materials used to form the microfluidic chips are polystyrene and cyclic olefin copolymer. Cost and time per chip of $0.10 and 40s, respectively[45], render chip fabrication via injection molding a low-cost and high-throughput manufacturing technique. While highly desirable if large quantities of identical parts are produced, injection molding is not an appropriate fabrication approach for research setting, prototyping, or production of a limited number of parts, due to high cost of molds.

3.1.3. 3D Printing for LOC Devices

Most LOC devices in research and product development are based on microfabrication methods using materials such as glass, plastic or polydimethylsiloxane (PDMS)[46]. While these fabrication methods require access to highly specialized and expensive microfabrication tools, as well as fabrication of a master for replica molding[47,48], recent developments in 3D printing, such as emergence of a wider range of materials and inexpensive printers, open new possibilities for rapid fabrication of affordable highly customizable LOC platforms[47,49–51].

For example, a POC device that implements LAMP for genomic detection of *Escherichia Coli* and *Staphylococcus Aureus* was fabricated with 3D-printing technology by Stedtfeld et al.[52]. The overall structure of the device was manufactured using stereolithography (3D printing based on curing liquid photosensitive resin by UV light[48]), while a channel network on the microfluidic chip was obtained using rubber-assisted hot embossing of polyester film with a 3D-printed mold. The polyester film was then assembled with a hydrophobic membrane and closed off with patterned adhesive[52]. The developed device is operated through an iPod Touch, which is also utilized for data analysis and Wi-Fi connectivity. A sample is loaded manually using a pipettor, while hydrophobic membranes and manual taping of vents after fill maintain fluid in the channels and prevent contamination[52].

Material jetting is another 3D-printing technology, and was used by Erkal et al.[53] to create a microfluidic device which holds electrodes for electrochemical detection of dopamine and nitric oxide. Another 3D-printed fluidic device demonstrated by the same group was used to measure the presence of adenosine triphosphate (ATP) while observing oxygen stimulus concentration in the sample[53]. Both devices were fabricated on an Objet Connex 350 multi-material printer.

Stereolithography and material jetting are well suited for designs requiring leakage-free bonding between adjacent layers, but these technologies are significantly more expensive than alternative 3D technologies such as fused deposition modeling (FDM)[47]. Prices for low-end FDM printers recently dropped from $14,000 to $300 due to expiration of patents, and are expected to decrease further as a large community of hobbyists has evolved around 3D printing, making hardware open source and sharing designs and ideas online[54].

The principle of FDM is based on layered deposition of liquefied material and is illustrated in Figure 2. Thermoplastic filaments are stored on spools and extruded through heated nozzles, where the plastic is liquified upon reaching the glass transition temperature. The molten material is then deposited onto the base, where it cools down and solidifies. To deposit a new layer atop of solidified material, the build platform holding the base is lowered. The height of one layer is defined by the lowering distance of the build platform between successive layers, and is as low as 100µm[55–57].

To save material and time, parts are typically not printed solid but filled with a hexagonal honeycomb structure (this so-called infill differs in the various systems and can be of different geometric pattern). The surface of printed parts consists of the denser shell of material. These shells consist of typically one to four layers (the number can be chosen by the user) of extruded material and give the part its shape while sealing the hollow infill.

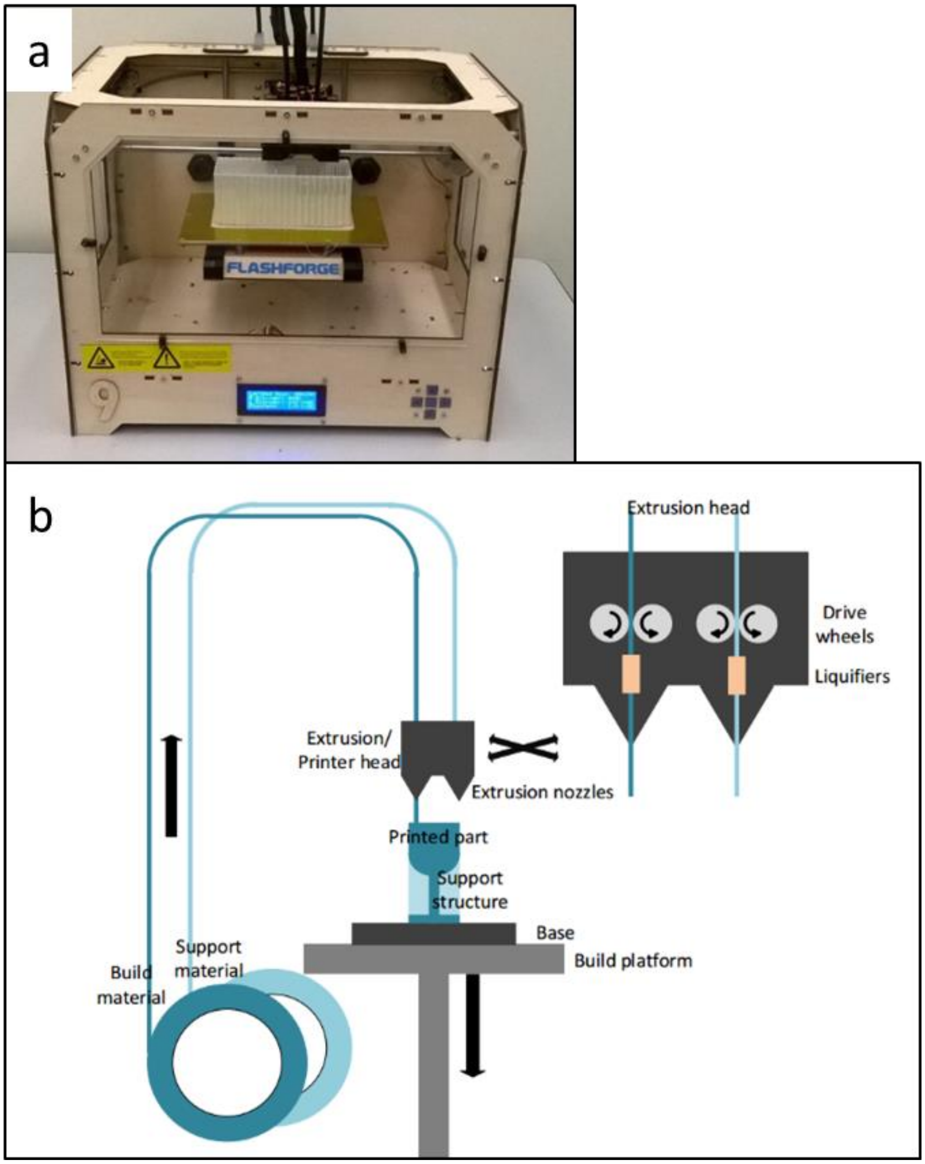

Figure 2: a) Flashforge Original Creator, the fused deposition modeling (FDM) system used for building devices in this work. b) Principle of material extrusion: Thermoplastic filament is heated while extruded through a nozzle onto the build plate. It re-solidifies as it cools down, and after the build plate is lowered, the next layer is deposited, thus forming the desired geometry.

Waheed et al.[49] recently analyzed advantages and disadvantages of different FDM systems utilized for the fabrication of microfluidic devices, and found that these systems are simple to use and able to fabricate affordable microfluidic systems. However, FDM-printed parts present a staircase effect deriving from the layered fabrication method. The extent of this effect is impacted by the layer height, negatively affects the surface texture, and limits the resolution of printed parts. The average deviation for features printed in the X and Y directions was reported to be 60.8 and 71.5µm, respectively[49].

Among the nine FDM systems analyzed in Waheed et al.[49] was also the MakerBot Replicator 2X (MakerBot Industries, LLC, New York, NY, USA), which was demonstrated by Kadimisetty et al.[58] to be capable of manufacturing a low-cost ELISA platform for the electro-chemiluminescent detection of cancer proteins. The channel height of this fluidic chip was 200µm, which corresponds to the layer height of the MakerBot Replicator 2X[58]. To actuate liquids, Kadimisetty et al.[58] rely on gravity by manually tilting the device.

Another device that uses 3D printing for device manufacturing, as well as a smartphone for readout, is described by Berg et al.[59]. The smartphone is not only used to read out the colorimetric ELISA (supported by a lens in the printed device) from a 96-well plate, but also allows for a custom mobile application with an interactive user interface. To allow for improved data processing, a server was used in conjunction with the fluidic device and a smartphone. Generally, smartphones are increasingly used in POC devices[42,52,59,60] to replace bulky and expensive optical instruments while benefitting from portable dimensions, built-in light source, and integration of multiple functions such as imaging, image processing, and providing a user interface via touchscreen, as well as Bluetooth and Wi-Fi connectivity.

Wireless connectivity is especially important for POC applications as it enables remote analysis of data and real-time feedback from specialists in central hospitals to patients in remote areas[52].

While all microfluidic devices use some type of external force propelling liquid through channels, Iwai et al. implemented a human-powered pumping system, allowing for resource-free (no electricity or external components) actuation of fluids through channels. In this design, a human finger pushes down onto an air-filled pressure chamber exerting increased pressure onto fluids in connected microfluidic channels. As the finger releases the dome on the pressure chamber, membrane-type fluidic diodes close, preventing backflow. Cantilever-based diodes are integrated to allow for multiple refills of the channels from fluid inlets. An injection-molding process was developed for low-cost mass production, however, it required increasing channel dimensions from 100 to 300µm, and introducing the need for oxygen plasma and thermal treatment for the bonding of layers[61]. While the finger-powered microfluidic device does not need external power sources, it is difficult to automate when a sequence of fluidic steps is required.

To allow for simple prototyping of POC diagnostics, a low-cost 3D printing approach was developed and demonstrated to fully automate process steps for a malaria assay.

3.2. Materials and Methods

3.2.1. Components and Operation Principle

The produced automated bioassay platform consists of the 3D-printed fluidic cartridge and a reusable frame holding the electronic components. In the course of this study, three generations of prototypes were fabricated. All 3D-printed parts were designed using

SolidWorks (Versions 2014/2015 through 2016/2017, Dassault Systems Corp., Vélizy-Villacoublay, France), exported as STL files and converted into g-code using MakerWare 3.4 (MakerBot Industries, New York, NY, USA). All parts were printed using a Flashforge Original Creator (FlashForge Corp., Jinhua, China) with 1.75mm ABS filament (MatterHackers, Inc., Lake Forest, CA, USA).

To create flexible domes, 3D-printed molds (printed on Flashforge Original Creator with 1.75mm ABS filament) were filled with Mold Star 30 elastomer (Smooth-On, Inc.). The print settings that were utilized in the printing of dome molds, electronics case and actuation gears are standard print settings: travelling speed: 90 mm/s, extrusion speed: 60 mm/s, heating platform temperature: 115 °C, extrusion temperature: 240 °C,, number of shells: 2, layer thickness: 0.2 mm. The molds consisted of bottom and top halves with a 2mm wide gap for the elastomer to form the dome. The molded domes were allowed to cure overnight.

Reagents were injected into storage chambers with a syringe needle piercing through the elastomeric domes before the use of the device. Utilization of a gauge-21 needle allowed the elastic domes to self-seal after injection of the reagents.

First Prototype:

The first, smallest prototype (with a footprint of 75 × 50mm), shown in Figure 3, contained four reagent-storage chambers and enclosed channels leading to an open detection/reaction well. Silicone domes were sealed to the cartridge with Sil-Poxy Silicone Adhesive (Smooth-On, Inc., Macungie, PA, USA). The servomotors (TowerPro SG90 Micro Servos, Shenzhen Hao Qi Core Technology Co., Ltd., Guangdong, China and HS-5645MG Digital High Torque Servo Motor, HITEC RCD USA Inc., Poway, USA) were controlled by a smartphone or laptop (via

Arduino board) and plastic arms attached to servomotors pushed on silicone domes to expel the reagents from the storage chambers into the detection/reaction well (micro-servomotors are available for less than \$5[62]).

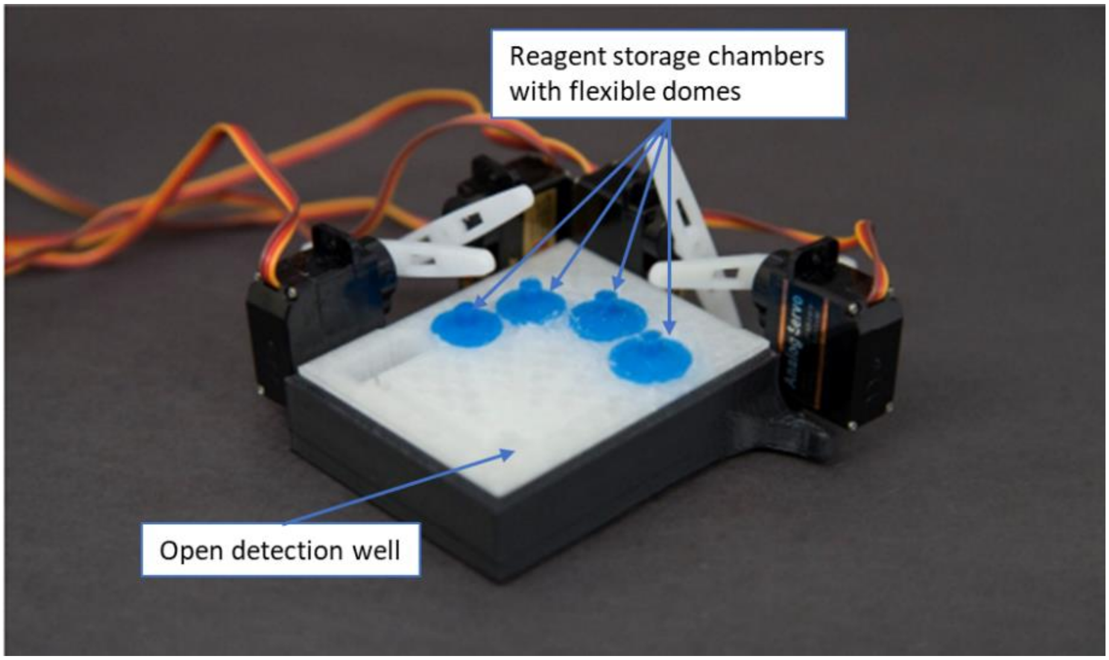

Figure 3: First design moving fluid through enclosed channels by servomotor actuation controlled from a smartphone audio jack (footprint 75 × 50mm).

In order to demonstrate the developed device with a bioassay with manufacturer recommended volumes, the cartridge had to be scaled up (e.g. total of 3.6mL washing buffer; for comparison, the storage reservoirs of the first prototype held about 70µL of washing buffer).

<u>Second Prototype:</u>

Figure 4 shows the second prototype with a footprint of 124mm × 104mm.

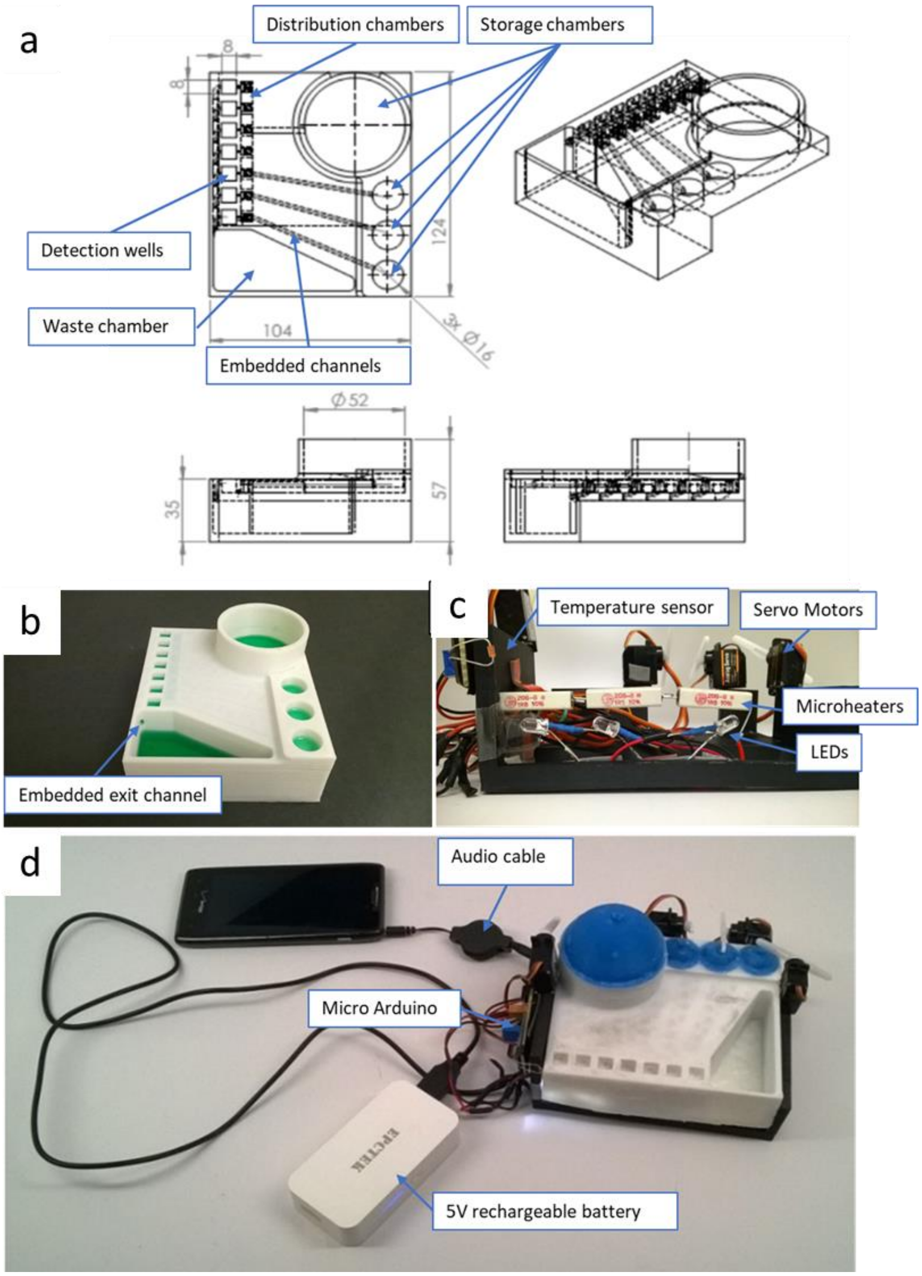

Figure 4: Second design powered by portable battery and controlled via smartphone. The design implements fluid actuation, lighting, incubation (heating and temperature control). a) Major dimensions of prototype in mm. b) Printed cartridge with colored water. c) Reusable frame holding electronics. d) Fully assembled device with electronics connected to portable battery and audio outlet of smartphone.

Besides increased reagent volumes, this platform integrated microheaters and a temperature sensor for incubation, as well as LEDs underneath the detection wells for improved illumination for higher fidelity during readout. Fluid propulsion followed the same principle of servomotors pushing flexible silicone domes atop of reagent-storage chambers. The second prototype included seven detection/reaction wells that had integrated antigen-coated test wells obtained from the break-apart well plate contained in ELISA bioassay kit (IBL International GmbH, Hamburg, Germany). All channels from the storage chambers lead to the distribution chambers (a series of interconnected shallow reservoirs), which were designed to allow for equal allocation of the reagents to all detection wells (see Figure 4a). Exiting the detection wells, fluid flows through the embedded exit channel into the waste chamber (see Figure 4b).

Some of the deficiencies of this second prototype included internal leakage, occurrence of cross-contamination between neighboring detection wells, and limited controllability of pumped volumes.

Third Prototype:

To address issues of the second prototype, the following changes were implemented in a third prototype, shown in Figure 5 (with footprint similar to second prototype):

- the microfluidic network of channels was redesigned to allow for improved gravity aided fluid actuation, thus avoiding cross-contamination risk,
- Plasti Dip coating (brushed on and cured overnight; Plasti Dip Int., Minneapolis, MN, USA) was used for exposed channels and chambers to eliminate leakages,
- replacement of rotary by linear movement to push on domes through 3D printed gears (see Figure 5b).

For qualitative readout and to evaluate successful solving of the issues observed in the second prototype, incubation at room temperature was found sufficient to allow a clearly distinguishable result of positive and negative controls even without the use of LED lights.

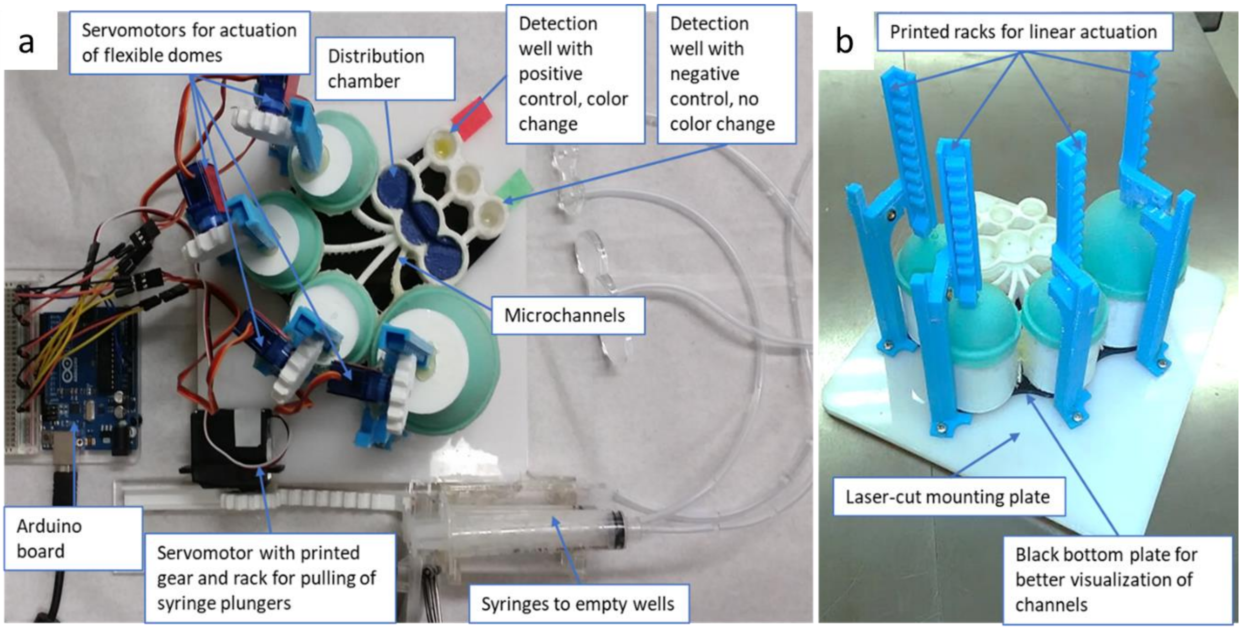

Figure 5: a) Top view of the third prototype incorporating a 3D-printed set of racks, gears and waste syringes (two waste syringes are stacked one atop the other). b) Side view of the third prototype (gears, motors and syringes are removed to facilitate the clear view of the fluidic platform).

For ease of fabrication of the third prototype, a bottom plate (serving as the frame for servomotors), as well as lids for the wells (to hold tubes in place), were laser-cut from cast acrylic sheets (McMaster-Carr Supply Co., Elmhurst, IL, USA) using an 80W Speedy 360 Trotec Engraver (Trotec Laser GmbH, Lyss, Switzerland).

3.2.2. Control and Electronics

While the prototypes varied in their electronics components, the main elements are as follows:

Control and Automation:

Electronics were controlled via an Arduino Uno (OSOYOO Mini USB Nano V3.0 ATMEGA328P, Pintree Electronics Ltd., Richmond, Canada) connected to a smartphone (Lumia 521, Nokia, Espoo, Finland) or laptop (Toshiba Satellite Pro, Toshiba, Tokyo, Japan) and powered either from the laptop or by a rechargeable 5V battery (EPCTEK® 5200 mAh Power Bank Portable Charger, EPCTEK Technology Co. Limited, Hong Kong, China).

Automation of the bioassay platform was furthermore implemented via a music file (.wav) that contained sounds of different frequencies and duration (an example is given in Bauer et al.[63]). Arduino microcontrollers were programmed using Visual Studio in C++ (see the program in Supplementary Material[63]) to translate music input into specific electrical signals to control electronic components such as servomotors, LEDs etc. Various frequency ranges controlled different devices. For example, a frequency between 1100 and 1400Hz actuated servomotor 1, while a frequency between 4100 and 4400Hz changed the position of servomotor 4, allowing for the control of multiple components by a single music file. Advantage of this approach is that the platform is adaptable to different procedures (e.g., for different bioassays), because the Arduino serves as a translator rather than holding a single program for the platform. Additionally, storage and distribution of the programs is as easy as storing or sending a song, and devices to control the platform range from MP3/CD players to smartphones to laptops. Different websites allow to generate the sequence of sinusoidal signals utilized for activation of the different functions (e.g., www.wavetones.com and www.onlinetonegenerator.com). These can then be downloaded as .wav files.

Fluid actuation:

- Four TowerPro SG90 Micro Servos servomotors (with 90° rotation range) were used to push the silicone domes on top of the reagent-storage chambers.
- Two 10mL syringes (see Figure 5a)) with racks and gears connected to plungers and a servomotor (HS-5645MG Digital High Torque Servo Motor with continuous rotation) allowed to provide the necessary suction to empty out reagents from the detection well through tubes after each washing step.

Heating:

Three wire resistors (5W, 1Ω, each 25mm) for incubation at 37°C, positioned under the detection wells, and a temperature sensor in close proximity to the detection wells for temperature control (no active cooling was implemented).

Readout:

Besides visual evaluation of the color change, readout via smartphone camera and processing with the Color Catcher phone app was demonstrated. The Color Catcher application exported the color in the image as RGB values. Such data can be read out directly from the phone or sent out for analysis via the phone network, Bluetooth or Wi-Fi (for example to a hospital laboratory). To support reproducible readout with a smartphone camera, LEDs were positioned under the detection wells and the color was imaged without any other light sources to ensure consistent lighting (see Figure 6).

Figure 6: LED backlighting for readout; empty cartridge.

3.2.3. ELISA Steps and Implementation

The malaria bioassay implemented in this study is based on antigen–antibody reactions occurring in the test tubes inside the detection wells. The steps are illustrated in Figure 7 and include the attachment of primary antibody (present in infected blood due to an immune reaction to malaria pathogen) to antigen immobilized on the bottom of the test wells, attachment of a secondary antibody (contained in malaria conjugate) to the primary antibody, color change enabled by the enzymes (HRP) attached to the secondary antibody after addition of TMB substrate, and stopping the color-change reaction with addition of the stop solution. To avoid false results due to unbound antibodies, multiple washing steps are performed.

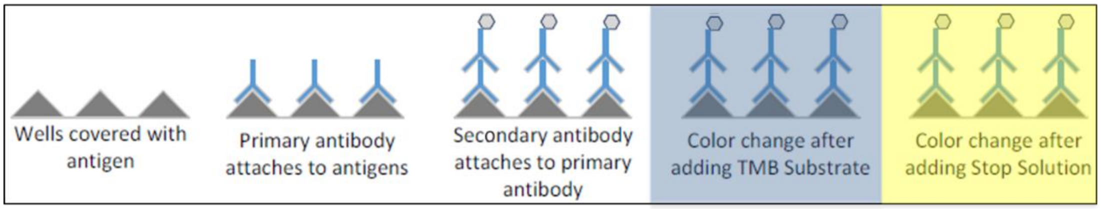

Figure 7: Schematic malaria ELISA steps. Test wells contained in the malaria kit are precoated with specific antigens. Primary antibodies (present in infected blood due to a patient's immune reaction to malaria pathogens) bind to antigens. Secondary antibodies (contained in malaria conjugate) are employed for optical detection as they are conjugated to the enzyme, effecting the color change of the solution after TMB substrate is added. The presence or absence of the color change of the solution in the detection wells is evaluated after the stop solution is added.

Prior to the start of the automated bioassay protocol, precoated wells are broken from the 96-break-apart strips (part of the assay kit) and inserted into the cavities of the printed platform. Subsequently, the positive and negative controls, supplied as part of the kit and representing patients' samples, are pipetted into these wells. After incubation of the controls in the wells (see Table 2 for details of each step), the automated protocol is started. Automation includes pre-determined sequence of servomotors pushing on flexible domes atop four reagent-storage chambers containing the four reagents (bottom to top in Figure 5a): washing solution, malaria conjugate, TMB substrate and stop solution. When the arm of a servomotor presses on the dome, a liquid reagent is expelled from the reagent storage below the dome to go into the distribution chamber. About 0.20mL of a reagent is left in the reagent chamber after it is fully compressed.

Reagents are sequentially propelled through the channels into the distribution chamber and flow from there into the detection wells. To empty the wells after washing steps, the continuous servomotor mounted on the side of the reusable case (see the bottom of the Figure 5a) pulls the plunger out of the syringes and hence empties the wells through the tubes attached to the syringes. After application of the stop solution (also loaded into one of the domed chambers), the color of the positive control solution changes from blue to yellow. Table 2 summarizes the steps performed on the 3D-printed automated platform (recommended steps including readout on ELISA reader are listed in Bauer et al. [63] Appendix Table A4).

Table 2: ELISA steps implemented on the 3D-printed automated bioassay platform.

Step	**Activity**
1	Manual dispensing of 100µL controls (2 positive, 2 negative, 2 cut-offs, 1 blank) into the wells
2	Incubation for 1h at 37°C
3	Washing the wells with approx. 5 × 300µL, 5s soak-time each and overflow to the waste/emptying of the wells after each washing step via automated syringe
4	Dispensing of approx. 300uL malaria conjugate into the wells
5	Incubating the wells at room temperature for 30min
6	Washing the wells with approx. 5 × 300µL, 5s soak-time each and overflow to the waste (prototype 2)/emptying of the wells after each washing step via automated syringe (prototype 3)
7	Dispensing of approx. 100µL TMB substrate solution in all wells

8	Incubating for exactly 15min at room temperature, in the dark
9	Dispensing of approx. 100µL stop solution in all wells
10	Readout of the qualitative result by eye, usage of the smartphone application Color Catcher to record the RGB color codes

3.3. Results & Discussion

3.3.1. Optimization of FDM Print Settings

Due to imperfect fusing of the adjacent layers, microfluidic devices printed via fused deposition modeling can frequently be subject to leakage[64]. Figure 8 shows a printed part (second prototype), where stained sections indicate the presence of leakage after dyed water was passed through the device.

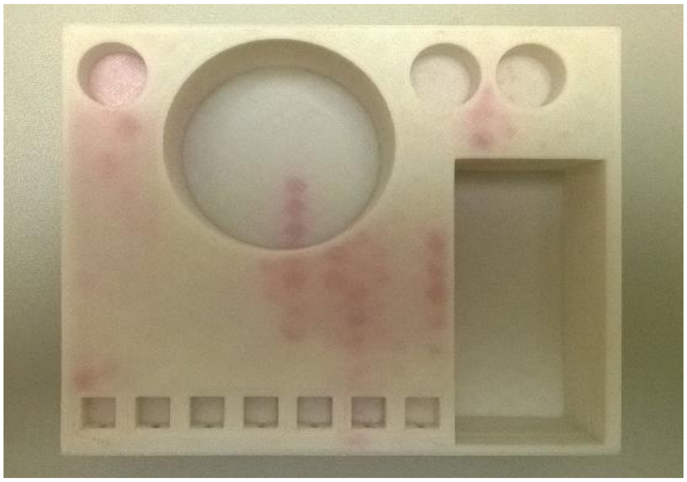

Figure 8: Printed part with leakages showing red. Dyed water marks the hexagonal infill structures filled with water through leakages from chambers and enclosed channels into the part.

To fabricate leakage-free fluidic cartridges, different print settings were tested and analyzed for their contribution to maintaining the designed device and channel geometry while avoiding leakages. Table 3 summarizes the influence of various print settings on the quality of the test piece. While it is known that a high infill can be beneficial in order to decrease leakage [64], this option was not considered, as it leads to significant increase in print time and fabrication cost. For testing of the effect of different print settings on leakage and geometric accuracy, the following parameters were kept constant throughout all tests: heating platform temperature: 115°C, number of shells (walls surrounding the infill): 4, and travelling speed: 90mm/s. Varied settings were: layer height (0.1mm to 0.2mm), extrusion speed (60mm/s and 80mm/s) as well as extrusion temperature (230°C, 240°C, 243°C (any higher temperature led to bubbles in extruded material through overheating)). The optimal print setting was found to be a combination of 240°C extrusion temperature, an extrusion speed of 60mm/s, and a layer height of 0.16mm.

Table 3: Optimization of print settings for the Flashforge Original Creator using 1.75mm acrylonitrile butadiene styrene (ABS) filament. Geometry is qualitatively categorized into three types: large deformations (--), small deformations (-), negligible deformations (+).

Test	**1**	**2**	**3**	**4**	**5**	**6**	**7**	**8**	**9**	**10**
Extrusion temperature (°C)	240	240	240	240	240	243	240	240	230	240
Extrusion speed (mm/s)	60	60	60	80	80	60	60	80	60	60
Layer height (mm)	0.12	0.14	0.16	0.1	0.2	0.1	0.1	0.1	0.2	0.18
Leakage	No	No	No	No	Yes	No	No	No	Yes	Yes
Geometry	--	-	+	-	+	--	--	--	--	+

Figure 9 top demonstrates the examples of test cubes with and without leakage after submerging in dyed water. To minimize distortion of embedded fluidic channels as well as to avoid the need to have supporting pillars inside channels, an elliptical cross-section able to support the channel roof was selected. The rhombus (diamond shape) is another channel geometry that is self-supporting[64]. The geometry of the test cubes is provided in Figure 9 bottom.

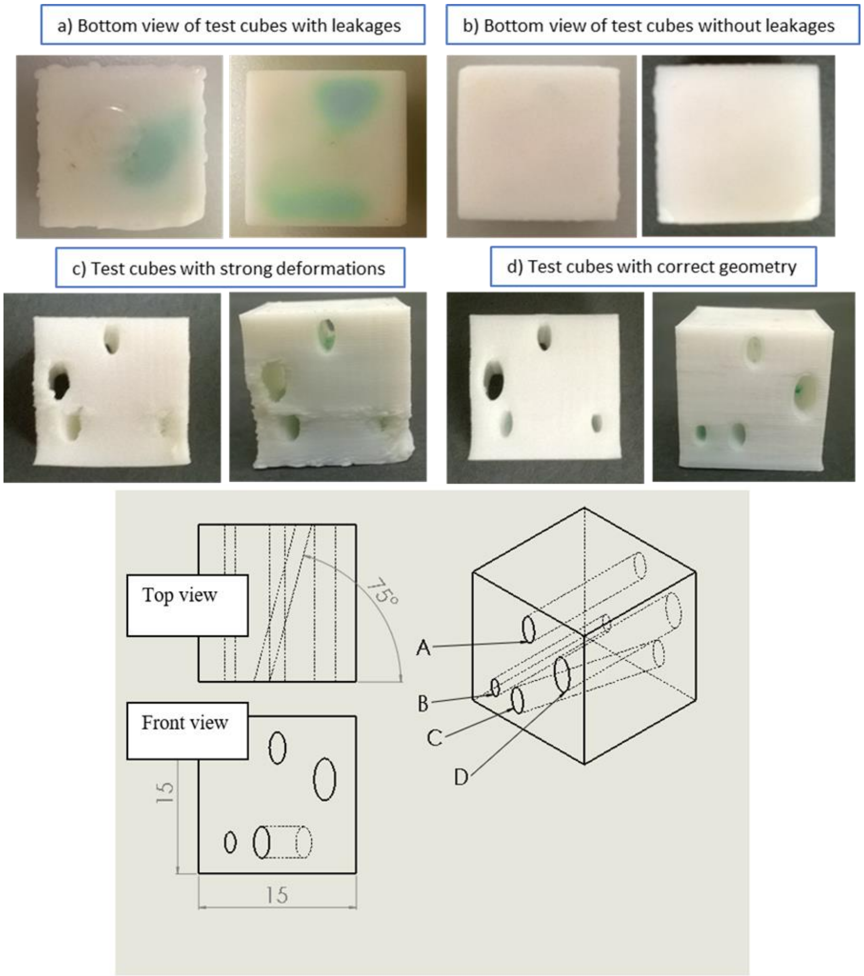

Figure 9: Top: Test cubes with leakage after submerging in dyed water. Bottom: Major dimensions of test cubes in mm. Channel C is inclined 75° with respect to the side of the cube. Channels have elliptical cross sections (major axis (mm) × minor axis (mm)): A, C: 3 × 1.5, B: 2 × 1, D: 4 × 2.

3.3.2. Postprocessing for Leakage Reduction

Additionally to improving of print settings, different post-treatments were tested and evaluated to further minimize leakages. Effectiveness for leakage reduction of the following treatments was tested: exposing the structure to solvent (acetone), coating the structure with a rubber coating (Performix Plasti Dip Multi-Purpose Rubber Coating, Plasti Dip Int.), and dipping the device into heated paraffin wax. Acetone treatment involved dipping the fluidic cartridge into acetone and soaking it for several seconds. Acetone dissolves the ABS, and the dissolved material resolidifies as the acetone evaporates. This process typically allows the dissolved material to fill small trenches between fibers, sealing the gaps. However, the process did not produce consistent results and alternative treatments were selected.

Wax was found to be an effective technique to reduce leakage of 3D-printed fluidic parts. In this method, the fluidic device is dipped into the bath with wax (Paraffin Wax, Laboratory Grade, Carolina Biological Supply Co., Burlington, NC, USA), heated to 80°C for a few seconds, and before the wax did solidifies, compressed air is blown through the fluidic channels to empty out excess wax.

To evaluate the effects of different surface treatments, the following 3D-printed parts were characterized: as-printed ABS surface, printed surface coated with Plasti Dip, printed surface coated with wax, and printed surfaces after acetone exposure. A confocal 3D laser scanning microscope (VK-250, Keyence Corp., Osaka, Japan) was used to characterize the surface roughness, and contact angle measurements (MCA-3, Kyowa Interface Ltd., Tokyo, Japan). Results are shown in Table 4. Average surface roughness (Ra) is 64.67μm for the untreated surface, Plasti Dip coating, wax coating, and acetone exposure for 10 or 60s decreased this roughness to 29.76μm, 21.85μm, 9.85μm or 5.86μm, respectively.

For each surface, four measurements of the stationary contact angle in different areas of the respective sample were taken. Overall, the wax coating showed the highest hydrophobicity with a contact angle of 102.27° compared to a contact angle of 80.24° for the untreated printed ABS surface. The standard deviation is the highest in the case of the untreated surface, which is likely due to the uneven topography of the part (different results in measurements in a trench versus elevated areas as well as depending on orientation of part). Acetone treatment and wax coating showed the lowest variation in contact angles when compared to untreated and Plasti Dip-coated parts. The volumes of the droplets used for contact angle measurements were in the range of 15.33μL to 20.56μL and are expected to not have significant impact on the measurements. Although the average contact angle after 10s acetone treatment compared to the untreated part (81.78° versus 80.24°) is slightly higher, 60s soak in acetone decreases the contact angle drastically to 67.15°. Therefore, the initial increase can be assumed to be within the deviation (especially because for the untreated part, the standard deviation is 15.76°).

Table 4: Contact angle measurements of different surface treatments of FDM-printed ABS parts.

Parameter	**Untreated ABS**	**Acetone 10s**	**Acetone 60s**	**Coat of Wax**	**Coat of Plasti Dip**
Mean contact angle [°]	80.24	81.78	67.15	102.27	72.32
Standard deviation [°]	15.76	2.546	4.246	3.33	10.02
Average droplet volume [µL]	17.41	22.54	15.33	20.56	17.64
Average surface roughness [µm]	64.67	9.85	5.86	21.85	29.76

3.3.3. Colorimetric Malaria-ELISA Test Results

Feasibility of a qualitative readout of the automated bioassay was demonstrated by obtaining a color readout for positive and negative controls. Figure 10 shows the automated device after application of the stop solution. The well with positive control is shown on the right and indicates a color change (yellow) while the negative control (left) shows no change in color. The tests were repeated several times by replacing the test wells, rinsing the microfluidic structure with water and soap, and switching the locations of positive and negative wells to verify repeatability of the experiment.

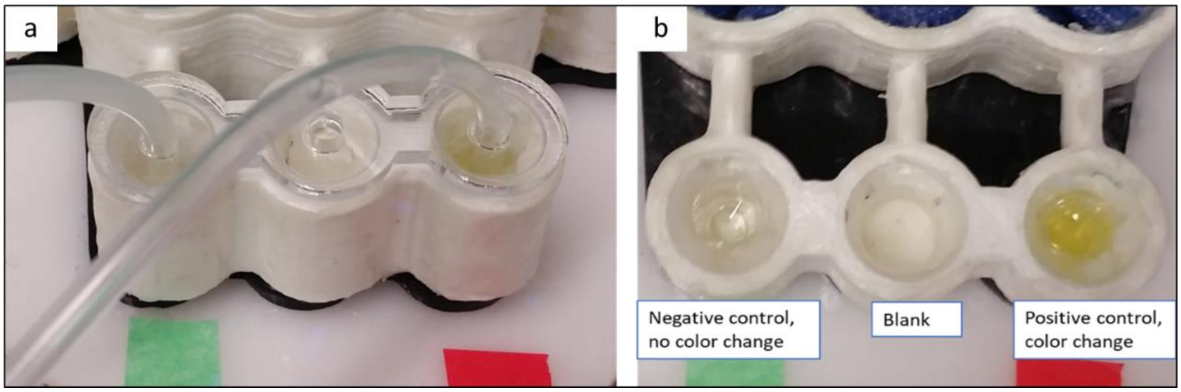

Figure 10: 3D-printed device with colorimetric malaria ELISA. a) Laser-cut lid to hold tubes for emptying of wells. b) Colorimetric results after application of stop solution. Left: negative control well, middle: blank well, right: positive control well.

3.4. Conclusions

In this section we introduced an approach for rapid prototyping of 3D-printed microfluidic platforms allowing for automation of immunoassays and enabling portable diagnostics specifically for research settings or a small number of parts. Advantage of printing the diagnostic cartridge on a low-cost material extrusion system (working principle see Figure 2) is the fast turnaround time for different designs to implement different assay steps and reagent combinations while only utilizing a single tool. Major challenge in utilizing material extrusion for building of microfluidic devices showed to be leakage control. While a smooth surface topography was achieved through treatment with acetone, this did not solve inherent leakage between adjacent layers. Print settings were optimized to improve bonding between layers, but ultimately an outside coating on exposed channels helped to seal the print. Printed ABS surfaces with and without acetone treatment and with different coatings were analyzed for their hydrophilicity and surface roughness to evaluate fluidic material characteristics.

While the fluidic cartridges are generally disposable, the hardware that holds electronics and servomotors is reused and can control a variety of bioassays (e.g. differing in number and volume of reagents or in sequence of servomotor actuation and timing). To the best of our knowledge, this is the first diagnostic device, controlled via an audio port/audio file, presenting an alternative to loading a new program onto a controller board. To change fluid actuation sequence or timing simply a new "song" can be played. This approach enables ease of storage and distribution of an assay program. The demonstrated system furthermore integrates the ability to aspirate fluid from wells and thus allows for automation of complex multi-step bioassays including repeated usage of fluid stored in the same reservoir, washing, dilution, and flow reciprocation. While the developed devices were tested for colorimetric detection via smartphone or visual evaluation, electrochemical detection could easily be integrated by placing electrodes in a chamber preceding the detection well. This could furthermore allow to reduce reagent volumes, which, for optical detection, need to be sufficiently large to detect the color change in the detection well.

In this work, liquid reagents were loaded into the printed devices prior to usage. Alternatively, reagent-storage options, such as dry storage as well as storage in glass capsules and pouches, can also be utilized for on-board reagent storage[65,66]. The arm movement of the servomotor during the initial actuation could break these pouches or capsules and allow for the reagents to be released. It is possible to pause fabrication to place vials or packages with the reagents into the storage chambers during the printing process.

Instead of being molded and sealed to the device, the flexible domes, could be printed in the same printing process as the microfluidic insert, since some FDM printers allow for multi-material printing, including the use of flexible polylactic acid (PLA)[67] and thermoplastic polyurethane (TPU)[68].

4. CD Microfluidics

Another platform used in the research environment but also in commercial applications is the microfluidic CD. This approach is increasingly used in the microfluidic community due to its elegant, simple and effective pumping principle[69]. Based on centrifugal pumping pressure supplied by a single spinning motor, liquid motion is often only controlled by channel geometry and diameter, or other non-contact valving methods, thus eliminating contamination-prone interfaces to the outside world, while allowing for a bubble-free flow (bubbles move to the center of the disc based on lower density), and integrating a complete diagnostic sample-to-answer system. Depending on spin speed of the motor, diameter, and orientation of a channel, a wide range of flow rates (5nL/s to 0.1mL/s) is feasible[69] and a variety of bioassay steps including but not limited to metering[70], passive[71] and active[72] valving, blood plasma separation[73], lysis[74], mixing[75], amplification[76,77] and detection[35,77] have been integrated on the CD. Some microfluidic companies who base their diagnostic systems on CD technology are Abaxis, Nexus Dx, GenePOC, and Spinit.

4.1. Burst Valves

4.1.1. Introduction to Burst Valves on the CD

Madou et al. (2006) point out the importance of ease of valving implementation when choosing a fluidic system. While traditional pumps most elegantly solve valving for both, liquid and vapor by utilizing two one-way valves, their scaling is not favorable for portable systems[78]. Generally, avoidance of external bulky instrumentation for liquid actuation and valving systems is essential for truly portable and disposable fluidic systems[79,80].

Furthermore, as most disposable microfluidic systems are based on injection molding of thermoplastics, valving needs to be compatible with this manufacturing choice[79].

Valves can generally be classified into active and passive valves, with active valves requiring an external activation stimulus while passive valves solely rely on the interplay between surface tension, chemical composition and topography of a surface. Active valves therefore usually allow for higher control but drastically increase complexity of the instrumentation needed[81]. One simple and instrumentation-free approach for valving is the integration of cross-sectional changes into microfluidic channels, causing fluid to stop at a specific point due to an increase in capillary pressure. When the fluid is stopped at such a point, an increase of the external pumping pressure above the critical capillary pressure causes the fluid front to burst forward as the capillary barrier is overcome[82]. This type of valve is therefore called a burst valve.

To implement burst valves into a new microfluidic platform or change a design, generally a series of prototypes is manufactured and tested to determine the burst pressure as a function of the detailed device geometry. These findings are then translated into an injection molded design and a costly mold is made. Because prototypes and products often differ in manufacturing technique and material, the balance of capillary forces and pumping pressure can be altered, potentially leading to differences in the performance of burst valves. As many bioassays require the sequential release of multiple reagents, a series of multiple burst valves at different break pressures is desired, thus adding complexity to the design. Precise prediction of changes in burst frequency when moving from prototyping to manufacturing and when changing material, can prevent valve failure and expensive iterations. The aim of this work is to add to the existing models predicting burst pressure for different burst valve geometries[82–88] and specifically to evaluate how the burst pressure depends on the manufacturing technique and the material of the microfluidic structure. Furthermore, general limitations of burst valves are discussed and suggestions for proper integration to achieve robust microfluidic designs are made. While CD microfluidic platforms are used to generate burst pressure in experiments in this work, results are applicable to various other pumping mechanisms.

4.1.2. Burst Model

In general, a valving point occurs in a microfluidic circuit at any location where there is a sudden increase in capillary pressure resisting forward fluid flow. In our geometry, a series of deeper chambers and shallower and narrower channels, there are two possible valving points per burst channel: the inlet and the outlet of the channel, thus leading to two possible burst behaviors of a valve. The first is based on liquid stopping at the channel inlet and then bursting through the channel into the subsequent chamber once the capillary pressure at the channel inlet is overcome. The second burst behavior is described by liquid stopping at the channel outlet and bursting forward once centrifugal pressure overcomes capillary holding forces at the channel outlet. In the latter case, liquid may or may not stop at the channel inlet prior to halting at the channel outlet. Because liquid must pass both locations (channel inlet and outlet) in order to reach the next chamber, the maximum burst frequency of both cases determines the burst behavior. However, taking surface imperfections into consideration there is yet a third scenario, which is described by fluid creeping into a channel along local favorable surface imperfections. Liquid may then stop at any point within the channel until the centrifugal pressure is high enough to move the liquid through the channel, or it may advance with increasing velocity as the head height of the fluid (radial distance between advancing and receding fluid front) increases, thus contributing to higher centrifugal pressure as can be seen from Equation 4. Liquid momentum may contribute to overcoming capillary pressures at the channel outlet, is however not considered in the proposed calculation.

Driving pressure can be obtained from:

$$\Delta P_d = \frac{1}{2}\rho\omega^2(r_A^2 - r_R^2) \tag{4}$$

Where ΔP_d is the driving (centrifugal) pressure on a fluid plug in a channel, r_A is the distance from rotation center to advancing fluid front, and r_R is the distance from rotation center to receding fluid front ($r_A > r_R$).

Various analytical models for the prediction of burst valve pressure have been described previously[82–89], all of which are based on the Young-Laplace equation and the change of total interfacial energies. Our model is a generalization of the calculation by Cho et al. (2007), in which we have accounted for the change in channel height as well as for a different contact angle for the material of the cover. The model is based on the pressure difference of advancing and receding fluid fronts, and derives the burst frequency, ω_b, from the equilibrium of capillary and centrifugal pressure. Equation 5 and Equation 6 show the proposed calculation for a burst event depending on liquid entering and exiting the channel respectively. It is assumed that fluid arrives parallel to the plane of cross-section change at the channel inlet, which leads to no change in the angle of the capillary force. Therefore, the cross-section change between channel and chamber is only considered in the advancing contact angle when the burst event depends on overcoming capillary pressure at channel outlet. While Equation 5 and Equation 6 describe the theoretical burst cases of a part with homogeneous hydrophobicity, Equation 7 describes the scenario where liquid advances into the channel along surface imperfections. As liquid in this scenario may stop at any point within the channel the fluid front is assumed in the middle of the channel as an approximation of the average position of advancing liquid front.

Burst frequency equations:

Burst frequency is based on capillary pressure overcoming centrifugal pressure. While centrifugal pressure can be obtained from Equation 4, burst frequency is obtained from $\Delta \mathrm{P_d} = \Delta \mathrm{P_{capillary}}$, with $\Delta \mathrm{P_{capillary}}$ depending on the burst scenario.

Burst frequency dependent on liquid entering the channel (ideally homogeneous surface):

$$\omega_b = \sqrt{2\sigma \frac{\frac{cos\theta_R}{H} - \frac{cos\theta_A}{h} + \frac{cos\psi_R}{H} - \frac{cos\psi_A}{h} + 2(\frac{cos\theta_R}{W} - \frac{cos\theta_A}{w})}{\rho(r_2^2 - r_1^2)}} \tag{5}$$

Burst frequency dependent on liquid exiting the channel (ideally homogeneous surface):

$$\omega_b = \sqrt{2\sigma \frac{\frac{cos\theta_R}{H} - \frac{cos\theta_A^*}{h} + \frac{cos\psi_R}{H} - \frac{cos\psi_A}{h} + 2(\frac{cos\theta_R}{W} - \frac{cos\theta_A^*}{w^*})}{\rho(r_3^2 - r_1^2)}} \tag{6}$$

Burst frequency approximation with fluid front at channel middle (surface imperfections):

$$\omega_b = \sqrt{2\sigma \frac{\frac{cos\theta_R}{H} - \frac{cos\theta_A}{h} + \frac{cos\psi_R}{H} - \frac{cos\psi_A}{h} + 2(\frac{cos\theta_R}{W} - \frac{cos\theta_A}{w})}{\rho(r_m^2 - r_1^2)}} \tag{7}$$

The advancing contact angle between liquid and air is θ_A and the advancing contact angle at a cross-section change is $\theta_A^* = \min\{\theta_A + \beta, 180°\}$, where β is the expansion angle of the channel opening. θ_A^* is limited by the maximum attainable contact angle of a fluid, which is 180°.Therefore, large expansion angles or high advancing contact angles lead to the same burst frequency in Equation 6. Further variables are, θ_R, the receding contact angle in the burst geometry, ψ_R and ψ_A, the receding and the advancing contact angle with the top adhesive, h the height of the channel, H the height of the chamber, w the width of the channel, and W the width of the chamber at the receding fluid front. $w^*$is the corrected channel width in the case of a gradual channel opening (see Figure 12b). A graphical representation of variables can be found in Figure 11.

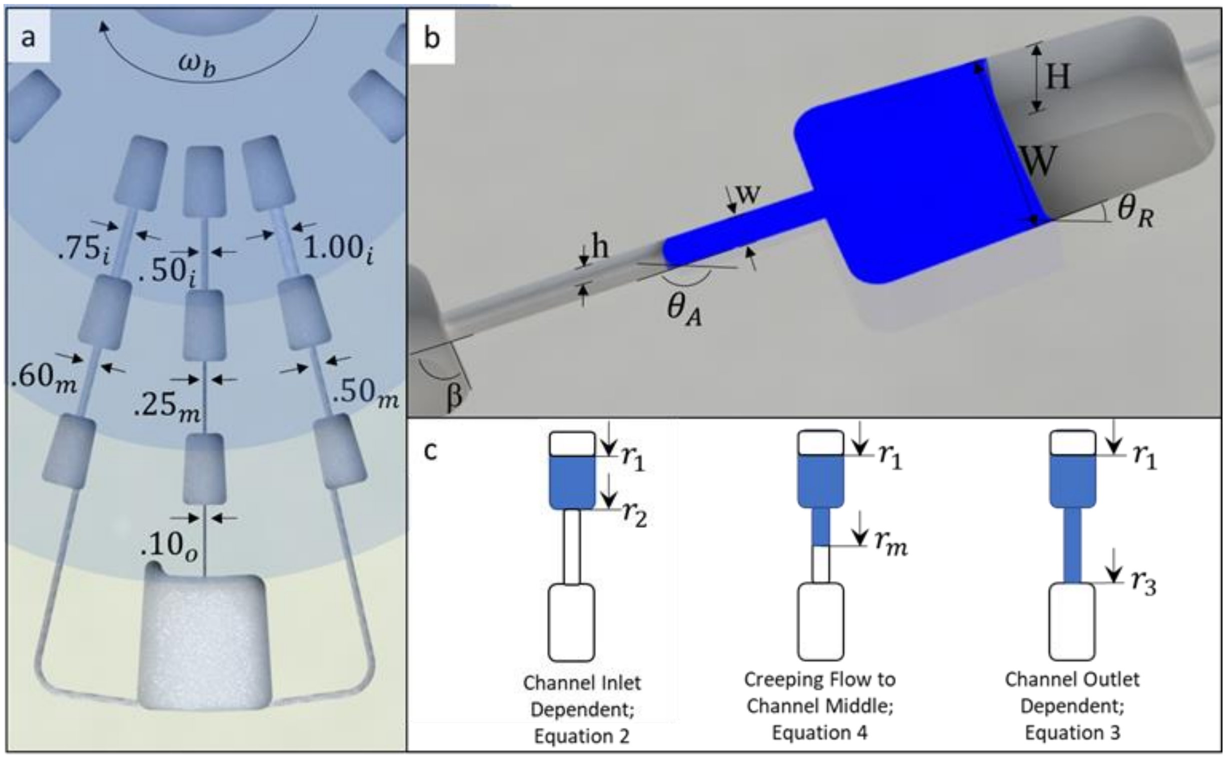

Figure 11: a) Channel layout on tested parts and widths of channels with nominal channel width in mm. Channel widths subscript relates to distance of the valve from the center with subscript i indicating a distance between center and channel inlet of 20mm, subscript m indicating a distance of 30mm and subscript o indicating a distance of 40mm; b) Variables

in burst frequency calculation; c) Schematic of burst scenarios with (left to right) burst dependent on liquid entering the channels, liquid creeping into the channel along imperfections, and burst dependent on liquid overcoming capillary holding forces at the channel outlet.

4.1.3. Experimental Methods

4.1.3.1. Fabrication of Channels

To measure the predictability of burst valve behavior we produced burst valve geometries with different prototyping and manufacturing techniques (3D printing via material jetting on Objet260 Connex3, Stratasys, Ltd; CNC milling on Haas VF2, Haas Automation, Inc.; rapid injection molding (RIM) on AB-200 Plastic Injector, AB Plastic Injectors, Inc.). While CNC machined discs were fabricated in a disc layout with 6 test patterns per disc, molded and printed parts were made in the shape of wedges and attached to a holder for testing. The channel and chamber geometry of the valves on the CD wedges, is the same as on CNC and laser machined discs, as is the distance of all structures to the center of rotation. The geometry of the valve layout is shown in Figure 12a) and consists of 7 burst channels at 3 different distances from the center, 20mm, 30mm and 40mm (indicated in the subscript of the channel widths in Figure 11a). Channel depth was kept constant at 100µm, while channel width varied. Chambers are 1mm deep. CNC machining of molds for injection molding resulted in 400µm radii at channel ends. To compare behavior directly and study the impact of radii at channel ends, half of the CNC machined discs were fabricated without radii as well as half with 400µm radii at channel ends. While actual channel widths were measured and averaged for each part for the calculation, depths were assumed at nominal value.

Given that the tested geometry only contains expansion angles of 90° at the channel outlet, the default value of β is 90°. For parts with radii at the channel ends, β was based on the tangent to the channel curvature at the point of contact of the fluid front right before burst (see Figure 12b), as opposed to 90° cross section change in Figure 12a), measured on a CNC machined poly(methyl methacrylate) (PMMA) part). Based on the same figure, the channel width at the location of the cross-section change was adjusted to account for a gradual channel opening. Figure 12 furthermore shows measurements of the resulting expansion angle and burst channel width right before burst. Based on the measurements, the corrected width w^* is 450μm wider than the channel width w and expansion angle β is 61.5°. For simplicity, these values are assumed to be the same for all parts containing radii. For calculations and graphs, dimensions and contact angles were averaged for each part.

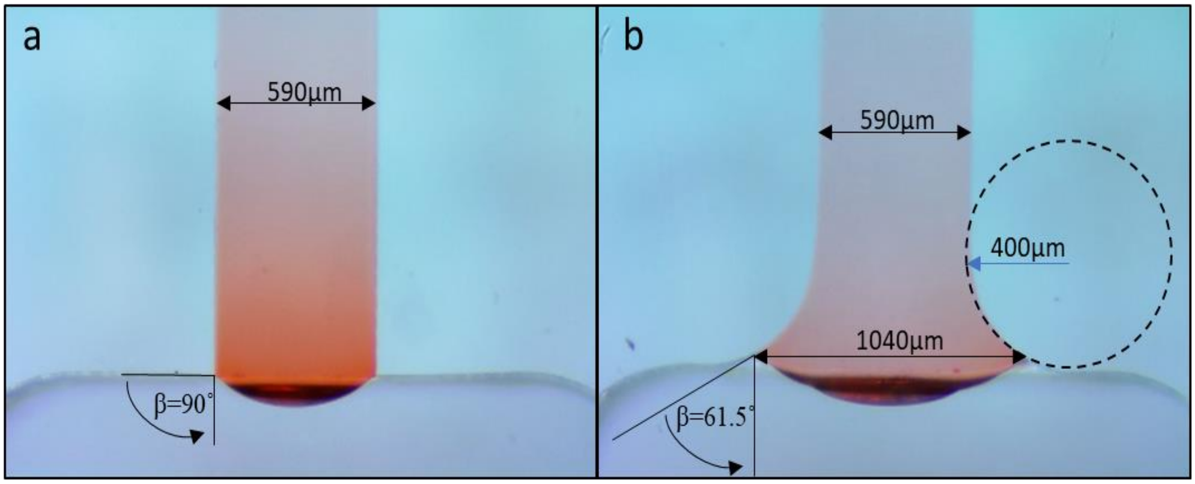

Figure 12: Optical microscope images of channel $.25_m$ in PMMA CNC milled disc with dyed 1xPBS solution right before burst in parts with a) no radius at channel ends b) 400μm radius at channel ends; resulting expansion angles, β and width, w^*

4.1.3.2.Molding of Burst Valve Geometry

In order to fabricate quick and affordable molded parts, a mold consisting of 4 main elements (Ejector Plate 1 and 2, A half and B half see Figure 13) was fabricated. The mold was designed such that the molded part remains attached to the B half once the mold is separated. Hitting against the Ejector plate 2 with a hammer allows for the ejector pins to separate the part from the B half of the mold. Channel and chamber features were only placed on the A half of the mold, a design change (given the same contour as defined by the B half) can therefore be made by simply providing a new A half. Molding was done on an AB-200 Plastic Injector (AB Plastic Injectors, Inc, Saint-Laurent, Canada). This molding machine is a very simple to use tabletop device which can inject up to a volume of about 7g. Limitations were found when molding PMMA as compared to PC, MX711(not evaluated in burst valve experiments) and PP. Molding errors observed were short shots, sink marks, and flow lines. It is assumed that short shots and flow lines in PMMA parts were due to too slow injection speeds for this material, allowing the plastic to cool down prematurely and sink marks due to material shrinkage especially in areas of increased thickness. Premature cooling is furthermore likely as the mold is not heated and depending on duration of use will have varying temperature. Finally, short shots are likely due to low viscosity of PMMA in the mold and approaching of the maximum volume per shot (about 5.5g per shot).

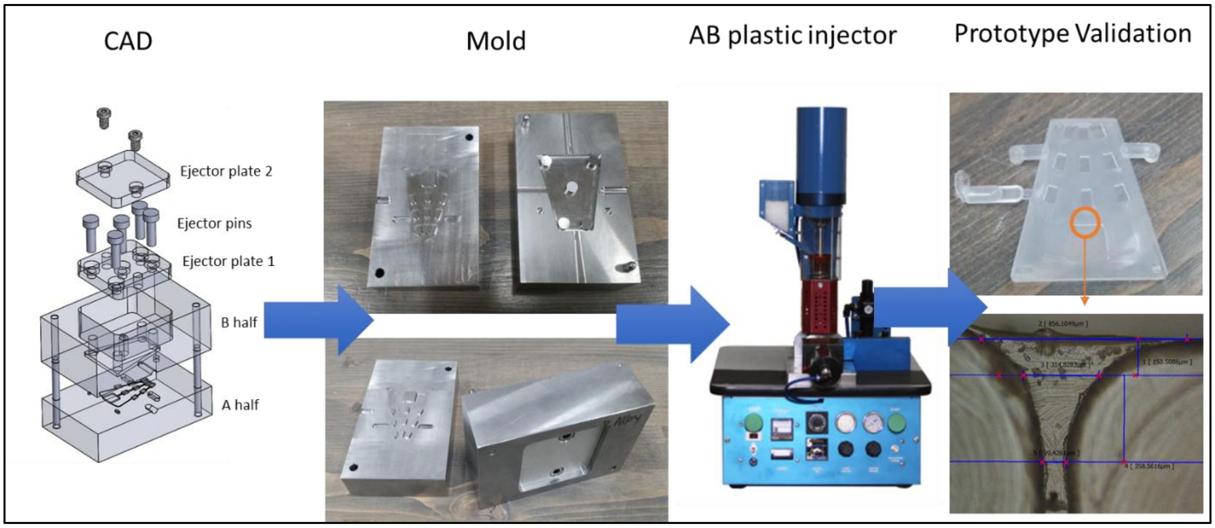

Figure 13: Process for producing molded parts of this work: left to right – 3D Model of mold components, machining of physical mold, molding of plastic granules plastic injector, measurement and analysis of molded parts

4.1.3.3.Measurement of Contact Angles

For every part, six measurements for each, static, advancing and receding contact angle were taken, the results of which are shown in Table 5. Static contact angles were averaged using a 2μl sessile drop measurement, while advancing and receding contact angles were obtained according to the method proposed by Korhonen et al.[90]. This consisted of using the needle-in-sessile-drop method with larger fluid volumes of at least 60μl, and taking measurements right before the contact line increase in the case of advancing contact angle, and right before the contact line decrease in the case of receding contact angle[90]. While only advancing and receding contact angles are used for the calculation, static contact angle measurements were taken as a control. The adhesive used to close the channels (ARCare90445) was obtained from Adhesives Research, Inc. All calculations consider the average measured contact angle of a part.

Table 5: Contact angle measurements in degrees with 1x phosphate-buffered saline (PBS) solution (Drop Shape Analyzer DSA25, Kruess GmbH); Standard deviations in measurements are indicated in parenthesis

Material - Manufacturing technique	**Static contact angle (Standard deviation) [°]**	**Advancing contact angle (Standard deviation) [°]**	**Receding contact angle (Standard deviation) [°]**
Polycarbonate (PC) - CNC milling	96 (1.4)	109 (0.9)	23 (1.2)
PC - Rapid injection molding	89 (4.5)	96 (3.6)	23 (1.1)
PMMA - CNC milling	75 (5.0)	85 (1.9)	17 (1.1)
PMMA - Rapid injection molding	78 (3.7)	87 (3.9)	23 (5.5)
PP - Rapid injection molding	79 (1.5)	95 (1.4)	23 (3.1)
VeroClear glossy - Material jetting	85 (2.0)	95 (2.6)	32 (2.3)
Adhesive	96 (3.5)	123 (3.2)	22 (2.1)

4.1.3.4. Measurement of Burst Frequencies

To determine burst frequency of the channels the parts were mounted onto a CD microfluidics spin stand with visualization system. The visualization system consisted of a trigger, a strobe light and a high-speed camera as described elsewhere [35]. A piece of reflective tape was adhered to the spinning platform to activate an optical trigger once per revolution. The highspeed camera was controlled by this trigger to take one image per revolution and a strobe light provided illumination of the setup to enable short exposure times. This visualization setup thence allowed for observation and recording of videos of the burst experiments. For burst experiments parts were first cleaned with soap, rinsed with deionized water and finally dried with air. Next, parts were assembled with the top adhesive, the latter containing fill holes in all chambers, and providing an additional vent hole at the bottom chamber, for injection molded and printed parts. CNC machined parts included vent and fill holes in the discs and were sealed with an adhesive without holes. Next 10µL of dyed PBS were loaded per chamber with liquid being placed towards the channel inlet (only chambers at the same distance from the center were tested at the same time to enable proper venting). Spin speed was then increased in 20 rounds per minute (RPM) steps with about 5s delay at each spin speed until burst of all tested valves. The spin speed at burst was recorded to be the burst frequency of the respective valve. Burst frequency results were averaged for each channel with a minimum of 6 experiments per channel (any experiments with undesired location of the fluid after loading, such as air between liquid and channel inlet, as well as experiments with premature leakage of fluid into the channel during loading were repeated). All tests were conducted with 1x phosphate-buffered saline (PBS) solution.

4.1.4. Results and Discussion

4.1.4.1.Comparison of Predicted and Experimental Burst Frequencies

Figure 15 illustrates the calculations for channel $.75_{\mathrm{i}}$ of a rapid injection molded PMMA part. Capillary pressure is shown at the channel inlet (equal to the capillary pressure through the channel) and outlet (yellow and blue, dashed lines respectively) and centrifugal pressures are given for fluid front at channel inlet, middle of channel, and channel outlet (green dashed, red, and blue dashed curves respectively). The receding fluid front is assumed to be at a constant position due to the much smaller volume of the channel compared to the chamber. Intersects of centrifugal pressure curves and capillary pressure lines are marked by C.M., EXP, C.O., and C.I., indicating predicted burst frequency assuming liquid creeping into channel along imperfections, experimental result, result for burst pressure based on Equation 5, and Equation 6 respectively. While based on a part with ideal surface homogeneity the valve from Figure 15 would burst according Equation 5 (marked C.I. in Figure 15) at 15.4 rounds per second (RPS), the approximated scenario of liquid creeping into the channel along surface imperfections (titled C.M. in Figure 15) predicts the experimental burst frequency much closer with 11.3RPS predicted compared to 11.7RPS experimental burst frequency. This trend is similar across manufacturing methods and materials and leads to valves generally bursting at lower than predicted values when basing predictions on the maximum result of Equation 5 and Equation 6, while predicting slightly lower burst frequencies based on Equation 7. A similar observation was obtained by Cho et al. (2007) who suggested the deviations to be due to surface imperfections. A comparison of predicted (blue, left columns) and experimental data (orange, right columns) for PMMA and polycarbonate (PC), each CNC milled and rapid injection molded parts and only considering ideal surfaces, is given in Figure 14.

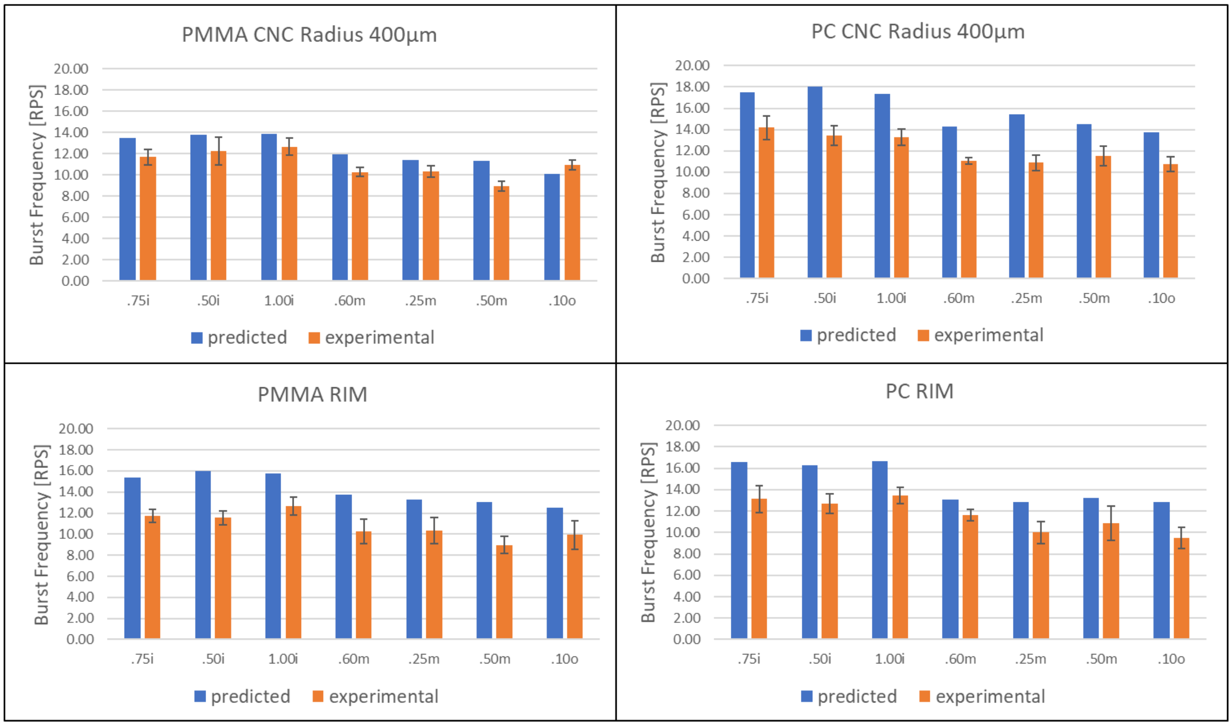

PMMA CNC Radius 400µm

PC CNC Radius 400µm

PMMA RIM

PC RIM

Figure 14: Maximum predicted burst frequency in RPS and respective experimental results for PMMA and PC parts, CNC milled and rapid injection molded

The average deviation between thusly predicted and experimental burst pressure was 20.0% for CNC milled (PC and PMMA with 400µm as well as with no radius at channel end) and 18.3% for rapid injection molded (PMMA, PC, Polypropylene (PP)). This deviation of predicted and experimental data is reduced to 7.1% and 10.4% for CNC milled and rapid injection molded parts respectively with predictions based on Equation 7. Figure 16 compares predicted and experimental burst frequencies for calculations based on Equation

7. Predicted values are shown in blue (left column of each pair) and experimental data (orange, right column) includes error bars depicting standard deviations of experimental burst frequency measurements. Both prediction methods agree in their trend with the experimental data, suggesting lower burst frequencies for channels farther away from the center due to the higher centrifugal pressure.

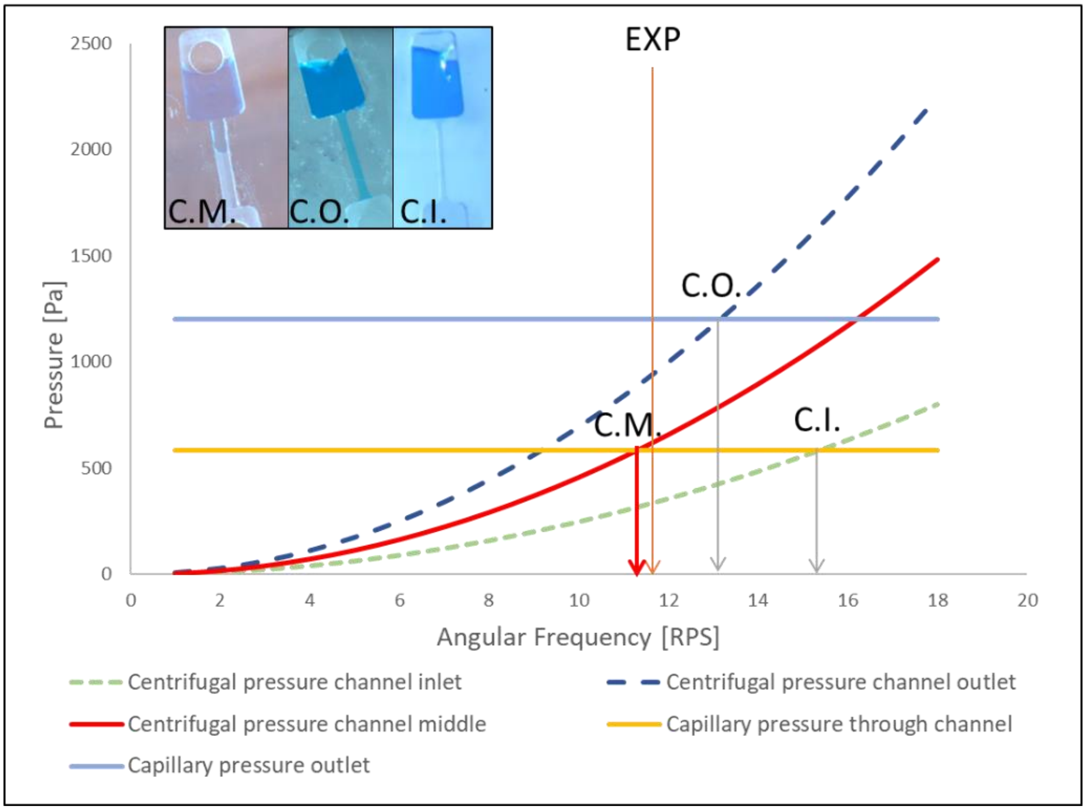

Figure 15: Pressures for fluid flow through channels in rapid injection molded PMMA part, channel $.75_i$; C.M.: Burst pressure based on fluid front at channel middle according to Equation 4, EXP: Experimentally obtained, averaged burst pressure, C. I.: Burst pressure according to Equation 5, C.O.: Burst pressure according to Equation 6

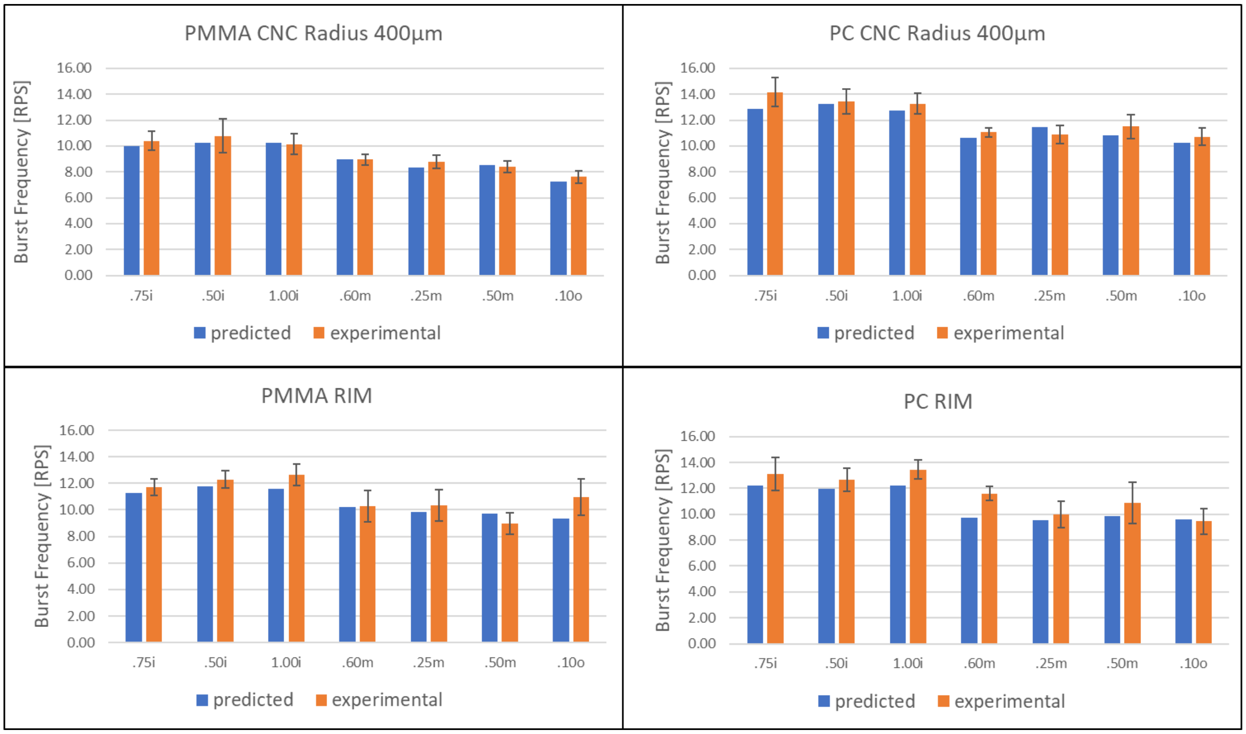

Figure 16: Predicted burst frequency in RPS and experimental results for channels on PMMA and PC parts, CNC milled, and rapid injection molded. Predicted values are based on Equation 7

4.1.4.2. Discussion of Factors influencing Burst Pressure

Materials and manufacturing techniques:

Figure 17 shows the average burst pressures for different parts, with error bars depicting the range of the burst pressures for the 7 different channels per part. Thus, 3D printed parts generally tend to burst at the lowest centrifugal pressure, while PP rapid injection molded parts burst at the highest pressures. The presence of radii at channel ends in PMMA CNC machined parts leads to a lower burst pressure as compared to the same parts without radii, while PC CNC machined parts with radii increase in burst pressure as compared to their radii free counterparts. Injection molded PC and PMMA parts are shown to be well approximated by PC CNC machined prototyping parts without radii.

From the size of the error bars in Figure 17 (indicating the change in burst pressure for channel widths varying between 0.1mm and 1mm, with channel height constant at 0.1mm), it can be concluded that channel dimensions have only a small effect on burst pressures when compared to the impact of material or manufacturing method. This is especially true as standard deviations for burst frequencies of the same channel on the same part ranged between 9.5% and 17.3%, which is sometimes higher than the expected burst frequency difference between channels of 0.1mm and 1mm width. For exact standard deviations see Table 6.

Table 6: Standard Deviations of experimental burst frequencies within part groups

Part	**Standard Deviation in RPS**	**Standard Deviation in %**
PMMA CNC No Radius	0.98	9.53%
PMMA CNC 400μm Radius	1.35	13.84%
PC CNC No Radius	1.88	16.43%
PC CNC 400μm Radius	1.57	12.92%
PMMA RIM	1.90	17.25%
PC RIM	2.01	11.61%
PP RIM	1.49	17.34%

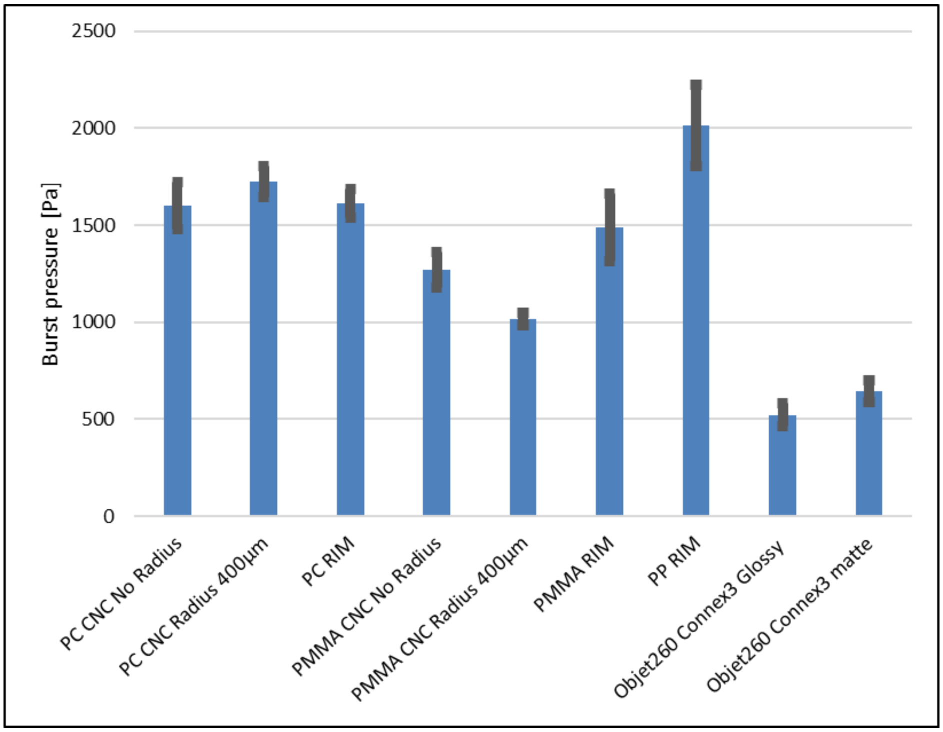

Figure 17: Average experimental burst pressure for tested parts with error bars representing the range of burst pressures for varying channel widths

As prototyped microfluidics often involve an adhesive cover, its influence needs to be evaluated when moving to a single material injection molded design. Figure 18 shows the difference between burst frequency of a PMMA rapid injection molded part with adhesive cover and with a cover of the same plastic. The burst frequency decreases by about 27% in average due to the higher hydrophobicity of the adhesive as compared to rapid injection molded PMMA.

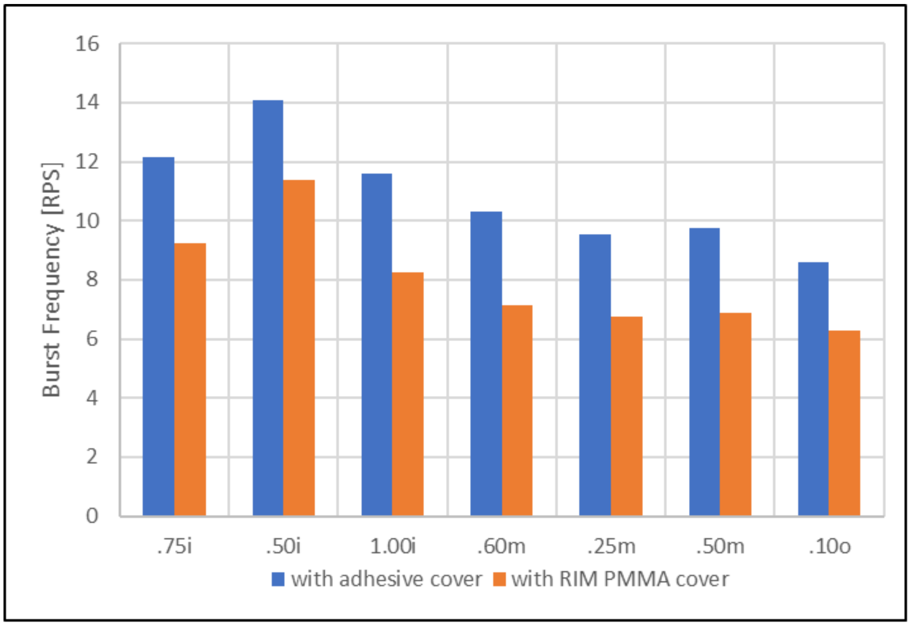

Figure 18: Example of PMMA rapid injection molded part: Influence of replacement of the adhesive cover with a PMMA rapid injection molded cover

Channel Widths:

High standard deviations as shown as error bars in Figure 16 and low impact of channel widths onto burst pressures, leave the burst valve at risk of malfunctioning by bursting at a too low or too high pressure. Inaccurate burst pressures need to especially be avoided in designs that combine multiple valves in series, which are opened at different points in time. The small difference in burst frequency between channels of varying width is due to the range of widths generally feasible with common manufacturing techniques for low cost disposable systems. According to our calculations, as well as data by Cho et al.[82], burst pressure increases drastically in channels of width and height below 100µm. The graphs in Figure 19 show the predicted burst pressure for PC rapid injection molded parts with an adhesive cover. While only a single channel height was used in our experiments, predictions suggest an even larger increase in burst pressure by reduction of height, than reduction in width. This is due to the higher contact angle of the top adhesive.

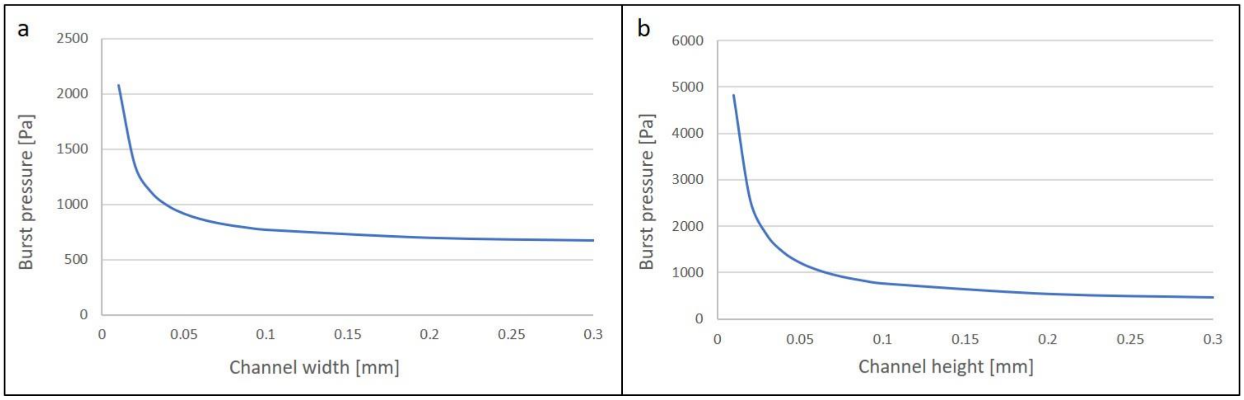

Figure 19: a) Effect of decrease in widths for parts with constant channel depth of 0.1mm onto burst pressure. Calculation based on PC rapid injection molded part; b) Effect of decrease in channel height with constant channel widths of 0.1mm; Decrease in height has more effect due to hydrophobic top adhesive

Due to the increase in burst pressure for smaller channel dimensions, larger differences in burst pressure can be achieved when combining multiple burst valves on the same platform. However, channel widths below 0.1mm are often hard to fabricate with standard manufacturing methods. One approach could be decreasing channel depths rather than widths. However, maintaining reproducible channel depth is also difficult when additional sealing steps such as ultrasonic welding, laser welding or thermal bonding follow. Small deviations from nominal dimensions are especially impactful as the burst pressure becomes increasingly sensitive to changes in widths or depths at smaller dimensions. Therefore, thorough dimensional control becomes inevitable. When considering deviations from nominal dimension in prototyped parts in this work (Table 8), it might be difficult to obtain channels of sufficient accuracy with the evaluated manufacturing means.

Table 8: Accuracy of Manufacturing. Nominal and actual dimensions for parts of different material and manufacturing technique, measurements taken via confocal microscope VK-X200K, Keyence, Corp.

Channel	**Nominal Width**	**Measured Width**						
		CNC PMMA	CNC PC	PMMA Laseretched	RIM PP	RIM PC	RIM PMMA	3DP VeroClear glossy
$\mathbf{.75}_i$	0.75	0.73	0.70	0.63	0.72	0.71	0.72	0.60
$\mathbf{.50}_i$	0.50	0.48	0.43	0.41	0.46	0.44	0.43	0.28
$\mathbf{1.00}_i$	1.00	0.98	0.94	0.84	0.83	0.77	0.81	0.72
$\mathbf{.60}_m$	0.60	0.59	0.55	0.51	0.57	0.57	0.56	0.30
$\mathbf{.25}_m$	0.25	0.27	0.23	0.15	0.23	0.21	0.19	0.16
$\mathbf{.50}_m$	0.50	0.48	0.44	0.37	0.52	0.48	0.50	0.26
$\mathbf{.10}_o$	0.10	0.18	0.17	0.11	0.08	0.07	0.05	0.15
	Nominal Depth	**Measured Depth**						
		CNC PMMA	CNC PC	PMMA Laser-etched	RIM PP	RIM PC	RIM PMMA	3DP VeroClear glossy
$\mathbf{.75}_i$	0.10	0.12	0.12	0.08	0.09	0.09	0.11	0.12
$\mathbf{.50}_i$	0.10	0.12	0.12	0.07	0.10	0.10	0.10	0.12
$\mathbf{1.00}_i$	0.10	0.12	0.12	0.09	0.10	0.09	0.10	0.11
$\mathbf{.60}_m$	0.10	0.12	0.11	0.09	0.09	0.10	0.08	0.12
$\mathbf{.25}_m$	0.10	0.10	0.11	0.05	0.10	0.12	0.09	0.08
$\mathbf{.50}_m$	0.10	0.12	0.11	0.07	0.10	0.10	0.08	0.12
$\mathbf{.10}_o$	0.10	0.11	0.11	0.03	0.10	0.10	0.10	0.06

Distance from Center of Rotation:

An alternative to changing capillary burst pressures of burst valves by geometry, material, or surface topography, specifically for CD microfluidics, is varying centrifugal pressures by placing valves at different distances from the disc center. The effect of this can be seen in Figure 16 when comparing burst frequencies of channels closer and farther away from the center. For example channel $.50_m$ is located at a distance of 30mm from the center as compared to $.50_i$ at a distance of 20mm from the center, which increases average burst frequency by over 15% for $.50_i$ as compared to $.50_m$ (based on average of CNC machined and rapid injection molded parts). Channels in position of $.10_o$ generally require lowest rotational frequency but in our experiment were chosen to have the smallest width at 0.1mm.

Shape of Channel Cross-Section;

As discussed by Zeng et al.[85] and Glière and Delattre[84] , channel shape does have considerable impact on burst frequency. When comparing CNC machined and rapid injection molded parts (see Figure 20) it can be seen that CNC machined parts have very steep channel sides while rapid injection molded parts have sloped channel sides. While our mold for rapid injection molding did have straight channel walls, the sloped shape is caused by the manufacturing technique itself and should be taken into account when developing reliable burst valves.

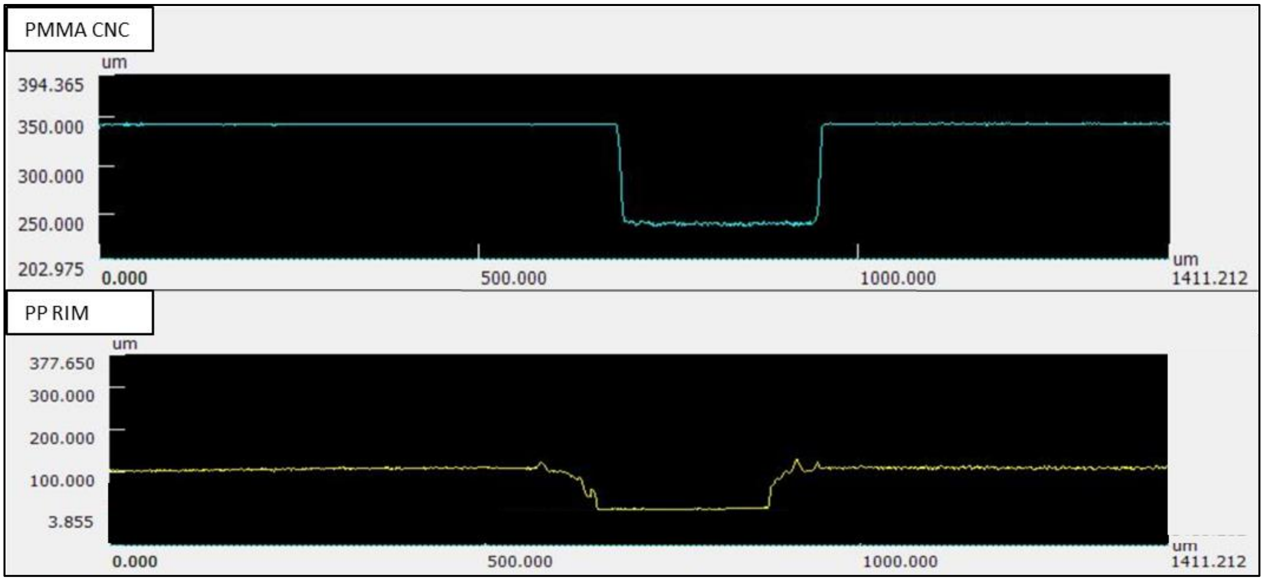

Figure 20: Surface Profile of channel E in a PMMA CNC machined and a PP rapid injection molded part measured with confocal microscope VK-X200K, Keyence, Corp.)

Hydrophilicity:

In our comparison, burst pressures were impacted by manufacturing technique as well as by material. Manufacturing technique affects burst pressure through differences in channel end geometries as in the case of rounded corners at channel ends and the shape of the channel cross-section, as well as through changes in contact angles (static, advancing and receding) through different surface topography and surface roughness. For example, CNC milled PC showed an advancing contact angle of 109° while rapid injection molded PC showed an advancing contact angle of 96°. This is in agreement with Chen et al.[83], who describe an increase in contact angle for hydrophobic (contact angle >90°) materials for increasing surface roughness. In our tests CNC milled surfaces tended to follow the air-solid composite effect of the Cassie-Baxter state, which describes reduced surface wetting for surfaces with increased surface topography[91], while rapid injection molded parts behaved according to the

Wenzel state in which the fluid is in contact with the entire surface and hence increases in hydrophilicity as roughness increases for surfaces with <90° contact angle. When a material is hydrophobic to start with (contact angle >90°), hydrophobicity will be further enhanced in Cassie-Baxter as well as in Wenzel state[92].

Although the differences we measured between values of advancing and receding contact angles, thus the contact angle hysteresis, are quite high, they are not unreasonable in the light of existing published results. For instance, Busscher et al.[93] measured a 40° hysteresis on a PMMA surface with low surface roughness (for DI water, the advancing contact angle was approximately 80°and the receding contact angle approximately 40°). Bormashenko et al.[94] studied surfaces such as polyethylene, PP, polyethylene terephthalate (PET) and polysulfone, and observed contact angle hysteresis values as high as 53°on polysulfone and 44° on PET when using the needle-syringe method.

4.1.5. Conclusion

We demonstrated a prediction method for burst pressure of burst valves, which follows the trend obtained in experiments with channels of width between 0.1mm and 1mm. The calculation was based on a design with significant channel length (5mm) and channels at three different distances from the center. Since fluid has to pass both, channel inlet and channel outlet, the location which requires higher spin frequency was expected to determine the overall burst of a channel with ideally homogeneous hydrophobicity. However, the thusly predicted burst frequencies tended to be higher than the experimental values. A better agreement of calculation and experiment for prototyped parts was obtained when assuming a burst event occurring when the fluid front reaches the middle of the respective burst channel. This behavior was observed in experiments and is assumed to be due to fluid prematurely advancing into the channel due to inhomogeneous hydrophobicity/surface imperfections. Generally increasing head height (as fluid advances into the channel which is much narrower and shallower than the chamber) leads to higher driving pressure thus aiding to liquid advancing at lower spin speeds. Liquid momentum may further contribute to liquid overcoming the holding forces at the channel outlet but was not specifically considered in the presented calculations.

Furthermore, it was found that the material type and fabrication method had the biggest effect on the valve break pressure and frequency, with a factor of four difference in break pressure between the highest and lowest values. That means that prototyping before production of any part needs to use the same material and fabrication method, or that the offset between prototyping and production methods must be previously established. Otherwise, multiple design iterations will likely be required.

Contrary to our expectations, the valve geometry had only a limited effect in the studied range, smaller than that of the material and fabrication method. The derived model indicates that this is due to the large dimensions of the tested channels. Only in the sub 100μm range is there a strong effect of channel dimensions, and most methods available for prototyping or manufacturing do not allow accurate dimensional control in this size range.

Since changes in widths of channels above 100μm have only little influence on burst pressure, and because standard deviations in burst events are high, burst valves in commercial microfluidic systems which are based on common fabrication processes (usually only capable of reliably achieving dimensions >100μm) should be critically evaluated. It will be very difficult to achieve large enough differences in burst frequency as needed to reliably actuate multiple burst valves in series. Using dimensions well below 100µm will cause large differences but will also increase the already high variability of the burst frequency if the dimensional control is not extremely accurate.

Another solution for the implementation and precise control of multiple burst valves, in the case of CD microfluidic platforms, is positioning of burst valves at different distances from the center of the disc, thus varying the centrifugal pressure at the location of the valves, rather than changing the capillary burst pressure.

Overall, much care should be applied when attempting to prototype a microfluidic burst valve design for further implementation into a mass manufactured product. Even if dimensions are identically transferred from prototype to injection molded part, surface topography and hydrophobicity can have major impact on burst pressures, as can manufacturing accuracy. The authors therefore recommend reducing the number of passive burst valves to a minimum or alternating them with siphons. Each burst valve should be designed for a large window of allowed burst pressure, to account for deviations from expected values. Alternative passive valves such as serial siphon valves or passive check valves together with a mix of active valving should be employed for robust fluidics in complex systems[71,95].

4.2. Laser Valve

One active valve approach which does not require physical interfaces or additional materials (such as wax) in the fluidic system for actuation are laser valves. Laser valves are based on the principle of selective melting of a heat sensitive (e.g. thermoplastic) film separating adjacent parts of a channel. In CD microfluidics this is easily achieved by integrating channels in a top and a bottom layer of the disc while separating them with a thin middle layer which once melted opens the valve.

Laser valves on the CD have previously described by Garcia-Cordero et al[96], who implement this optofluidic valve based on a clear film, thermoplastic working layer with black, printed dots. Channels are formed between this working layer and a top and bottom layer of the disc assembly. While all other disc components are clear, allowing for light from a laser to pass through, the dark areas absorb the largest amount of the light energy, thus leading to heating of the dark patch and, therefore, melting of the thermoplastic material in this area. Garcia-Cordero et al.[96] characterize the transmittance of cyclic olefin polymer (COP), PMMA, and PC for wavelengths over 400nm at approximately 90%, while printed, black spots absorbed about 99% of the light when applied in two layers of ink.

Laser valve technology is integrated and demonstrated in Section 6. The principle is illustrated in Figure 21 and utilizes a black double-sided adhesive to connect upper and lower half of the microfluidic CD. Laser intensity is regulated through increase of current and spot size can be either controlled by a lens or through changing the distance between laser and black adhesive to increase or decrease the focus of the laser beam. The less focused the laser beam, the bigger the area that is heated and the lower the intensity per area. Thus, applied current and distance between the laser and the valve determine the time of exposure to melt a given substrate as well as the size of the opening. While not demonstrated in this work, the laser can be triggered electronically to turn on and off such that valves van be opened during spinning. This will require very short exposure times for precise positioning of small holes. Alternatively, utilization of dark patches could allow for valve activation even without pulsing the laser. This is because the dark material absorbs most energy and heats up, while clear layers allow most of the energy to transmit and experience less heating. Besides avoidance of contamination through the abundance of physical interfaces, laser valves are easy to implement and to control. Unlike wax valves, laser valves are vapor and liquid tight, therefore allowing for on disc reagent storage of liquids (depending on plastics and storage times) and of lyophilized powder/pellets.

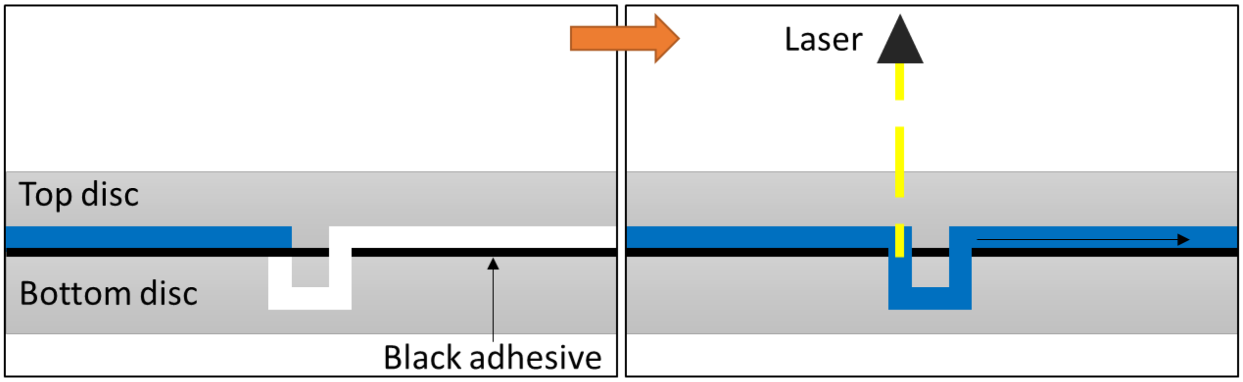

Figure 21: Principle of laser valves, energy from a laser transmits clear layers and is absorbed by a black thin film, melting a hole in the latter and allowing fluid to pass.

4.3. Fluid Reciprocation

4.3.1. Introduction

While CD microfluidic platforms inherently provide pumping pressure from the center to the rim based on the centrifugal force, the capability of reverting flow towards the center, and radial flow reciprocation are valuable additions in the microfluidic toolbox[97–100]. Reciprocating flow not only enhances mixing but also improves the lower LOD of biomarkers[98]. For example in the case of an assay utilizing a capture probe, repeated flow over a functionalized sensor area can increase the amount of analyte captured in a given amount of time[101] and therefore yield higher sensitivity, while lowering LOD. In electrochemical detection, flow provides signal enhancement through enhanced mass transport[35,102]. Furthermore, reverting and repeating flow is especially helpful when working with small sample volumes, where the volume would otherwise not suffice to provide continuous flow throughout the duration of the measurements[103].

Previous work has demonstrated an un-vented compression chamber, in which the trapped air is compressed as the liquid advances at increasing spin speeds. Subsequent decrease of the angular velocity allows the air to expand and thence pushes the liquid back towards the center. The effect is based on Boyle's law which is given in Equation 8 for an ideal gas at constant temperature.

$$p_1V_1 = p_2V_2 \tag{8}$$

With p_1 and V_1 as the pressure and volume of an ideal gas at time 1, and p_2 and V_2 as the pressure and volume at time 2. The principle of flow reciprocation through compression and expansion of air was demonstrated by Noorozi et al.[98] and the effect was amplified through addition of an elastic membrane atop of the air compression chamber[99]. Analytical modeling of the elastic membrane is discussed by Aeinevhand et al.[99]. The principle of an air compression chamber for liquid reciprocation on a microfluidic CD is illustrated in Figure 22. Other related reciprocation principles include heating of the unvented air chamber to cause expansion of the enclosed air[104] and the use of water electrolysis by an integrated electrode generating hydrogen and oxygen, thus increasing volume in a chamber and pumping the liquid back to the center[105].

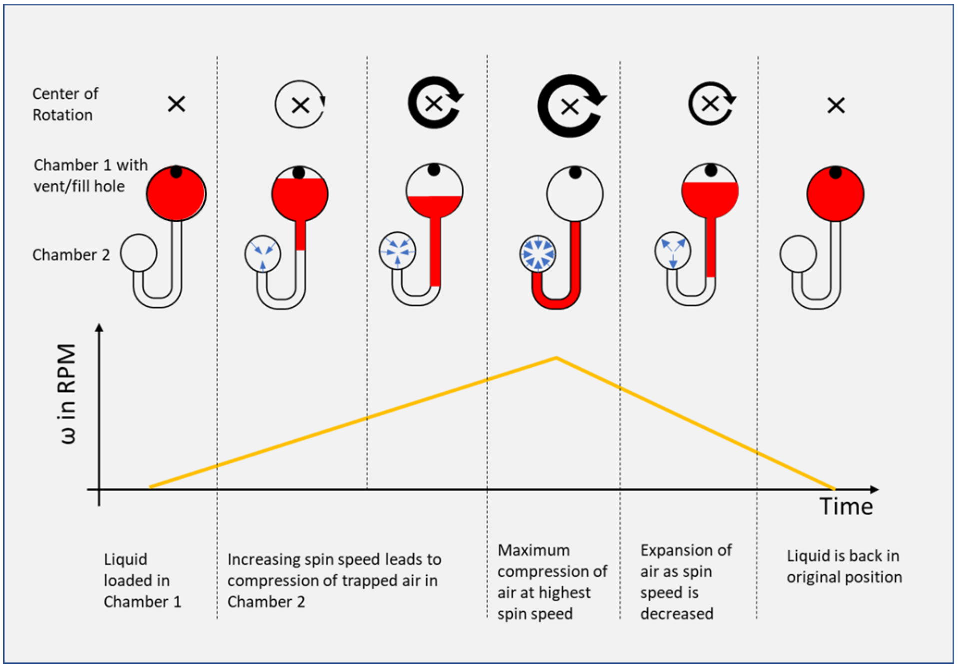

Figure 22: Basic principle of air compression chamber for (ideal) reciprocation of fluid on a microfluidic disc

Pneumatic pumping with an elastic membrane increases the efficiency of the reciprocation[99] and allows the reciprocation to take place at lower spin speeds. As a consequence, less expensive motors can be used and the bonding between CD layers endures less stress. However, the assembly process of the microfluidic disc prototypes with elastic membranes is time consuming and the CD assembly process introduced by Aeinevhand et al. includes manual alignment and adhesion of 7 different layers[99].

Here we present an approach based on 3D printing (material jetting) to prototype reciprocation inserts for centrifugal microfluidics, which enables the introduction on the CD of these dual material structures in one single step. This approach enables faster prototyping of microfluidic structures for fluid reciprocation, while printed parts resemble over-molded, mass manufactured parts. Furthermore, we demonstrate the printed structures for reciprocation-based mixing and characterize the surface of printed parts obtained by material jetting with regard to use in microfluidics. The mechanical characterization on 3D printed materials is described elsewhere[106].

4.3.2. Materials and Methods

An Objet260 Connex3 (Stratasys Ltd., Rehovot, Israel) printer was used for fabrication of the microfluidic structures used in this work. This printer is based on material jetting of UV hardening resin, in which liquid photoactive polymer droplets are expelled from a printer head and sprayed onto a building platform. The deposited droplets are then cured with UV light. After the first layer of the structure is printed, the building platform is lowered, and a second layer is built on top of the first. This process continues until the entire structure is finished. Multiple printheads allow for multi-material prints and the use of droplets of different photoactive polymers allows for the creation of material gradients.

Material jetting allows for two types of surface finishes on the top and side surfaces of a part, i.e. *matte* and *glossy*. The respective finish depends on the presence or absence of support material. Support material is sacrificial material with weaker bonds that can be mechanically (i.e. via a water jet) or chemically (dissolved by submerging the part in a solvent) removed. Print support is essential for parts that otherwise would be suspended and could not stay in place unless they are supported. If a surface is in contact with support material the surface will obtain a matte finish, while support material free surfaces result in a glossy finish.

Materials used for parts in the scope of this work are VeroWhitePlus, VeroCyanPlus (both rigid and opaque), and TangoBlackPlus (rubber-like) (all materials obtained from Stratasys Ltd., Rehovot, Israel). Parts were first designed in SolidWorks 2016 (Dassault Systemes, Vélizy-Villacoublay, France) and then exported as STL file to Objet Studio (Stratasys Ltd., Rehovot, Israel). Mixing efficiency was simulated using SolidWorks 2018 FloXpress (Dassault Systemes, Vélizy-Villacoublay, France).

The sacrificial support material in enclosed microfluidic structures (channels) could not be entirely removed. Therefore, structures were printed that are open on one side, and were then sealed with a single sided adhesive (ARCare 90445, Adhesives Research, Glen Rock, PA, USA), and attached onto acrylic holders in order to be mounted on the CD and the testing spin stand. The liquid motion on the spinning platform was visualized through a combination of a trigger, strobe light and high-speed camera as described elsewhere[35]. To demonstrate mixing, fluid reciprocating CD inserts with a woven channel geometry were produced. Furthermore, for surface characterization, inserts with different surface finish (see Figure 26) were printed with VeroWhitePlus. The nominative depths of all the channels is 1mm, while the width was varied between 0.1mm, 0.25mm, 0.5mm, 0.75mm and 1mm. After loading of 20µL dyed, deionized water in each loading chamber, burst events were observed while increasing spin speed in 10RPM steps. Each burst event was repeated 10 times and burst frequency averages and standard deviations were calculated.

4.3.3. Results and Discussion

Design of Dual Material Inserts

To assign different materials to sections of the same print, two parts were designed in SolidWorks 2016 (one for each material) and an assembly was created. Respective materials were then assigned to the different parts of the assembly in Objet Studio (Stratasys Ltd., Rehovot, Israel). Because initial designs, without securing the rubber-like membrane in the rigid part properly, led to delamination, the membrane was embedded in the rigid material as shown in the cross-sectional view of the assembly in Figure 23. The optimal thickness of the rubber-like membrane for maximum expansion while maintaining sufficient stability was found to be around 200µm.

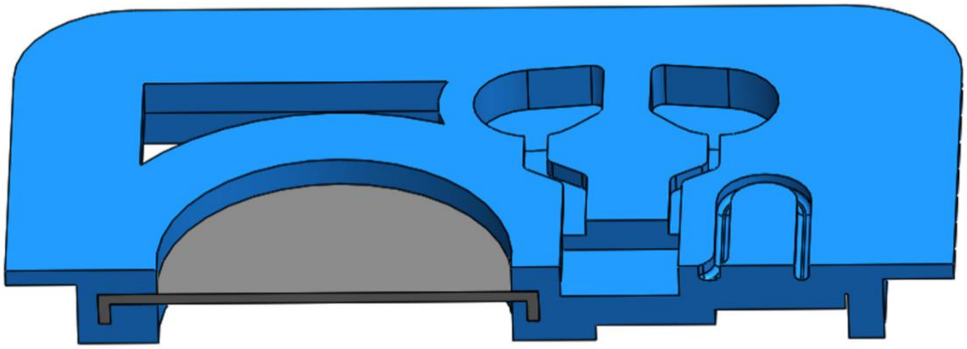

Figure 23: Embedded rubber-like membrane. Embedding the elastic membrane is necessary to avoid delamination.

Variants of Reciprocation Inserts

In Figure 24 we show the three different types of 3D printed reciprocation inserts fabricated in this work. In all designs, liquid is loaded into a fill chamber and released by increasing the centrifugal pressure over the burst pressure of the capillary burst valve. In Figure 24a the insert relies on an unvented air-chamber with a rubber-like membrane to push the fluid back to the center. Liquid reciprocation was demonstrated with this insert at spin speeds as low as 400RPM. In Figure 24b we show an insert with a straight-channel thus only utilizing elastic deformation of the rubber-like membrane for fluid reciprocation. The behavior of this membrane is further discussed in Figure 26. While this geometry does not allow to revert liquid back to its loading position, reciprocation allows for repeated flow over an area of interest close to the elastic membrane. In Figure 24c we present a mixing insert consisting of two loading chambers, a third collecting chamber that can be used for detection, and a woven channel (see Figure 25) leading to a compression chamber with an elastic membrane and finally a siphon leading from the third chamber to a waste chamber. Homogeneous mixing was visually observed after 2-3 cycles of reciprocation.

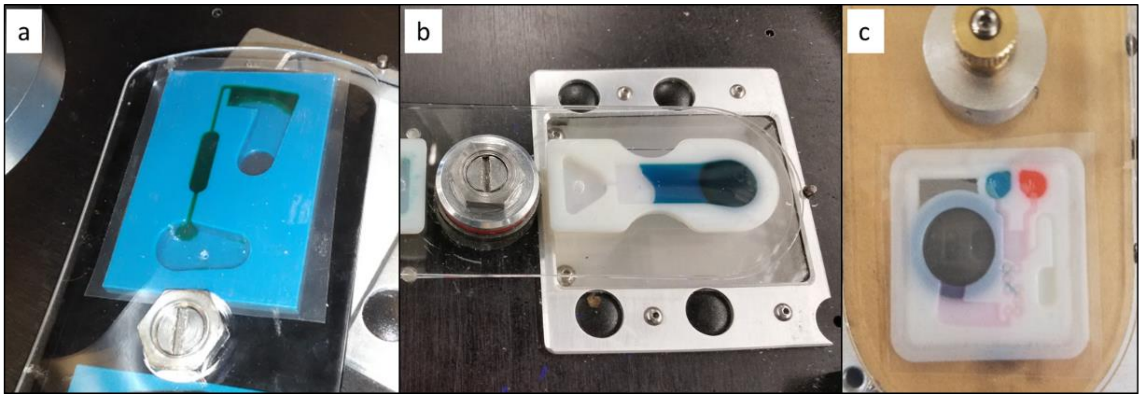

Figure 24: Three different reciprocation inserts are shown as mounted on the spin stand (the largest dimension of the inserts is between 4-6 cm): a) Reciprocation insert based on compression of air and elastic deformation of rubber-like membrane; b) Straight-channel reciprocation insert to decouple printed micro-balloon performance; c) Mixing insert allowing for mixing of two components and reciprocation of the mixture until expelled via a siphon to a waste chamber.

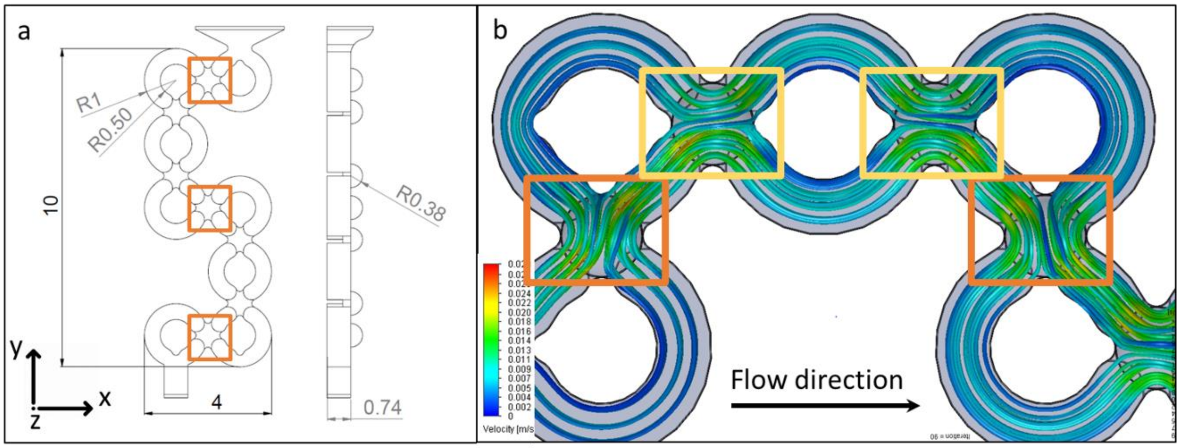

Figure 25: Channel of the mixing insert (as shown in Figure 24c) orange marks show locations of increased liquid interchange between merging and separating channels; a)

Major dimensions of the mixing channel [in mm], b) Water flow path during reverted flow simulation at a 200μL/min flow rate, yellow marks show locations with less liquid interchange between merging channels (compare over-crossing of green lines)

As shown in Figure 25, mixing was achieved through a 3D channel structure, separating and re-merging fluid elements, while changing direction in all three orthogonal directions. As observed from Figure 25b), the liquid velocity increases as the channel diameter decreases in positions where liquid streams are merged and change direction into z-direction. In locations between changes of direction of the channel-braid (marked orange) higher liquid exchange between the two streams is predicted by the simulation than in areas marked yellow (compare flow lines changing *side*). The physical 3D printed structure with glossy surface finish did not resolve suspended arcs (i.e. areas marked yellow and orange in Figure 25b) sections in as contained in the CAD model. The printed features are open towards the top surface.

<u>Reproducibility of Reciprocation</u>

To evaluate the possible fatigue of the rubber-like material, a 300μL of dyed deionized water was loaded into the straight-channel reciprocation insert (see Figure 24b) with glossy surface finish and the insert was spun reciprocating between 700 and1000RPM. After cycling between these spin speeds for 10s each over 25 rounds, the fluid location was compared to its initial location at 200RPM. As can be seen from Figure 26c) the liquid position only changed marginally, demonstrating only minor fatigue of the membrane after 26 rounds. When attempting to repeat this experiment with matte surface finish, the adhesive delaminated due to insufficient bonding with the rougher surface during steps of high liquid pressure.

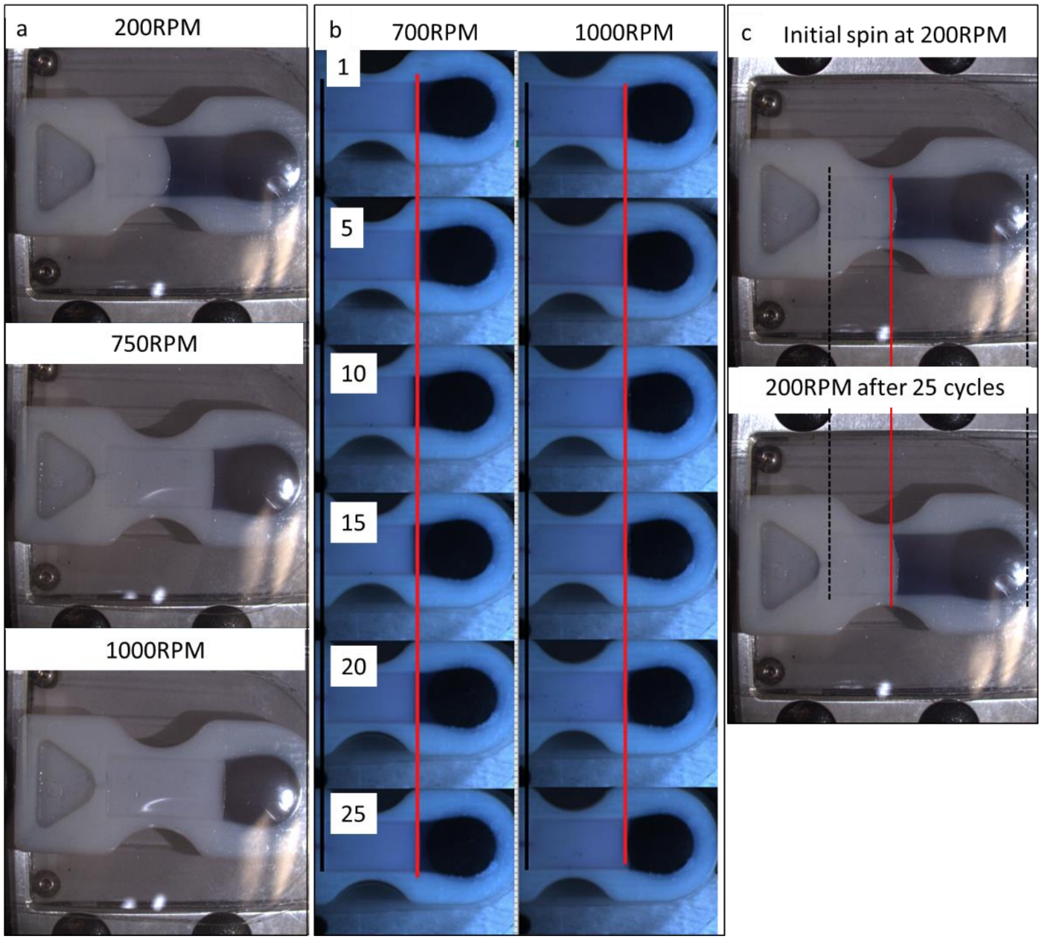

Figure 26: Minimal fatigue of rubber-like material after 25 reciprocation cycles: a) Fluid position when spinning at 200RPM, 750RPM and 1000RPM respectively; b) Reciprocation repeated between 700RPM and 1000RPM over 25 cycles. Fluid position is indicated with red line; c) Fluid position at 200RPM before and after 25 cycles between 700 and 1000RPM. Only minimal fatigue observed

Surface Characterization

To characterize the printed surfaces for microfluidic applications, 3D surface images were taken, and surface roughness was measured with a Keyence VK-X250 confocal microscope, (Keyence Corp., Osaka, Japan). Furthermore, contact angles (DI water-air interface) were analyzed with a Kruess Drop Shape Analyzer DSA30 (KRÜSS GmbH, Hamburg, Germany). The 3D images of the surfaces are presented in Figure 27, and surface roughness, and contact angles are listed in Table 7.

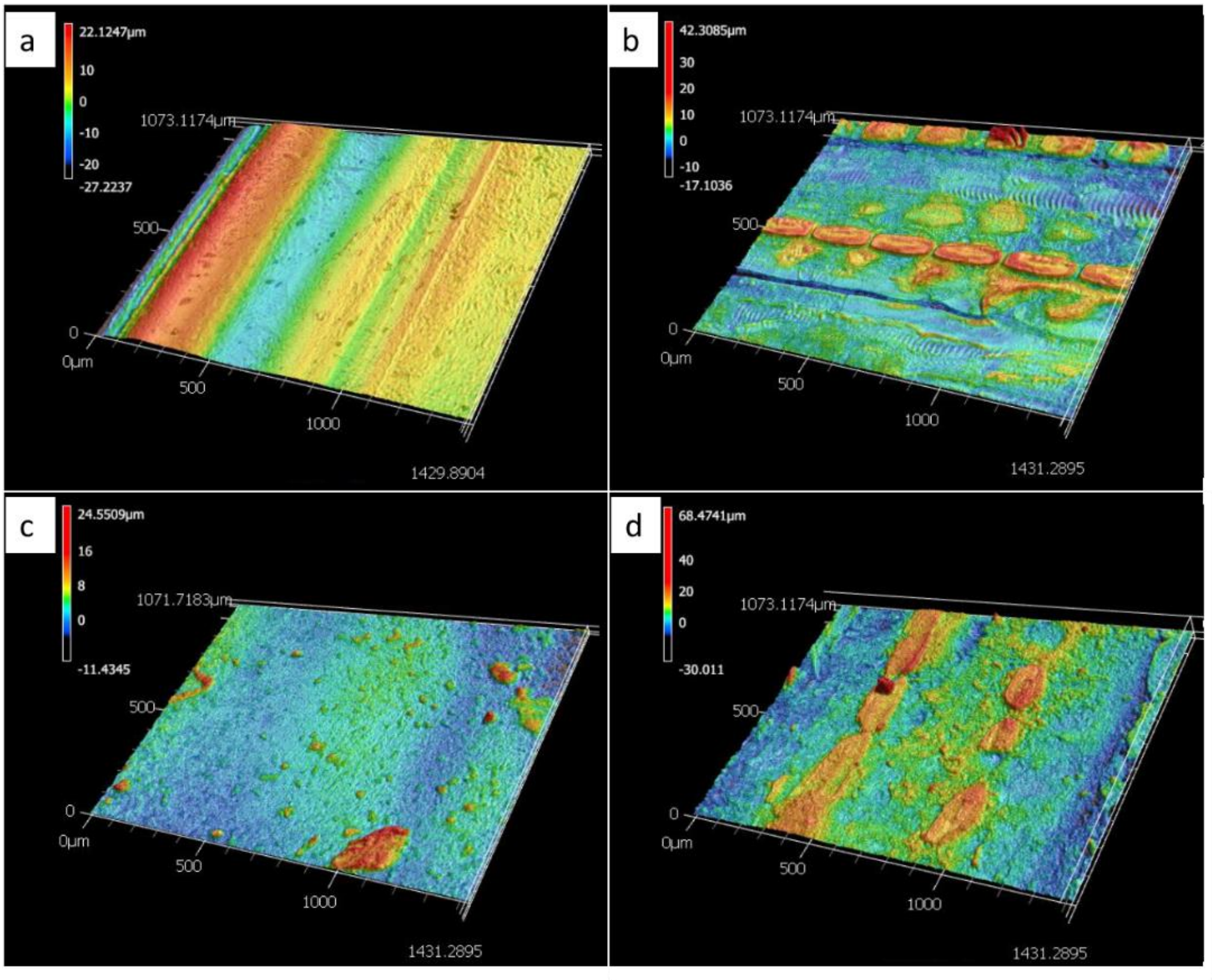

Figure 27: 3D images of surface topography of the printed surfaces, a) VeroWhitePlus, glossy, b) VeroWhitePlus, matte, c) TangoBlackPlus, glossy, d) TangoBlackPlus matte.

Table 7: Surface roughness and contact angles of printed materials. TangoBlackPlus matte was not measured as liquid spread out too quickly during measurements.

Surface	**Average surface roughness Ra[μm]**	**Average static contact angle [°]**
VeroWhitePlus glossy	5.6	94.4
VeroWhitePlus matte	3.3	105.3
TangoBlackPlus glossy	1.2	97.5

As can be seen from Table 7, surface contact with support material (i.e. matte surface finish) during the printing process not only affects the surface roughness but also contact angles. The static contact angle for matte as compared to glossy finish is more hydrophobic thus contributing to higher burst pressures for the same channel geometries (compare Figure 28d)[107]. The effect of the support material on the surface topography of the part can be gleaned from Figure 27. While the 3D scan of the matte surface in Figure 27b) shows drop-shaped material remaining as deposited by the printer head, glossy finish as shown in Figure 27a) only shows material ridges and trenches along the print direction. To further characterize the microfluidic behavior of the printed parts, burst frequency measurements were taken on the parts shown in Figure 28. Naming of channels is shown in Figure 28b) and average burst frequencies and nominal widths are shown in Figure 28c) and 28d). Standard deviations (based on 10 tests each) are shown as error bars in Figure 28d). Channel E did not resolve in the glossy surface finish part due to limited print resolution. Besides promoting a matte surface finish, utilization of support material yields higher dimensional accuracy and allows for smaller feature size. When using support material, liquid resin droplets expelled from the print head onto the outer layer(s) of the printed part, are held in position by support material in the adjacent layer. In parts with glossy surface these material droplets are able to spread and fill groves and pits before they are cured by UV light, thus affecting the resolution of features and affecting topography of the surface.

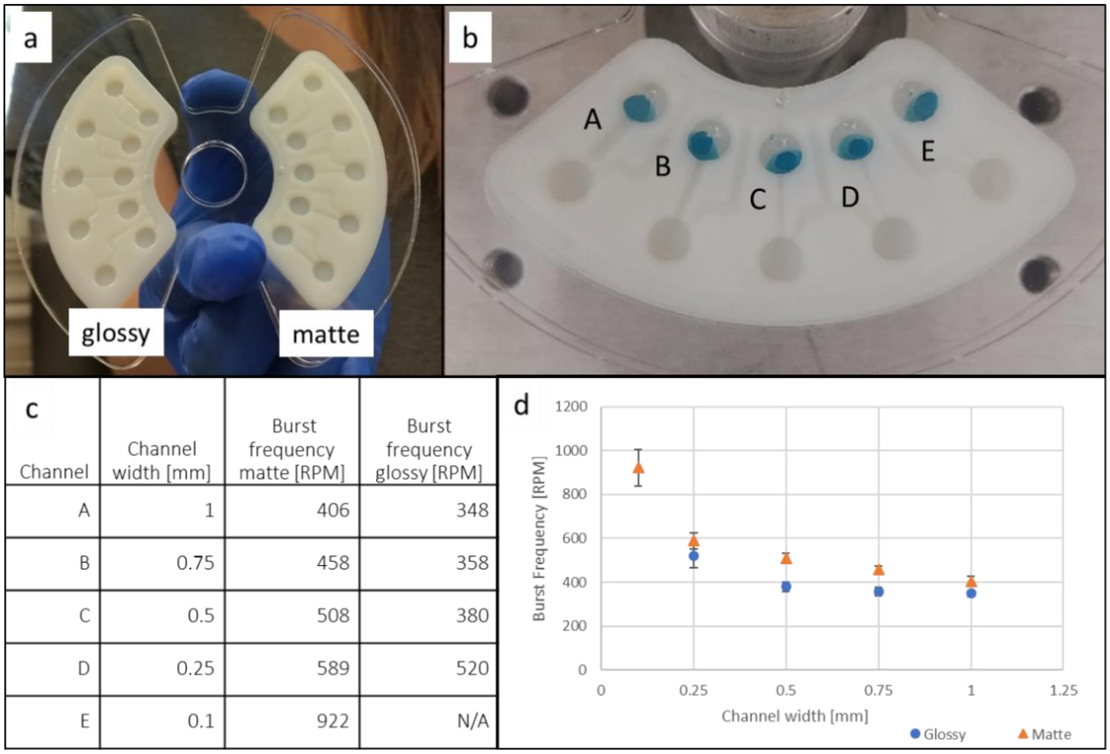

Channel	Channel width [mm]	Burst frequency matte [RPM]	Burst frequency glossy [RPM]
A	1	406	348
B	0.75	458	358
C	0.5	508	380
D	0.25	589	520
E	0.1	922	N/A

Figure 28: Burst frequency testing of 3D printed inserts with glossy and matte surface finish. a) inserts with different surface finish in a laser-cut acrylic holder; b) Naming convention of channels with decreasing channel widths left to right; c) Average burst frequencies for channels A through E. Channel E did not resolve in glossy surface finish part due to limited resolution. d) Graph of burst frequency as a function of channel width. Blue/round symbols are burst frequencies of glossy and orange/triangular are burst frequencies for the matte part. Error bars represent standard deviation. Number of tests for each channel was 10 and volume of deionized, dyed water per channel was 20μL

Overall it can be seen from Figure 29 that a more hydrophobic surface finish (matte surface) leads to higher burst frequencies and that the burst frequency increases steeply at very small channel widths as described in the burst valve theory discussed in Bauer et al.[107].

4.3.4. Conclusions

We have demonstrated reciprocation and mixing on a microfluidic CD using 3D printed dual material inserts. Mixing and reciprocation enable improved detection reaching a lower LOD in a shorter amount of time. Generally, utilization of an elastic membrane in combination with an unvented air chamber allows for reciprocation at lower spin speeds, while utilizing a fluid filled chamber with an elastic membrane allows for a simpler design and a reduced footprint. Mixing was achieved through reciprocating flow through a 3D woven channel, and simulation showed the locations of the highest mixing efficiency within the channel.

While 3D printing is only appropriate for prototyping of CD inserts rather than mass manufacturing due to its sequential nature of producing parts, material jetting of a flexible and a rigid material can be used to model products before investing into a costly mold. Printed surfaces were fluidically evaluated as differences in surface properties need to be considered when utilizing a prototyping approach to correctly predict fluidic behavior of manufactured parts[107]. Surface finish of the printed parts not only impacts hydrophilicity and topography but also smallest possible dimensions with matte surface finish allowing for more accurate features while glossy surface finish yields higher hydrophilicity and better bonding with adhesives.

5. Electrochemistry on the CD

5.1. Basics of Electrochemical Sensing

5.1.1. Amperometry

Electrochemical detection as introduced in Section 2, relies on electron transfer between an analyte and an electrode surface. Generally, an electrochemical cell consists of 3 electrodes, namely working electrode, counter electrode, and reference electrode. The working electrode is the electrode of interest to analyze a charge transfer process. The counter or auxiliary electrode has a larger surface area than the working electrode as to not limit the charge transfer reaction and avoids any current from passing through the reference electrode, as this could change the potential of the latter. The reference electrode is ideal when its potential is well known and stable (nonpolarizable) and serves as potential reference for measurements. Potentials of reference electrodes are evaluated versus Standard Hydrogen Electrode (SHE) with assigned potential of 0V. [108]

In the case of amperometry the potential between working and reference electrode is stepped from zero to a positive or negative value and held constant throughout the measurement. The resulting current is measured as a function of time see Figure 29a). Initially a high current is observed as species in close proximity with the electrodes exchanges charges. Once these are consumed the current decreases to a steady state current with amplitude depending on mass transport kinetics. The Nernst Planck equation[108,109] describes the mass transfer to an electrode and is given in Equation 9 for one-dimensional mass transfer along the x-axis:

$$J(x) = -D\frac{\partial C(x)}{\partial x} - \frac{zF}{RT}DC\frac{\partial \Phi(x)}{\partial x} + Cv(x) \tag{9}$$

Where $J(x)$ is the flux of species, x the distance from the electrode surface, D diffusion coefficient, F Faraday's constant, R gas constant, T temperature, $\partial C(x)/\partial x$ the concentration gradient at distance x, $\partial \phi(x)/\partial x$ the potential gradient, z the charge of the species, C the bulk concentration of the species and v(x) a volume element velocity along x. The three terms on the right-hand side represent diffusion, migration, and convection respectively.

The most basic form of an electrochemical cell relies on diffusion only, while migration is avoided through addition of a salt and no convection is induced (no stirring or flow)[108]. Depending on the electronegativity of the analyte and the applied potential, electrons can either be released or adsorbed by the electrode surface. Therefore, measured current can be positive or negative in nature. In all amperometry experiments in this thesis the potential is stepped to -0.2V thus leading to electrons flowing from the electrode (cathode) to the analyte (i.e. in this work TMB^{+} + $e^{-} \rightarrow$ TMB; Ferricyanide$[Fe(CN)_6]^{3-}$ + $e^{-} \rightarrow$ Ferrocyanide $[Fe(CN)_6]^{4-}$) and inducing a current between working and counter electrode. Stirring of the solution or flow over the sensing surface of the electrode introduces convection, thus decreasing diffusion layer thickness and aids mass transport. Consequently, the current plateau increases (to more negative currents as shown in Figure 29a).

5.1.2. Cyclic Voltammetry

While amperometry is based on applying a potential step between the electrodes, in cyclic voltammetry the potential is ramped up and down within a chosen range. As in amperometry the resulting current is measured between working and counter electrode. A graphical illustration is shown in Figure 29b).

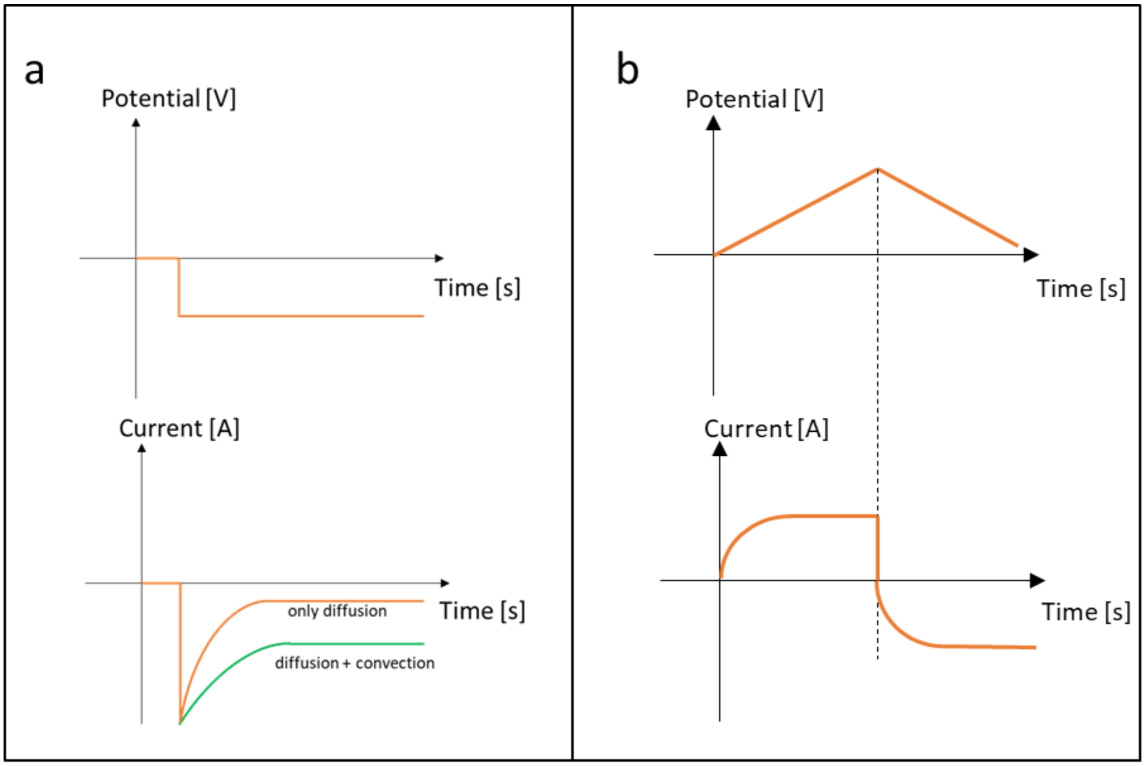

Figure 29: a) Amperometry: applied potential step and resulting current profile, b) Cyclic voltammetry: applied potential sweep and resulting current profile (at slow scan rates)

If the potential is increased quickly, a current peak can be observed (compare Figure 30, yellow curve). Throughout the increase in potential (forward scan) analyte at the electrode surface is consumed at increasing rate until charges are eventually depleted (peak). When no more analyte is available at the electrode surface to be reduced/oxidized, the current becomes mass transport limited as species has to be supplied from the bulk. Further increase of the potential leads to increase of the diffusion layer thickness and, therefore, constant current with amperage of the plateau depending on the mass transport rate. The same principle occurs during reverse scan. The faster the potential is raised and lowered the higher the peak, as less time is allowed for mass transport to occur while more charges are consumed per time. This can also be seen from Equation 10, the Randles-Sevcik equation[108,109]:

$$i_p = nFAC^0 (\frac{nFvD_0}{RT})^{\frac{1}{2}} \tag{10}$$

With i_p peak current, n number of electrons transferred, ν scan rate, A area of the electrode, C^0 bulk concentration of the analyte and D_0 diffusion coefficient of the consumed analyte[109]. Figure 30 shows the cyclic voltammogram for TMB$^+$(blue curve) and TMB^{2+} (yellow curve). The two peaks in TMB$^+$ graph indicate two separate electron transfer reactions, while TMB^{2+} only shows one peak for a single electron transfer reaction.

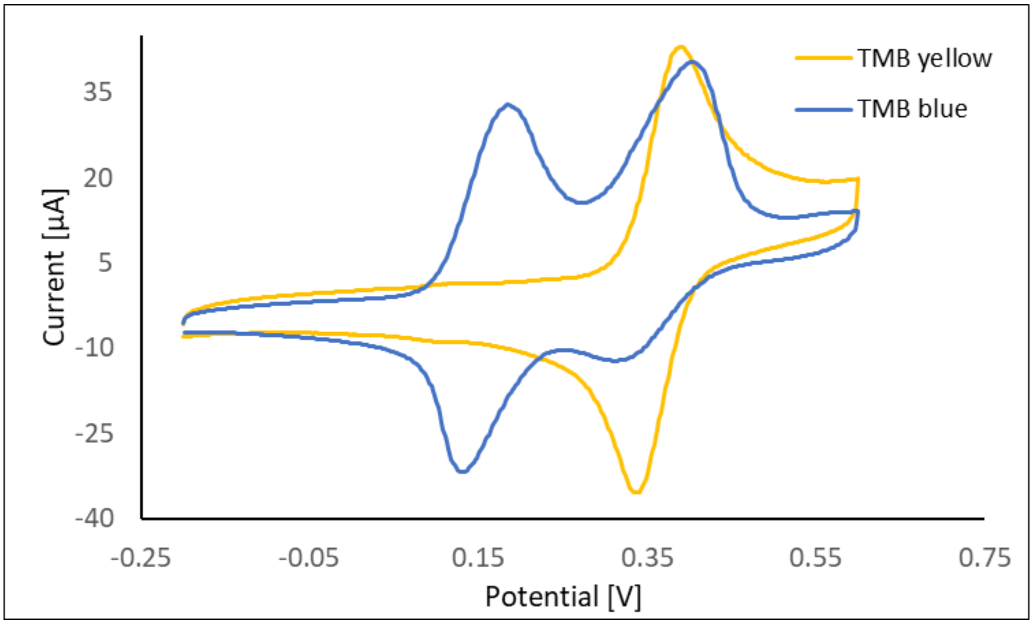

Figure 30: Cyclic Voltammogram of TMB, blue line shows two electron transfer (two peaks) of TMB$^+$(TMB blue) while the yellow curve shows one electron transfer voltammogram after adding stop solution to TMB$^+$, thus redox-cycling of TMB^{2+}(TMB yellow)

5.1.3. Microelectrodes

Advantage of electrochemical detection for microfluidics is ease of miniaturization. While optical detection methods require a minimum optical path length to provide sufficient performance[110], electrochemical sensors are easily miniaturized via advanced micromanufacturing techniques[111,112] and detection benefits from miniaturization[108].

This benefit is due to radial diffusion in electrodes with at least one dimension in the order of the diffusion layer thickness as opposed to planar diffusion when working with macroelectrodes (compare Figure 31 and Equation 11). The improved diffusion profile increases current density, allowing to reach steady state faster and enabling electrochemical kinetic measurements as well as highly accurate measurements in non-polar and resistive media[111]. Consequently, electrochemical detection is especially useful when working with very small fluid volumes.

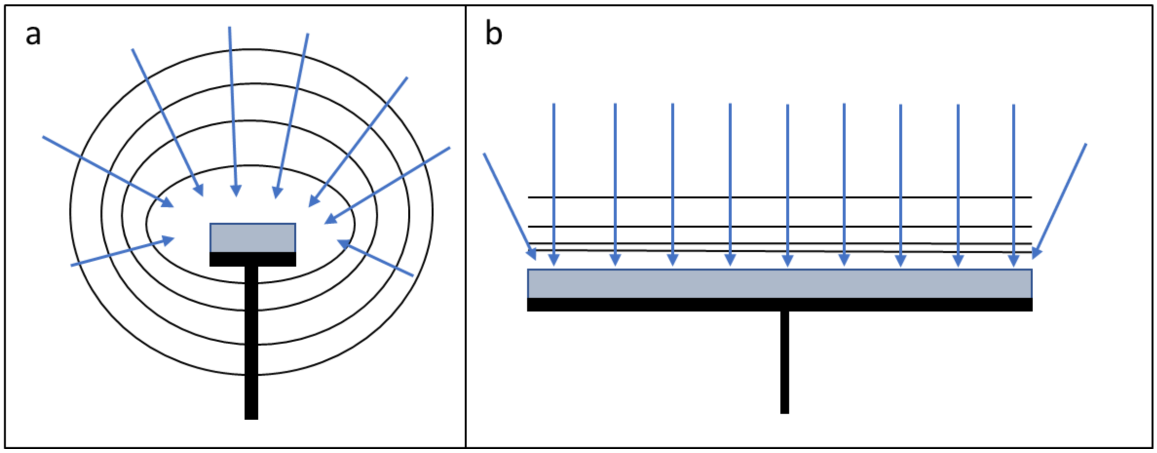

Figure 31: a) radial diffusion to a microelectrode, b) quasi planar diffusion to a macroelectrode, blue arrows indicate direction of diffusion, black lines areas of constant concentration.

$$i = \frac{nFA\sqrt{D_0 C_0^*}}{\sqrt{\pi}\sqrt{t}} + \frac{nFAD_0 C_0^*}{r_0} \tag{11}$$

Equation 11 describes the increase in current depending on relation of diffusion layer thickness D_0 and smallest electrode dimension r_0. In the case of a macroelectrode this relation is much smaller than 1 (electrode dimensions much larger than diffusion layer thickness) therefore the second term on the right-hand side is negligible and current only depends on the first term. If one electrode dimension is in the order of the diffusion layer thickness the second term contributes to the increase of current between analyte and electrode[108]. Because the diffusion layer only starts to grow once a potential is applied at the electrode, D_0 is initially very small and grows throughout forward scan in cyclic voltammetry or time of constant potential in amperometry. Therefore, the second term is especially relevant late in the experiment during steady state condition[108].

5.2. Effect of Flow on Electrochemical Signal

5.2.1. Introduction - Detection on CD Microfluidic Platform

Various detection methods have been employed on CD microfluidic platforms, usually based on optical, non-contact techniques, such as absorbance, fluorescence and chemiluminescence [113,114]. However, due to the proportionality of absorbance to optical path length most commercial absorbance-based systems are based on rather thick optical cells (equal or larger than 10mm) and not suitable for miniaturization[113]. Fluorescence and luminescence-based systems afford very good LODs but at the cost of complexity and size of the instrumentation[114]. Generally, optical detection methods also require stopping of the disc for readout and often even transportation of the disc to a different read-out device[113].

Without the need for optical grade materials or peripheral equipment with high electrical power demands, electrochemical detection affords for smaller, portable and lower cost diagnostic devices [113,115].

5.2.2. Background

5.2.2.1. Current Methods for Interfacing Electrodes on a Microfluidic CD

Similar to optical detection, electrochemical detection may require stopping of the disc for measurement in order to ensure electrical connectivity between the electrochemical sensors on the CD and a stationary instrument[116,117]. This spin-stop solution results in undesirable delays for time-sensitive experiments and cannot take advantage of the signal enhancement through flow. An electrochemical signal is indeed enhanced through increased mass transport of analyte towards the electrode surface. When mitigating unwanted migration via increased ionic concentration in the solution, only convection aids the otherwise purely diffusion-based mass transport of analyte to the electrodes. Increasing flow and thus convection leads to higher current signal and therefore lowers LOD and increases sensitivity[102].

In order to take advantage of flow over the electrodes, avoid delays or altered signal readouts, measurements need to be taken while the disc is spinning. This has been realized before through the use of a so-called slip-ring setup, allowing stationary contact pads to conduct electricity to and from a set of rotating rings spinning along with the rotating CD[102]. However, the physical contact induces significant electrical noise while wearing out components and thus gradually changing conductivity and resistance. An alternative has been demonstrated using a mercury based rotating electrical connector, inducing lower amounts of noise in the measurements during spinning of the disc[118]. However, this connection method is made up of a bulky setup and relies on rather expensive and undesirable mercury as the conducting and connecting substance. Rather than establishing electrical contact with the sensors on the disc, recently efforts have been made to develop wireless power and data connections. The first prototypes employing this approach demonstrate that the elimination of the physical interface reduces the electrical noise and increases the life-time of the device[119].

In this work, we aim to add to the relatively few examples of indirect interfacing methodologies by presenting a setup that integrates the analysis instrument, a bipotentiostat (allowing for simultaneous sensing of two working electrodes), to the spinning platform, powering it with a small battery and sending the obtained data via Bluetooth to a stationary desktop computer or mobile phone. Thus, rather than conducting the very low current signals to a stationary instrument, the obtained current signal is sent wirelessly as a binary code and is not affected by transmission errors and noise due to changing electrical contacts.

5.2.2.2. Redox Cycling Amplification using Interdigitated Microelectrode Arrays

While most of the efforts made in the field of electrochemical detection on a microfluidic CD have relied on the use of microelectrodes in a 3 electrode setup with a working electrode, reference electrode, and a counter electrode- so called single mode[102,116,117], here we use a 4 electrode setup utilizing 2 working electrodes besides a reference and a counter electrode- called dual mode. The working electrodes consist of sets of interdigitated electrode digits to further enhance the performance of the electrochemical detection. This type of electrode configuration is called an Interdigitated Electrode Array (IDA). IDAs allow for redox amplification (RA) of a measured signal by the redox cycling of a species between the interdigitated digits, in which a redox species is transported multiple times between the two sets of working electrodes before diffusing out into the bulk of the test solution. This amplification results in higher currents for a given concentration of analyte and therefore is capable of lowering the LOD[120]. The material choices and manufacturing means for IDAs vary and severely impact electrode cost, which especially for disposable systems is a major consideration.

Generally, RA has been demonstrated to significantly enhance the current signal and to decrease the LOD through an increase in sensitivity. Odijik et al. , for example, demonstrated an RA of over 2000 using a parallel plate setup with ferrocyanide as the redox-couple and Dam et al. showed an RA of 60-70 with high aspect ratio platinum IDAs with a width- gap- height of 2µm- 2µm- 7µm[121,122] . Even though very high RA factors might allow for the detection of very low concentrations and might be applicable to very small sample volumes, the question arises whether such measurements have actual analytical value as they do not relate the measured currents back to a bulk concentration of sample, but may increase error due to statistical distribution of particles in the solution, which would especially have an effect at very low concentrations. Working with a cell allowing for flow over the electrodes during the measurement allows for the supply of new species from the bulk of the solution thus providing for a fast coupling of transport between the fingers of the electrode sets and the bulk.

The effect of flow on the current signals in 3 and 4 electrode setups was described previously[102,111]. While the analytical current in a single mode setup benefits from flow enhanced mass transport, leading to a 7 fold increase under flow (500nL/s) compared to the no flow condition as demonstrated a study conducted by Kamath[111], dual mode currents show little enhancement under increasing flow. This phenomenon is explained by shearing off of the redox-species concentration profile through flow and therefore always hindering of the redox-species diffusing against the direction of the flow of reaching the other working electrode[120]. Kamath et al describe a drop in RA from 37 to 4 on carbon IDAs under flow (500nL/s) when compared to no flow[115]. Higher aspect ratio electrodes suffered less from the decrease in RA during flow which is explained by the lesser effect of the flow onto the redox-path of analyte between the digits of the electrodes rather than above them[111]. Besides RA, also the collection efficiency [CE=Collector current (one of the working electrodes) /Generator Current (the other working electrode)] can be used as a measure for characterization of redox cycling in dual mode.

Despite ample research in all three areas: diagnostics on a CD platform, flow enhanced electrochemical sensing and redox-amplification with IDAs, to the author's knowledge, no group has characterized the performance of IDAs in dual mode under flow conditions on a microfluidic CD nor have such measurements been transmitted wirelessly off the rotating platform.

5.2.3. Materials and Methods

5.2.3.1. Microfluidic Disc Design and Fabrication

Platinum IDAs consisting of 2 working electrodes, counter, and reference electrode and with digit widths and gaps of 3µm and electrode height of 90nm were purchased from CH Instruments Inc. and integrated onto the CD. Carbon IDAs were obtained through photolithography of SU8 and subsequent pyrolysis as described elsewhere[111]. The dimensions of the carbon IDA were identical to those of the platinum IDAs but with a height of 1.72µm and 70 digits per working electrode compared to 65 pairs for the platinum IDAs. A drop of Ag/AgCl was used on top of the platinum and carbon electrodes as pseudo reference electrode. The microfluidic disc and IDAs were assembled such, that the electrodes could be removed for cleaning (see Figure 32), which was essential for repeated usage of electrodes and discs for different and/or repeated experiments. The disc assembly consists (top to bottom) of a top adhesive layer sealing the chambers in an underlying PMMA disc, followed by another adhesive layer with microfluidic channels and another PMMA layer with through holes to provide flow to the electrodes. Between the latter PMMA layer and the electrodes a PDMS layer was placed with a channel perpendicular to the direction of the electrode digits and connecting the through holes while also exposing reference and counter electrodes. Finally, each electrode is held by a PMMA holder which is screwed to the microfluidic disc. Solutions were loaded into fill chambers and flown via the through hole into PDMS channels and onto the sensing area of the working electrodes. After returning via the other through hole in the disc fluid was collected in a waste chamber (see Figure 32).

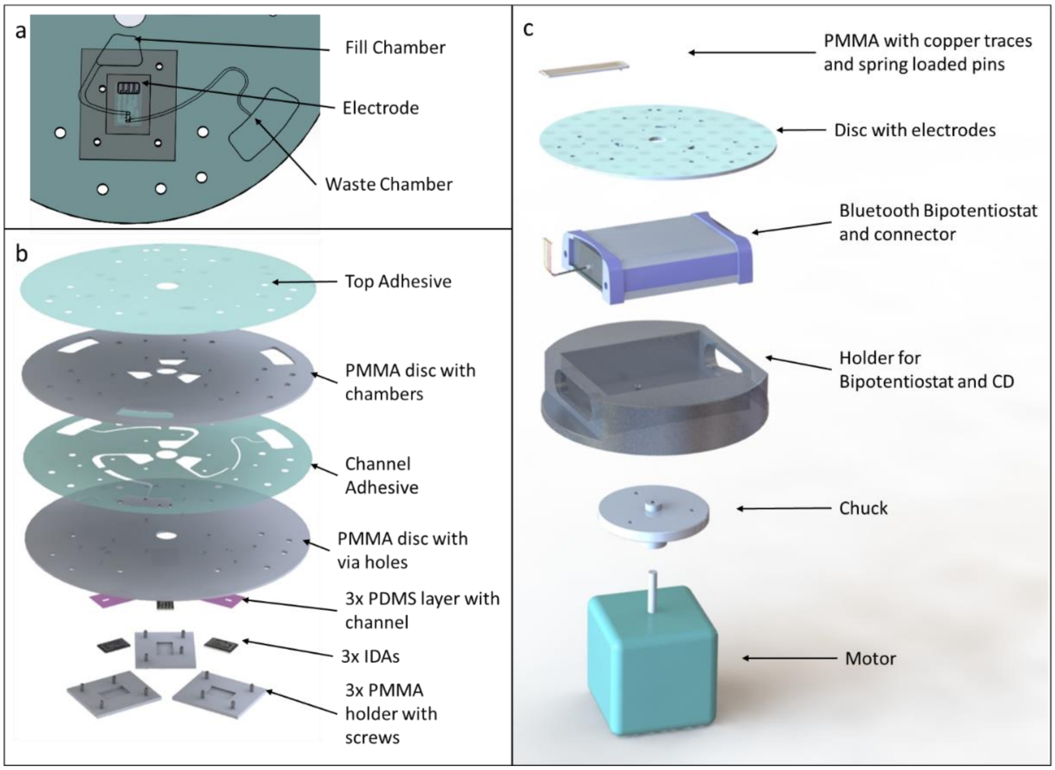

Figure 32: a) Fluidics on CD and positioning of the electrode underneath the disc, b) Assembly of modular CD. Electrodes can be removed for cleaning and replacement, c) Test setup for non-contact measurements

5.2.3.2. Setup for Rotating Electrochemical Measurements

A spin stand with motor (PMB21B-00114-00, Pacific Scientific, Co.) and controller (PC3403Ad-001-E, Pacific Scientific, Co.) was used for rotary actuation, while a trigger (D10DPFPQ, Banner Engineering, Corp.) was installed to trigger a high-speed camera (Area Scan A311fc, Basler AG) and a stroboscope (DT-311A, Nidec-Shimpo, Corp.) at each single rotation of the disc for visualization of the fluidics. This setup was used for the analysis of flow rates as well as for general control of fluidics (such as fill levels of the chambers).

A portable, battery powered bipotentiostat (µStat400, Metrohm DropSens AG) was purchased and controlled with the Dropiew 8400 software. To allow for integration of this instrument onto the spinning platform a holder was machined in which the bipotentiostat was placed and on top of which microfluidic discs could be mounted (see Figure 32c). The original DropSens cable was soldered to a connector consisting of a polymethylmethacrylate (PMMA) base with copper foil paths and spring-loaded gold pins for contacting the electrode bonding pads. Sensed data was sent via Bluetooth to a stationary computer for further analysis.

5.2.3.3.Procedures for Electrochemical Measurements

Solutions were prepared with 1mM, 3mM, 5mM, 7mM and 9mM ferricyanide, ferrocyanide redox-couple and a supporting electrolyte of 2M potassium chloride (KCl). One solution was prepared as blank (2M KCl) for measuring noise from the setup.

Platinum IDAs

For single mode operation, the potential was scanned from 0V to 0.6V in 0.002V steps at a scan rate of 0.02V/s. Dual mode was conducted using the same step size and scan rate with one working electrode scanned from 0.1V to 0.6V and the second working electrode kept constant at 0V. This scan rate leads to peak currents in no-flow and low RPM conditions due to the diffusion-limited mass transfer, while allowing for reaction limited currents at higher flow rates. Choosing a lower scan rate was not feasible as it did not allow for the completion of forward and backward scan with a maximum fill volume of 300µL.

Platinum electrodes were cleaned, once degradation in performance was observed. Cleaning of the Pt electrodes consisted of depositing a drop of 0.1N sulfuric acid solution on the sensing area of the Pt electrodes and conducting 20 cycles of cyclic voltammetry (CV) with sweep range from 0V to 1.5V at a scan rate of 0.1V/s. This procedure was followed by rinsing the IDA with distilled water and drying with filtered nitrogen. When subsequent control under microscope showed debris between the digits of the IDA, the interdigitated electrodes were carefully polished parallel to the digit direction with a gloved finger under flowing distilled water. Drying and control with a microscope was repeated until all the debris was removed.

Carbon Electrodes

Like platinum electrodes, carbon electrodes were utilized in single as well as dual mode. For single mode the best scan range was 0V to 0.5V. The scan rate in single as well as dual mode was 0.01V/s. Due to the lower conductivity of carbon as compared to platinum, the iR drop of carbon electrodes was higher. As the portable bipotentiostat did not allow for iR compensation, larger scan ranges were necessary to take full advantage of redox amplification when working with carbon electrodes. The dual mode curves for carbon electrodes were observed to approach a plateau around 1V (see Figure 33b) when scanning at 0.01V/s. However, such large scan ranges lead to the disintegration of the counter electrode and therefore to the reduction of the lifetime of the carbon electrode. To allow for the maximum sweep range and avoid early disintegration of the counter electrodes, the pH level of the solutions was measured and adjusted to a pH of 8 using sodium hydroxide. Nevertheless, to allow for an increased lifespan of the electrodes, sweep ranges in dual mode were limited to 0.1V to 0.6V for experiments on the CD. Due to the lower cost (about $5 per carbon electrode versus about $200 for a platinum electrode), carbon electrodes were replaced once signals started diverging rather than cleaned and used again. Due to the high iR drop and the lower stability of carbon IDAs in the required potential range, tests were limited to stationary testing with a single concentration (5mM). Taking all measurements (single and dual mode) on a single electrode was important as the PDMS channel, acting as shield in on disc measurements was manually positioned to only allow sensing area, counter, and reference electrodes to be exposed. Small changes in positioning as well as tightening of screws lead to changes of areas exposed to fluid and therefore to changes in currents.

5.2.3.1.Data Analysis

Single mode limiting currents were calculated with respect to the flow rate ν according to Bard et al.[108]:

$$i_L = 1.47nFC(DA/B)^{\frac{2}{3}}v^{\frac{1}{3}} \tag{12}$$

where n is the number of electrons transferred, F is Faraday's constant, C is the bulk concentration, D is the diffusion constant, A is the surface area of the electrodes and B the height of the channel. Therefore, flow is expected to increase with current as the cubic root until the reaction rate at the electrode surface becomes limiting.

Dual mode current without flow for different concentrations is calculated according to Aoki et al.[123] :

$$i = mbnFCD\left(0.637\, ln\left(\frac{2.55}{x}\right) - 0.19x^2\right) \tag{13}$$

With m the number of digits per working electrode, b the length of each digit and x the width of the digit divided by the width plus the gap. The diffusion constant of potassium ferri-ferrocyanide was assumed at 7.26E10-6cm^2/s[124].RA and CEs in dual mode under flow are expected to decrease with increasing flow rates due to shearing off of species[111,125]. Dual mode currents with flow at different concentrations were calculated according to the model by Morita et al[125].

Current voltage measurements (CVs) were obtained using Dropview 8400 software and analyzed with respect to the baseline of the respective curves. Such a baseline for each CV was established using a first order tangent based on 5 points in the linear area of each curve. RA and CE were calculated with RA= Limiting Current in Dual Mode/ Limiting Current in Single Mode and CE with: CE=Collector Current/ Generator Current. A calibration curve was established for each spin speed based on measurements of varying concentrations (i.e. 1mM, 3mM, 5mM, 7mM, 9mM at spin speeds of 0RPM, 100RPM, 200RPM, 300RPM, 400RPM respectively). The curves were quasi linear in the range of the tested solutions and the obtained slope equals the sensitivity at the respective spin speed. The LOD was calculated as 3 times the standard deviation of the CV for the blank solution in a range of 0.5V around the potential of the peak currents in solutions with the redox couple present. The standard deviation as well as the noise levels were measured using Origin 2018b (Originlab Corp.)

Oscillatory noise from spinning of the disc in the measured signal was removed utilizing Fast Fourier Transformation (FFT) Filtering.

5.2.4. Results and Discussion

5.2.4.1. Stationary Electrochemical Sensor Performance

First, stationary sensor performance was established in single and dual mode with a drop of 5mM ferri-ferrocyanide solution on platinum as well as on carbon IDAs. Potentials were measured versus Ag/AgCl. In Figure 32 we show the resulting CV curves for platinum a) and carbon b) electrodes. Measurements for both electrodes are summarized in Table 8. While with platinum IDAs the area of the working electrodes exposed to fluid is restricted to the interdigitated digits by a passivation layer added by the manufacturer, for carbon IDAs in the droplet experiment a small area of the traces between digits and bonding pads to the solution may be exposed to the solution as well. This adds to generally higher currents with carbon electrodes for droplet measurements as well as a CE of slightly larger 1 (due to unequal areas of the two working electrodes exposed to solution). It can be seen from Table 8 that carbon IDAs have a higher RA than platinum IDAs. This can be explained by the higher aspect ratio of the carbon IDAs compared to platinum IDAs. The higher aspect ratio of the carbon electrodes does not only increase the surface area for electron exchange but also decreases the diffusion path in a linear diffusion profile between electrode digits as compared to an elliptical diffusion profile atop of the electrode digits in the more planar Pt case[115]. In Table 8 we summarize the measurements depicted in Figure 32. It might be noted here that with different carbon electrode geometries carbon IDAs amplification factors of up to 38 were obtained. Predicted dual mode current (based on Equation 14) for platinum IDAs is in good agreement with the experiment, with calculated and experimental value respectively of 45.1μA and 37.7μA. This deviation seems to be largely within the variation when changing the setup (disassembly for cleaning of the electrode and subsequent reassembly) of the experiment. Additional possible reason for lower than calculated values in the experiments is described in the literature through contamination of the electrode surface [126].

Table 8: Stationary measurements in dual and single mode on platinum and carbon IDAs

Parameter	**Platinum IDA**	**Carbon IDA**
Single mode peak current	5.2μA	9.9μA
Generator current	37.7μA	165.5μA
Collector current	37.5μA	166.7μA
Redox amplification (with respect to peak current)	7.25	16.7
Collector Efficiency	0.99	1.0

In Figure 33c) and 33d) we show the CVs for platinum IDAs in stationary on disc measurements for various concentrations in single and dual mode respectively. For the dual mode graph, baselines were subtracted from measurements for better visualization of the current increase at higher concentration.

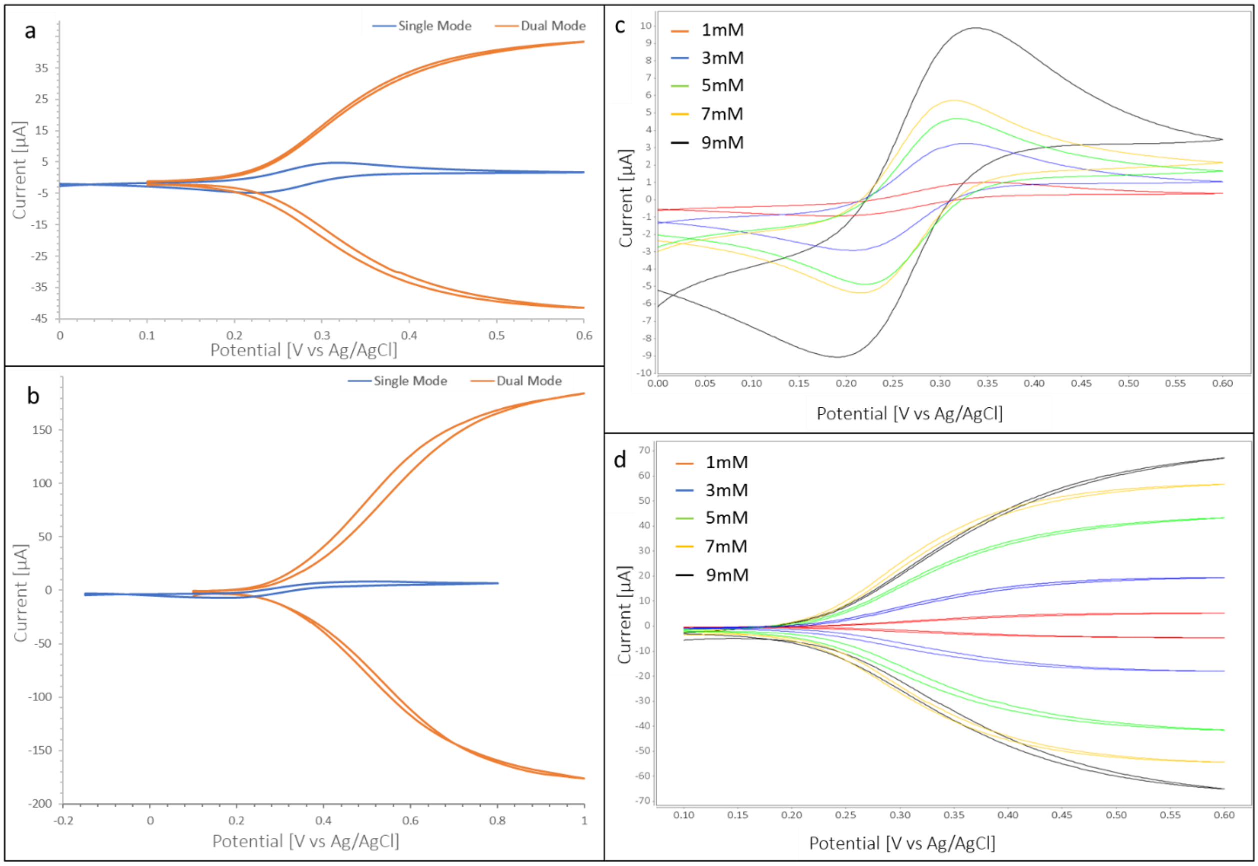

Figure 33: Single and dual mode CVs for a) Platinum IDA and b) carbon IDA, c) Single mode CV for platinum IDA with concentrations 1mM through 9mM ferricyanide, ferrocyanide redox-couple, d) Dual mode CV for platinum IDA with concentrations 1mM through 9mM ferricyanide, ferrocyanide redox-couple.

Based on the measurements shown in Figure 32 calibration curves for single and dual mode of platinum electrodes were obtained. These are shown in Figure 34. The sensitivity was calculated from the slope of calibration curve in Figure 34 as 0.39µA/mM and 6.7µA/mM for single and dual mode in stationary measurements respectively.

As can be seen from these values and Figure 34, the sensitivity for dual mode is higher than for single mode, thus affording lower LOD of 10.14nM in dual mode versus 63.51nM in single mode at 0RPM (based on average noise level of 21.5pA in measurement). Current measurements varied around 10% between setups which could be influenced by the manual alignment of the channel on the sensing area as well as manual adjustment of clamping pressure onto the silicone layer (leading to changes in width and height of the channel). Measurements within one setup showed only small standard deviations of less than 1% as can be seen in the error bars in Figure 34.

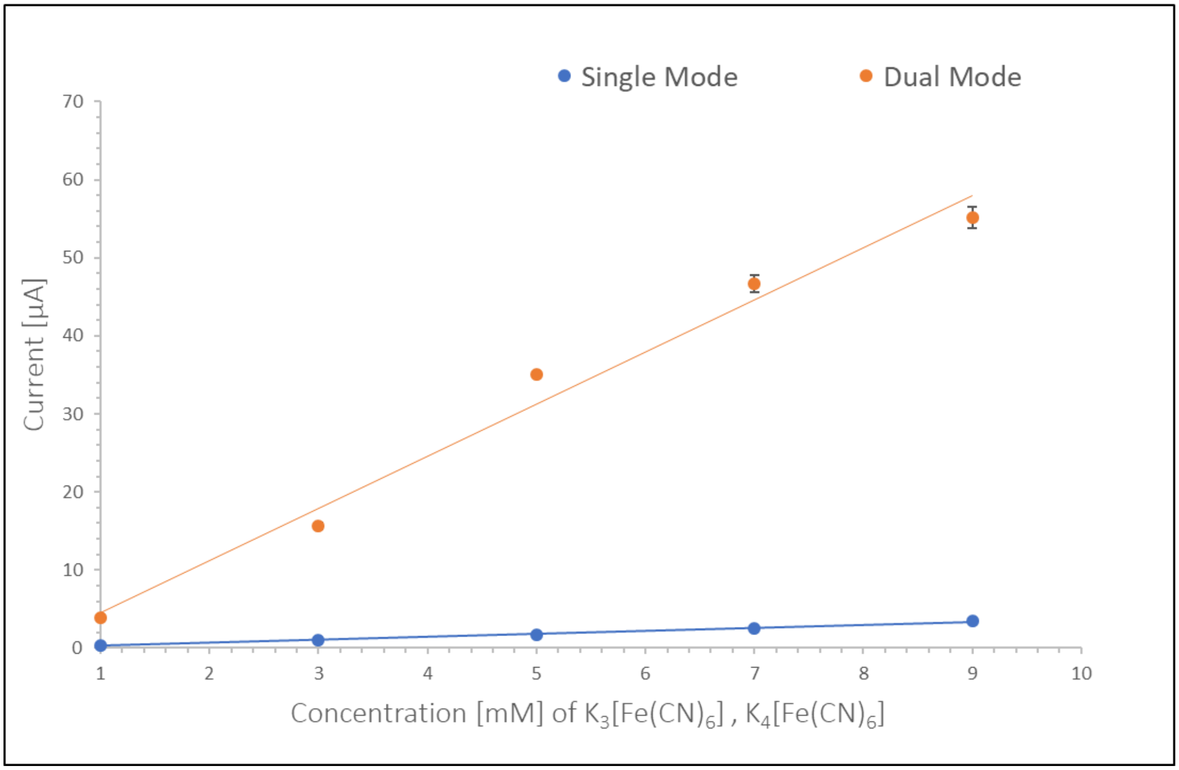

Figure 34: Calibration curve for single and dual mode, platinum IDA, stationary measurements

5.2.4.2. Effect of Flow Velocity on Redox Cycling

The effect of flow on the measured currents in single and dual mode can be seen in Figure 35a) and b) respectively. The graphs show the CV curves for 9mM ferri-ferrocyanide solution. It is observed from Figure 35a), that single mode CV moves from a diffusion limited curve with peak current to a current plateau. The dual mode curves Figure 35b) show less impact of flow on current but the current still increases with increasing flow.

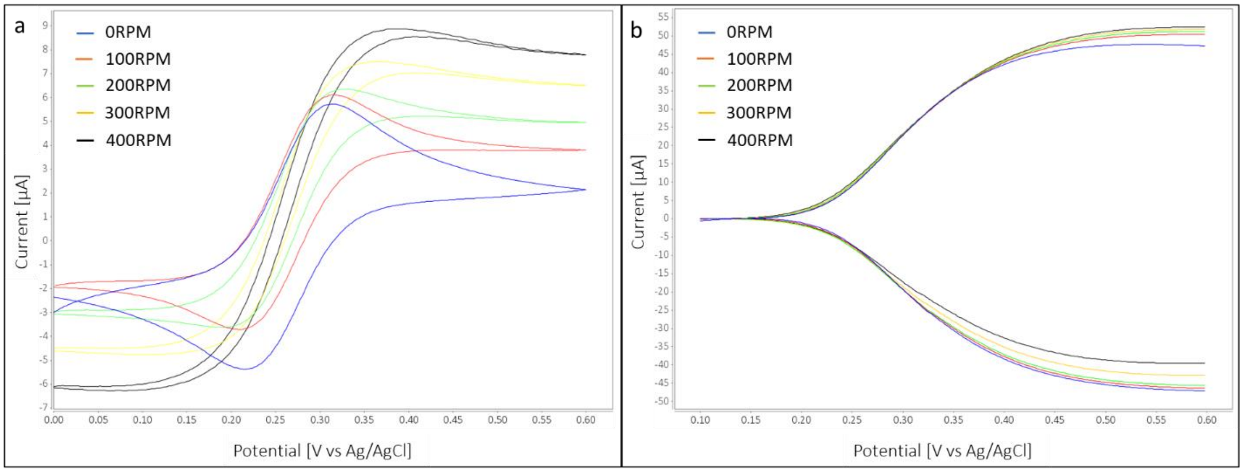

Figure 35: a) Single mode platinum IDA CV for increasing flowrates, b) Dual mode CV for platinum IDA for different flowrates. The baseline was subtracted from curves in dual mode for better visibility of the current increase with increasing flowrate

To allow for the calculation of single mode currents for different spin speeds, the flow rate at different spin frequencies was measured and results are shown in Figure 36a). Calculation (based on Equation 12) and experimental single mode currents were in very good agreement (Figure 36b)) and linear with $\nu^{\frac{1}{3}}$. In Figure 36c) we show the decrease of RA with respect to the limiting current from 16.2 to 4.6 and Figure 36d) shows the decrease in CE from 0.94 to 0.67 both with increasing flow rate. The RA and CE values are based on average measurements of all concentrations at the respective flow rates. This behavior is as expected as the increasing flow shears off redox species and precludes it from repeated redox cycling. Error bars in Figure 36 show standard deviations. In Figure 36b) error bars represent standard deviation of different measurements within the same setup.

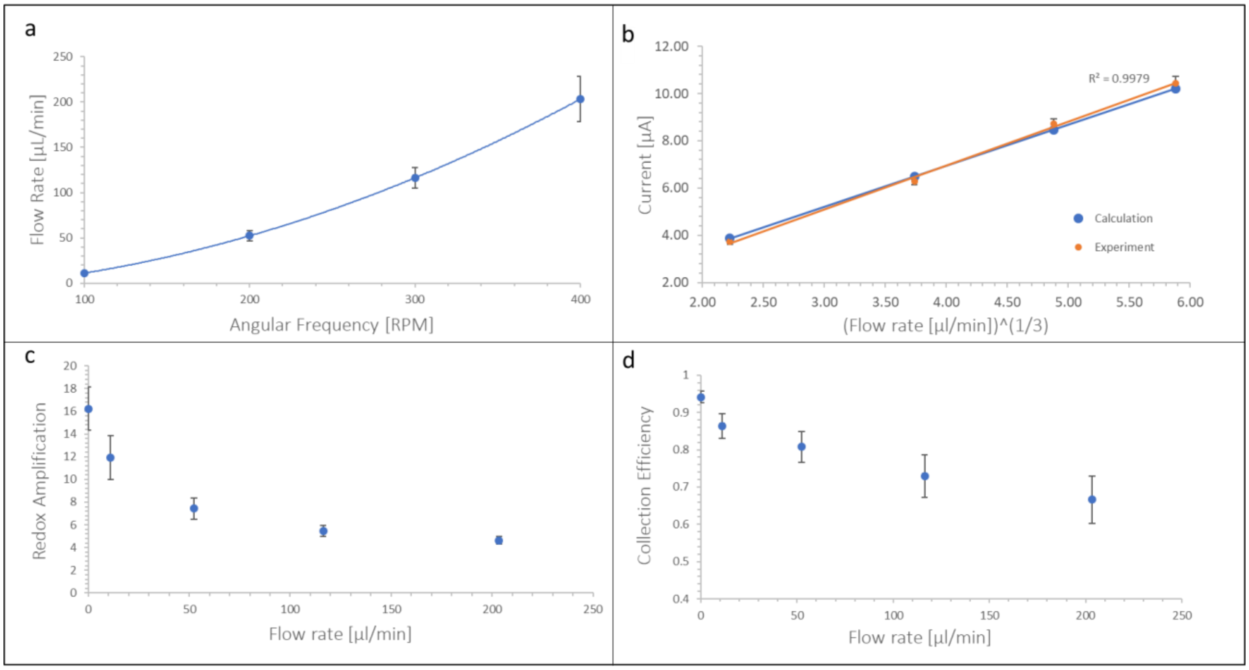

Figure 36: a) Relation between angular frequency and flow rate, b) Calculated (blue) and experimental Single Mode currents for increasing flow rate (platinum IDA), c) Measured RA versus flow rate (Platinum IDA), d) Measured CE versus flow rate (platinum IDA)

5.2.4.3.Flow-enhanced Electrochemical Sensor Performance

Despite a decreasing RA, the dual mode with flow affords the highest sensitivity of 6.99µA/mM and, in conjunction with average constant noise level (after FFT filtering of oscillatory noise from the rotation) of 21.5pA, leads to the lowest LOD of 9.23nM. Therefore, based on this study, dual mode CV with flow should be used for best electrochemical measurement performance at low concentrations (see Table 9). This is because even at higher than tested flowrates, dual mode limiting current will only eventually approach single mode limiting current but cannot result in lower currents. This is because once redox cycling is completely mitigated by flow, generator current will simply become single mode current. In CV measurements with very high scan rate, peak currents during stationary or slow flow measurements will increase and could lead to higher currents than the limiting current in dual mode. Fast CV experiments are however outside the scope of this work.

Table 9: Single versus dual mode sensitivities and LOD for platinum IDA under flow

`	**Single Mode**		**Dual Mode**	
Flow Rate [µL/min]	**Sensitivity [µA/mM]**	**LOD [nM]**	**Sensitivity [µA/mM]**	**LOD [nM]**
0.00	1.02	63.51	6.36	10.14
11.04	1.21	53.32	6.64	9.71
52.32	1.46	44.05	6.71	9.61
116.29	1.87	34.49	6.89	9.36
203.39	2.27	28.45	6.99	9.23

Table 10 shows a comparison of experimental and predicted dual mode currents with flow at a spin speed of 400RPM. Overall experimentally obtained currents are by a factor of 4.3 to 5.6 higher than predicted currents, which could be due to smaller than assumed channel geometry (height and width of channel depends on compression and thus deformation of PDMS layer) as well due to neglecting of species trapped between the digits of the electrodes, which are less affected by flow.

Table 10: Comparison of predicted and measured currents in dual mode at spin speed of 400RPM at various concentrations

	1mM	**3mM**	**5mM**	**7mM**	**9mM**
Predicted Current [µA]	1.34	4.02	6.70	9.38	12.06
Measurement [µA]	5.62	19.43	37.67	52.38	60.95

5.2.5. Conclusion

In this work we studied the effect of flow on redox amplification of platinum Interdigitated Electrode Arrays on a microfluidic disc and compared stationary currents obtained from carbon and platinum electrodes. A modular disc assembly allowed for cleaning and replacement of the electrodes. Cyclic Voltammetry measurements were conducted with a spinning bipotentiostat, placed underneath the fluidic disc, which was battery powered and transferred data via Bluetooth to a stationary computer, thus eliminating the need for physical contact to conduct data from the spinning electrodes to a stationary analysis device and therefore decreasing noise during measurements. Stationary cyclic voltammetry measurements were conducted on both, carbon and platinum Interdigitated Electrode Arrays, with carbon electrodes leading to higher currents and redox amplification, while being more affordable than platinum electrodes. However, platinum electrodes showed to be more stable throughout experiments and had less iR drop than carbon electrodes, therefore reaching steady state currents faster. Calibration curves for platinum electrodes in stationary measurements showed a higher sensitivity at 6.36µA/mM for dual mode as compared to 1.02μA/mM in single mode, leading to a lower limit of detection of 10.14nM in dual mode versus 63.51nM in single mode.

After imposing flow over the electrode surface and increasing flow rate to 5.88μL/min, a more than two-fold increase in sensitivity for single mode was observed while dual mode sensitivity increased less than 10% and redox amplification and collection efficiency decreased. Lowest limit of detection of 9.23nM was nevertheless obtained in dual mode at the highest tested flowrate. When targeting high sensitivity measurements this setup should therefore be chosen.

6. Demonstration of Malaria Assay on the CD

6.1. Integration of Sample-to-Answer Malaria-Assay on the CD

6.1.1. Assay Procedure

To demonstrate the electrochemical detection of a fully integrated assay for detection of malaria, a microfluidic CD was designed and a bioassay (Malaria-Ab ELISA, IBL International, Corp., Hamburg, Germany) was procured. The assay-kit includes the following components: Pre-coated wells, positive control, negative control, cut-off, malaria conjugate, TMB substrate, stop solution, and washing buffer. Because amperometric measurements were conducted with TMB blue (TMB^{+}), no stop solution was used on the CD. The procedure was integrated onto the CD with the following steps:

- incubation of 100μL controls (positive, negative, cut-off) on precoated well for 1h at 37°C,
- 2x 300μL washing of the well,
- transfer of 100μL malaria conjugate onto the well,
- incubation for 30min at room temperature,
- 2x 300μL washing of the well,
- transfer of 100μL TMB substrate,
- incubation for 15min at room temperature,
- flowing of the HRP-TMB reaction product at 44.5μl/min over the electrodes and amperometric measurement

For washing steps, the washing buffer was transferred into the well, then the disc was oscillated for 20 seconds at ±1 Hz/s, followed by flushing of the buffer towards the waste chamber. During the incubation steps, the disc was oscillated at ±1 Hz/s. To allow for low cost, disposable disc assemblies, commercial screen-printed carbon electrodes were chosen for single use application (DRP 110, Metrohm Dropsens, Asturias, Spain).

Off-the-disc experiments were conducted with the same steps directly in the break-apart well plate contained in the malaria kit and the resulting solutions were pipetted onto stationary electrodes of the same type as for on-disc experiments to conduct the amperometric measurements with potential stepped to -0.2V and evaluation of steady state current after 60s. Noise was filtered using Fast Fourier Transformation (FFT) filtering (Origin 2018b, Originlab Corp., USA).

6.1.2. Integration of the Assay Steps on the CD

Layers and Operation Principle of the CD

The CD assembly consists of two lasercut (Speedy 360, Trotec Laser Inc.,Austria), clear PMMA layers (Mc Master-Carr Supply Co., Santa Fe Springs, Ca, USA) containing chambers, etched channels (the channel over electrode is 0.1mm deep, all other channels are 0.5mm deep, 1mm wide) as well as etched areas for electrode placement. These layers (top and bottom PMMA disc) are bonded together with a black double-sided adhesive and the assembly is sealed with two clear adhesives on top and bottom (see Figure 37). Bonding of the discs via black adhesive allows for the use of a laser to open connecting channels by melting a hole into the black adhesive layer while leaving the rest of the disc intact. The principle of the laser valve is described in Section 4.2 and was chosen in conjunction with a burst valve between well and waste to increase the reliability of fluidic performance[107]. To initiate the opening of a valve, a current and voltage of 0.7A and 3.8V were applied and a 445nm 4.75W laser was focused via a 400nm-470nm Glass Lens (both from Shenzhen

Newgazer Technology Co., Ltd., Guangdong, China) from a distance of approximately 1.6cm. The layered disc assembly is shown in Figure 37a). Electrodes for the disc design presented in this work were non-removable to avoid contamination. Choice of screen-printed carbon electrodes allows to keep this solution affordable. In commercial systems electrodes could be directly printed onto the thermoplastic disc[127,128]. The utilized test setup is described elsewhere[35]. Additional components are an IR lamp for heating during incubation and a portable DC power supply.

Disc Layout

Figure 37b) shows a photograph of the disc with chambers filled with colored water for better visualization. The disc layout allows for processing of three samples in parallel on the same disc. Each of these three structures consists of two chambers for washing buffer (see blue in Figure 37b) with two outlets each at different heights. Opening the upper valve for a first washing step and the lower valve of the same washing chamber for a second washing step enables dual step washing from the same chamber and decreases the real estate for washing buffer on the disc. Chambers shown in yellow and red in the same figure contain malaria conjugate and TMB buffer respectively. The green chamber contains a single break-apart well from the utilized malaria kit. This chamber has two channels exiting. The first channel is separated from the chamber via a burst valve (constriction in channel to 0.1mm widths) and leads through a serpentine channel to the waste chamber (channel on the right). The second channel is protected with a laser valve during assay procedure and only opened once the assay is ready for the detection step. It then allows liquid to flow over the sensing surface of the electrode towards the second waste chamber (left in Figure 37b). The shape of the chamber containing the electrode together with the serpentine channel allows to keep entire sensing surface in contact with liquid during sensing and increases the available time for measurement. Holes above the sensing chamber allow for access to contact pads of the electrodes. Figure 38 illustrates fluidic steps on the CD.

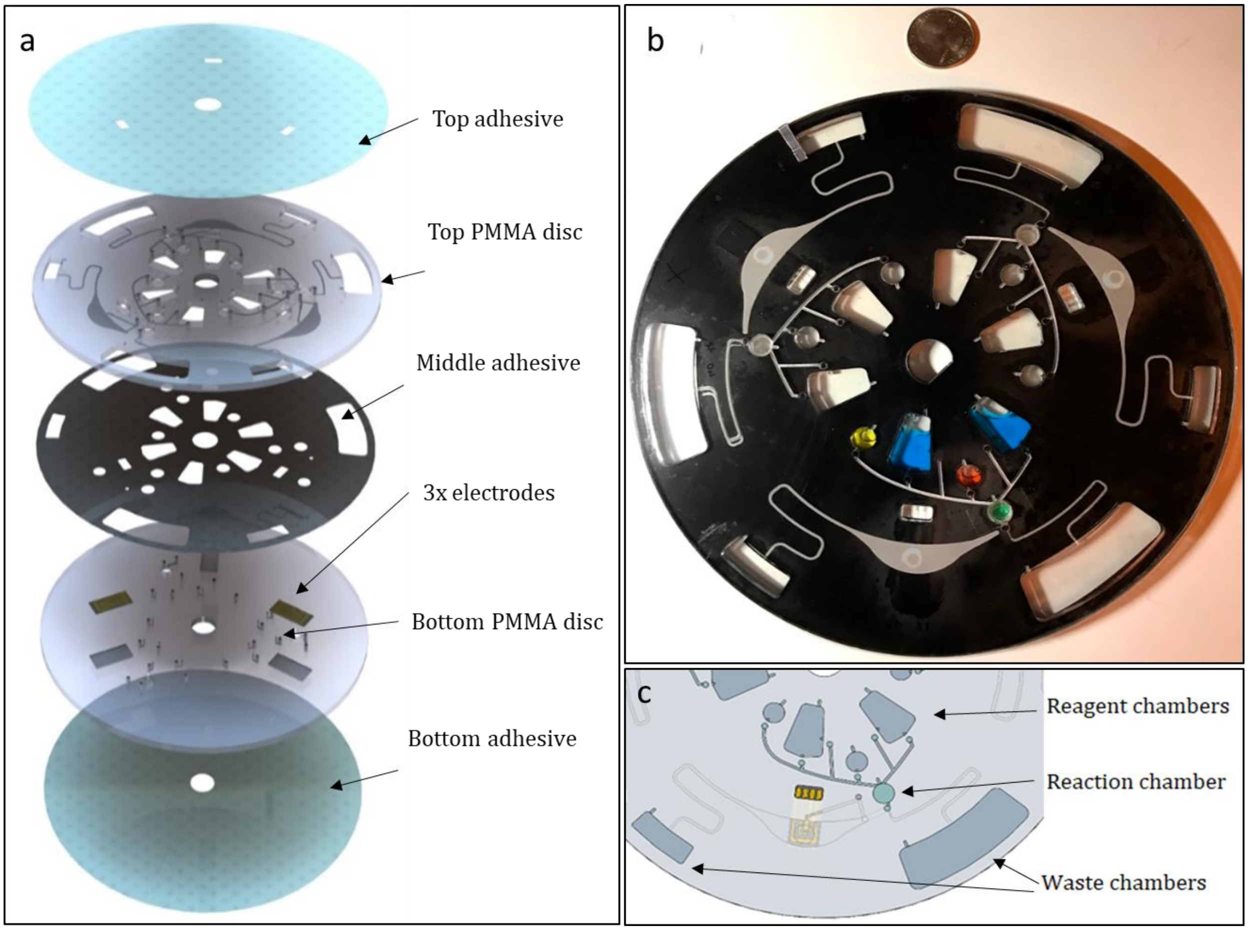

Figure 37: a) Disc assembly with black adhesive layer to enable use of laser valves, b) assembled disc with dyed water in reagent chambers (green is reaction chamber with break apart, pre-coated detection well), c) model of disc layout.

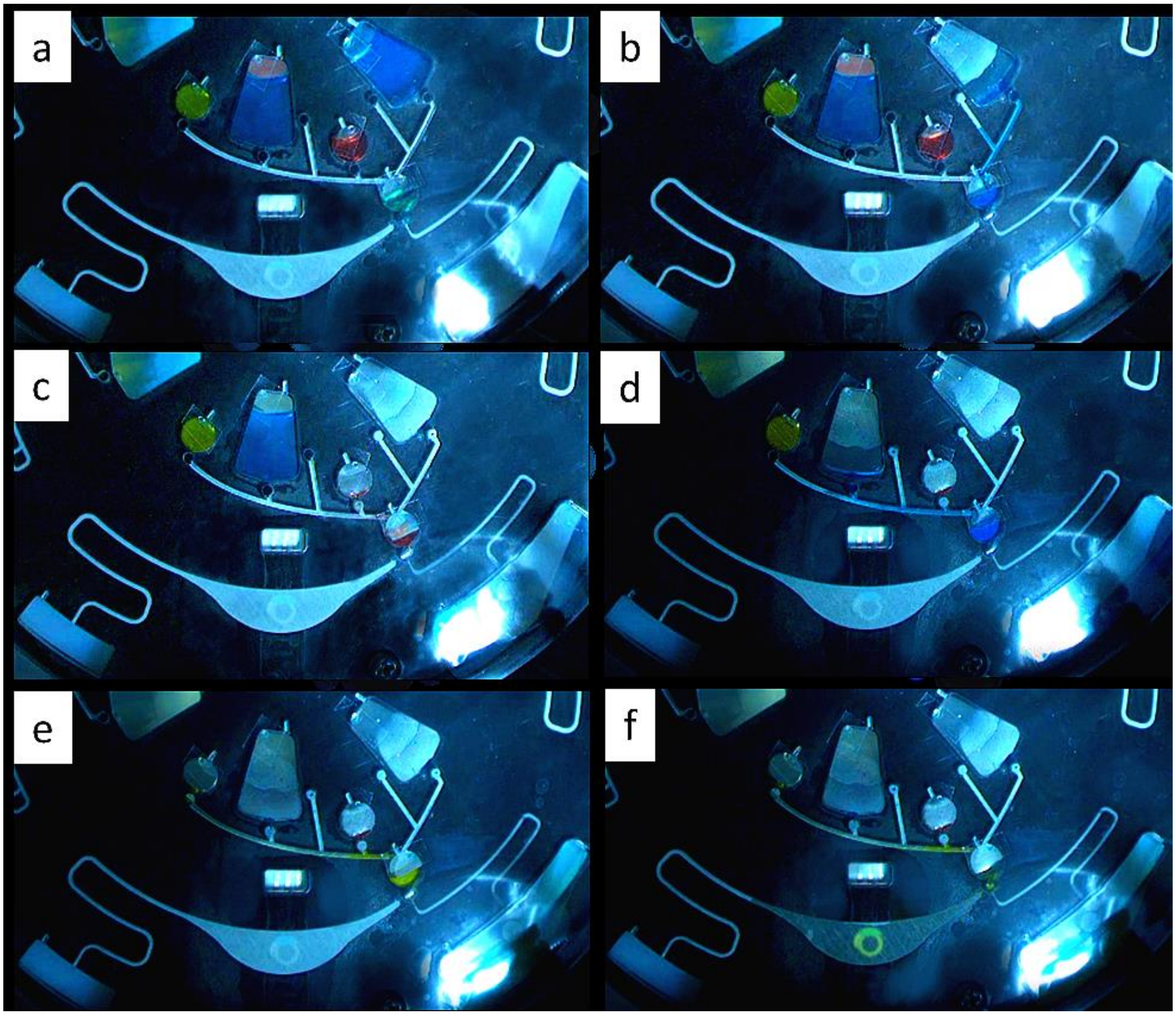

Figure 38: High speed images of critical steps: a) sample incubation, b) first wash, c) incubation of malaria conjugate (primary antibody), d) second wash, e) incubation TMB substrate, f) electrochemical detection during flow

6.2. Results and Discussion

Figure 39a) shows amperometric results when detecting positive, cut-off and negative controls (as contained in the malaria kit) on the disc. It also shows the signal obtained when no control is used (skipping of step 1 in the protocol), this is considered the blank. Figure 39b) illustrates results obtained in experiments on and off disc. Higher currents on disc are due to convection, specifically measurement during flow[35] and enhanced mixing through oscillation of the disc during incubation steps. While amperometric detection yielded highest LOD according to our initial comparison to absorbance and electrochemiluminescence, possible means for increased sensitivity and reduced LOD are flow and, if utilizing a 4-electrode setup, redox-amplification[35].

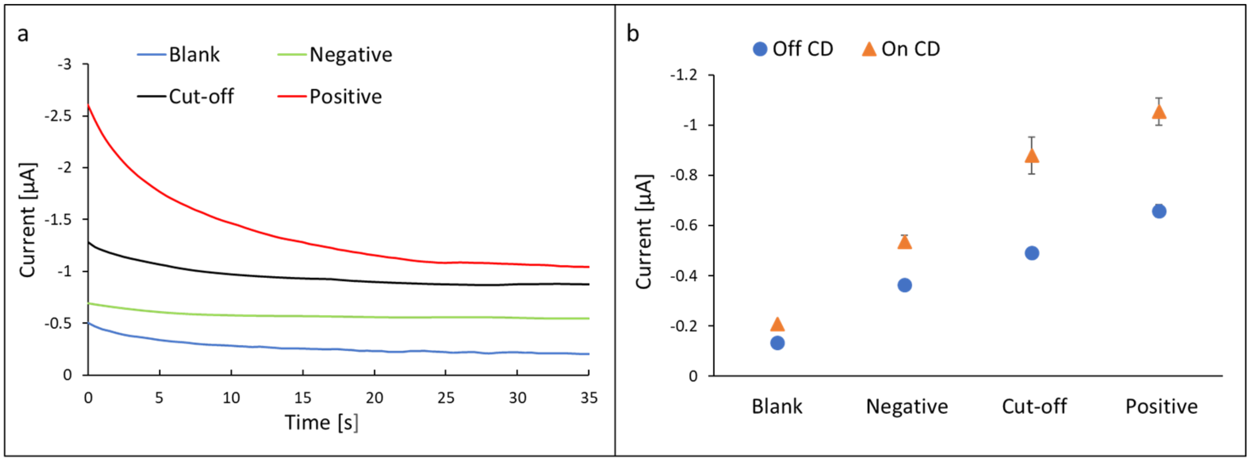

Figure 39: a) On disc amperometric results for blank, negative control, cut-of control, and positive control, b) comparison of on disc and off the disc currents

The diagnostic device can affect precision of a diagnostic result depending on how reproducibly the fluidic steps are implemented. With a CV of 11.7% on the disc versus 7.8% off the disc, integration on the spinning platform with electrochemical detection only slightly increased imprecisions. This is especially true when comparing to significant influence of user related variability[129]. When comparing off disc experimental data with HRP detection study using amperometry (with the same electrodes, bipotentiostat and sample volume) discussed in Section 2, it can be seen that assay steps contribute to detection imprecision. The averaged measured current of -0.658μA obtained through performing assay related steps (as recommended by the assay supplier) relates to a HRP concentration of 1.65E-05mg/mL when detected directly through amperometry as described in Section 2.3.3. Comparing CV for HRP detection at this level to the assay CV shows a much lower CV for direct HRP detection at 2.2% as compared to 7.8% for the off disc assay. This increase in CV can be attributed to additional pipetting steps, possibly incomplete washing, and standard deviations in crosslinking of antigen/antibody. Also additional chemistries may affect the electrochemical readings. Table 11 shows a summary of CVs for different levels of assay integration.

Table 11: CV for different assay integration levels

Method for detection of approx. 1.65E-05 mg/mL HRP	**CV [%]**
HRP detection through TMB amperometry	2.2
Assay procedure and HRP detection through TMB amperometry	7.8
On disc assay procedure and HRP detection through TMB amperometry	11.7

Finally, the specific circumstances in which the detection method will be employed need to dictate detection technology and additional considerations such as substrates, incubation times, flow- or redox-amplification enhanced electrochemical detection can further optimize performance of electrochemical detection[35]. Such circumstances include range of expected concentrations, time to answer, cost of disposable and instrument, environmental conditions and end-user. When trying to achieve a very reproducible assay performance steps should be considered separately.

7. Conclusions

This thesis discusses and compares different detection methods and means of integration on automated, microfluidic platforms to address challenges in bringing diagnostics to patients in POC settings. While malaria was chosen as an example for detection methods and diagnostic platforms, general results apply to various other diseases and health conditions. The choice of detection method and assay integration must depend on the specific situation. Consider the following scenario: a patient in a *developed country* suffers from chest pain and calls 911, First responders arrive at the scene and need to start the diagnostic process immediately as acute coronary syndrome (ACS) is suspected and any delay in treatment may lead to further complications for the patient[4]. A portable diagnostic device (e.g. placed in the ambulance) with very low LOD and extremetly fast time to answer is needed to allow for diagnosis by the time the patient arrives at the hospital, so that the appropriate treatment may start immediately. In this case only low levels of biomarker would be expected (*limited DR sufficient*), *very low LOD* is required due to the short time since suspected obstruction of oxygen supply to heart muscle tissue, wherefore only low levels of biomarker of interest have been released. *Cost* in this case would *not be restrictive* due to criticality of event and level of income/public healthcare system in the country of occurance. Although environmental conditions require *shock and vibration resistance* of the diagnostic device to driving, temperature and air quality are likely in a normal range and electricity may be reliably supplied from the vehicle. Any disposables containing reagents can be stored at required temperature setting prior to usage. According to the comparison of three different detection methods for the label HRP in this thesis, chemiluminescence would be most suitible in this case due to its very low LOD, sufficient DR and very fast time to answer, while cost of optical components and controlled environmental settings would not prohibit employment of this technique. Integration into a CD microfluidic system is sufficiently vibration resistant (compare CD player in cars) for regular driving. A portable, commercial CD microfluidic platform for detection of Troponin I is indeed in use in emergency departments[130].

In another scenario, which has been described in detail in this thesis, infectious diseases such as malaria need to be diagnosed in *resource limited* areas. Diagnosis is needed during the *same visit* at the physicians office to allow for treatment of the underlying cause while avoiding contribution to increasing drug resistance issues caused by overtreatment. While a *wide range of concentrations* is expected, *affordability* of the diagnosis is essential. In this case, besides simple RDTs which only provide limited sensitivity, electrochemical detection may be most appropriate as according to studies introduced in this thesis it allows for widest DR. Utilization of *low cost electrodes*, possibly directly printed on disposable platforms can make this technology affordable. Miniaturized electrodes furthermore allow for increased sensitivity, while decreasing required sample volume, possibly allowing for *simple finger prick test* without the need for a trained phlebotomist. Also in this case CD microfluidics can enhance success of diagnostic procedure, by fully automizing all fluidic steps, allowing multiplexed air bubble free and flow enhanced electrochemical measurement. Especially susceptibility of optical components to sand, dust and humidity may prohibit optical detection methods. Generally reagent storage is challenging in environments with extreme humidity and temperature conditions. Besides sophisticated reagent storage of liquids in containers such as glass capsules[66] or aluminum pouches[131], valving and lyophilization, and/or utilization of an absorbent storage medium (e.g. sponge[132]) of reagents can contribute to address this challenge.

For microfluidic diagnostics, valving is essential to allow for acurate control over fluidics. While burst valves are inherently simple to integrate as they only rely on cross-section or surface changes and do not need external instruments, extensive analysis demonstrated limitations when using burst valves for commercial microfluidics. To allow for cost efficient, complex and robust microfluidic systems, combination with other passive valves, e.g. (multi-)siphon valve or with active valves is suggested. Active valves such as laser valves, which completely seal a chamber from vapor and liquid, not only allow for a highly reliable fluid release, but can also enable reagent storage in high humidity settings.

For research settings or when low numbers of automated fluidic platforms are needed 3D printing can allow for affordable fabrication. Integration with basic electronics such as servomotors, heating elements and lightning was demonstrated to successfully automate a qualitative malaria bioassay. When utilizing fused deposition modelling, leakage control is critical to avoid (cross-) contamination. Different post processing steps such as solvent treatment or surface coatings were characterized and discussed. Another 3D printing method, which was utilized to produce reciprocation inserts for CD microfluidics is material jetting. Parts produced with this technology are slightly more costly than those obtained from FDM systems but did not show issues with leakage. Furthermore, this technology allows for combination of rigid and elastic materials within the same part, which can not ony allow for enhanced fluidic functionality, but also allows to model overmolded part without the need for costly mold. Generally 3D printing can enable complex fluidic structures while reducing manufacturing and assembly steps to a minimum.

Combination of electrochemical detection and sophisticated fluidic systems can drastically enhance sensitivity and lower LOD. This was demonstrated on a CD microfluidic platform utilizing redox amplification and enhanced mass transport to the electrode through flow. While flow generally loweres collection efficiency and thus makes redox amplification less efficient, lowest LOD demonstrated for the ferricyanide/ferrocyanide redox couple was obtained through a combination of flow and employment of redox amplification. While tests used platinum electrodes due to high reliability of results, low cost carbon IDAs obtained through pyrolisis of a polymer precursor (SU-8) make integration of redox amplification in POC diagnostics more affordable. Further research could address robustness of carbon electrodes, and redox amplification efficiency. The latter could for example be addressed through increasing surface area in height direction (i.e. adding post structures on the otherwise mostly planar electrodes). Extension of electrodes into height direction (perpendicular to flow) may also decrease the current reducing effect of shearing off of redox species through flow.

Finally for true multiplexing on an electrochemistry based CD, a lightweight, possibly inductive powered bipotentiostat is needed, which can spin with the disc to reduce noise and which allows for sequential or synchronous detection of species from mltiple electrodes.

REFERENCES

1. Point of Care Diagnostics/Testing Market Size, Share & Trends Analysis Report by Product (Glucose, Blood Gas/Electrolytes, Cancer Marker), By End Use (Clinic, Hospital), And Segment Forecasts, 2019 - 2025. 252 (2019). Available at: https://www.researchandmarkets.com/reports/4479669/point-of-care-diagnosticstesting-market-size?utm_source=BW&utm_medium=PressRelease&utm_code=j9rglr&utm_campaign=1236970+-+Global+Point+of+Care+Diagnostics%2FTesting+Market+Size%2C+Share+%26+Trends+Analysi. (Accessed: 13th June 2019)
2. Bissonnette, L. & Bergeron, M. G. The GenePOC Platform, a Rational Solution for Extreme Point-of-Care Testing. *Micromachines* **7**, (2016).
3. Tiffany Bailey Lash. NIH Fact Sheets - Point-of-Care Diagnostic Testing. Available at: https://report.nih.gov/NIHfactsheets/ViewFactSheet.aspx?csid=112. (Accessed: 16th June 2019)
4. (UK), N. C. G. C. for A. and C. C. *Chest Pain of Recent Onset*. *Chest Pain of Recent Onset: Assessment and Diagnosis of Recent Onset Chest Pain or Discomfort of Suspected Cardiac Origin* (Royal College of Physicians (UK), 2010).
5. Hudson, M. P., Christenson, R. H., Newby, L. K., Kaplan, A. L. & Ohman, E. M. Cardiac markers: point of care testing. *Clin. Chim. Acta.* **284**, 223–37 (1999).
6. Health Organization, W. *World Malaria Report 2018*.
7. Koch, A., Cox, H. & Mizrahi, V. Drug-resistant tuberculosis: challenges and

opportunities for diagnosis and treatment. *Curr. Opin. Pharmacol.* **42**, 7–15 (2018).

8. Shah, N. S. *et al.* Transmission of Extensively Drug-Resistant Tuberculosis in South Africa. *N. Engl. J. Med.* **376**, 243–253 (2017).
9. Wellems, T. E. *et al.* Genetic mapping of the chloroquine-resistance locus on Plasmodium falciparum chromosome 7. *Proc. Natl. Acad. Sci. U. S. A.* **88**, 3382–6 (1991).
10. Wellems, T. E. & Plowe, C. V. Chloroquine-Resistant Malaria. *J. Infect. Dis.* **184**, 770–776 (2001).
11. Natalie Slivinski. A New Era of Malaria Drug Resistance? | RealClearScience. (2019).
12. Bloland, P. B. *Drug resistance in malaria*. (2001).
13. Hastings, I. M., Watkins, W. M. & White, N. J. The evolution of drug-resistant malaria: the role of drug elimination half-life. doi:10.1098/rstb.2001.1036
14. Bill Brieger. Asymptomatic Malaria – we need to eliminate what we can't see. (2019). Available at: http://www.globalhealthhub.org/2019/01/30/asymptomatic-malaria-we-need-to-eliminate-what-we-cant-see/. (Accessed: 16th June 2019)
15. Oladosu, O. O. & Oyibo, W. A. Overdiagnosis and Overtreatment of Malaria in Children That Presented with Fever in Lagos, Nigeria. *ISRN Infect. Dis.* **2013**, 1–6 (2013).
16. Singh, H. *et al.* High sensitivity, high surface area Enzyme-linked Immunosorbent Assay (ELISA). *Biomed. Mater. Eng.* **26**, 115–127 (2015).
17. Lawn, S. D., Kerkhoff, A. D., Vogt, M. & Wood, R. Diagnostic accuracy of a low-cost, urine antigen, point-of-care screening assay for HIV-associated pulmonary tuberculosis before antiretroviral therapy: a descriptive study. *Lancet. Infect. Dis.* **12**, 201–9 (2012).

18. Parsons, L. M. *et al.* Laboratory Diagnosis of Tuberculosis in Resource-Poor Countries: Challenges and Opportunities. *Clin. Microbiol. Rev.* **24**, 314–350 (2011).

19. Kosack, C. S., Page, A.-L. & Klatser, P. R. A guide to aid the selection of diagnostic tests. *Bull World Heal. Organ* (2017). doi:10.2471/BLT.16.187468

20. García-Basteiro, A. L. *et al.* Point of care diagnostics for tuberculosis. *Pulmonology* **24**, 73–85 (2018).

21. Horizon Scanning Report. *Point-of-care tests for malaria — NIHR Community Healthcare MIC*. (2015).

22. Berzosa, P. *et al.* Comparison of three diagnostic methods (microscopy, RDT, and PCR) for the detection of malaria parasites in representative samples from Equatorial Guinea. *Malar. J.* **17**, 333 (2018).

23. Fanjul-Bolado, P., González-García, M. B. & Costa-García, A. Amperometric detection in TMB/HRP-based assays. *Anal. Bioanal. Chem.* **382**, 297–302 (2005).

24. Virel, A., Saa, L., Köster, S. D. & Pavlov, V. Ultrasensitive optical detection of hydrogen peroxide by triggered activation of horseradish peroxidase. *Analyst* **135**, 2291 (2010).

25. Veitch, N. C. Horseradish peroxidase: a modern view of a classic enzyme. *Phytochemistry* **65**, 249–259 (2004).

26. Lee, A.-C. *et al.* Sensitive electrochemical detection of horseradish peroxidase at disposable screen-printed carbon electrode. *Electroanalysis* **20**, 2040 (2008).

27. Zhao, Y.-D., Zhang, W.-D., Chen, H., Luo, Q.-M. & Li, S. F. Y. Direct electrochemistry of horseradish peroxidase at carbon nanotube powder microelectrode. *Sensors Actuators B Chem.* **87**, 168–172 (2002).

28. Yi, X., Huang-Xian, J. & Hong-Yuan, C. Direct Electrochemistry of Horseradish Peroxidase Immobilized on a Colloid/Cysteamine-Modified Gold Electrode. *Anal. Biochem.* **278**, 22–28 (2000).

29. Ferri, T., Poscia, A. & Santucci, R. Direct electrochemistry of membrane-entrapped horseradish peroxidase.: Part I. A voltammetric and spectroscopic study. *Bioelectrochemistry Bioenerg.* **44**, 177–181 (1998).

30. David Josephygg, P., Elingg, T. & Mason1, R. P. *The Horseradish Peroxidase-catalyzed Oxidation of 3,5,3′,5′-Tetramethylbenzidine FREE RADICAL AND CHARGE-TRANSFER COMPLEX INTERMEDIATES**. *THE JOURNAL OF BIOLOGICAL CHEMISTRY* **257**, (1982).

31. Stefan, L., Denat, F. & Monchaud, D. Insights into how nucleotide supplements enhance the peroxidase-mimicking DNAzyme activity of the G-quadruplex/hemin system. *Nucleic Acids Res.* **40**, 8759 (2012).

32. Stefan, L., Xu, H.-J., Gros, C. P., Denat, F. & Monchaud, D. Harnessing Nature's Insights: Synthetic Small Molecules with Peroxidase-Mimicking DNAzyme Properties. *Chem. - A Eur. J.* **17**, 10857–10862 (2011).

33. Yang, L. *et al.* Study on Enhancement Principle and Stabilization for the Luminol-H2O2-HRP Chemiluminescence System. *PLoS One* **10**, e0131193 (2015).

34. Nelson, W. D. & Opperman, G. *Detection, Detection, Detection: Considerations for Enzyme/Substrate Selection in Immunoassay Development Contact Information Figure 1: Model Immunoassay System Figure 4: Lower Limit of Detection-Analytical Sensitivity*.

35. Bauer, M., Bartoli, J., Martinez-Chapa, S. O. & Madou, M. Wireless Electrochemical Detection on a Microfluidic Compact Disc (CD) and Evaluation of Redox-Amplification

during Flow. *Micromachines* **10**, (2019).

36. *Evaluation of Detection Capability for Clinical Laboratory Measurement Procedures; Approved Guideline-Second Edition*. (2012).

37. Jung, W., Han, J., Choi, J. W. & Ahn, C. H. Point-of-care testing (POCT) diagnostic systems using microfluidic lab-on-a-chip technologies. *Microelectron. Eng.* **132**, 46–57 (2015).

38. Figeys, D. & Pinto, D. Lab-on-a-Chip: A Revolution in Biological and Medical Sciences. *Anal. Chem.* (2000).

39. Haeberle, S. & Zengerle, R. Microfluidic platforms for lab-on-a-chip applications. *Lab Chip* (2007). doi:10.1039/b706364b

40. S.A.B. Hermsen, B. Roszek, A.W. van Drongelen & R.E. Geertsma. Lab-on-a-chip devices for clinical diagnostics, Measuring into a new dimension. *Natl. Inst. Public Heal. Environ. RIVM Rep.* **080116001/**, (2013).

41. Rajeevan, M. S. Immunoassays versus Molecular Diagnostics: Who has the upper hand? *Frost&Sullivan Mark. Insight* (2006).

42. Liao, S. C. *et al.* Smart cup: A minimally-instrumented, smartphone-based point-of-care molecular diagnostic device. *Sensors Actuators, B Chem.* **229**, 232–238 (2016).

43. Liu, C. *et al.* An isothermal amplification reactor with an integrated isolation membrane for point-of-care detection of infectious diseases. *Analyst* **136**, 2069 (2011).

44. Liu, C. *et al.* Membrane-Based, Sedimentation-Assisted Plasma Separator for Point-of-Care Applications. *Anal. Chem.* **85**, 10463–10470 (2013).

45. Chin, C. D. *et al.* Microfluidics-based diagnostics of infectious diseases in the

developing world. *Nat. Med.* **17**, 1015–1019 (2011).

46. Verpoorte, E. & De Rooij, N. F. Microfluidics Meets MEMS. in (2003). doi:10.1109/JPROC.2003.813570

47. Gross, B. C. *et al.* Evaluation of 3D Printing and Its Potential Impact on Biotechnology and the Chemical Sciences. *Anal. Chem.* (2014). doi:10.1021/ac403397r

48. Ubide, S. C., Waldbaur, A., Rapp, H., L€ Ange, K. & Rapp, B. E. Let there be chip—towards rapid prototyping of microfluidic devices: one-step manufacturing processes. *Anal. Methods Pages Anal. Methods* **33121**, 2663–2954 (2011).

49. Waheed, S. *et al.* 3D printed microfluidic devices: enablers and barriers. *Lab Chip* **16**, 1993–2013 (2016).

50. Cotteleer, M. J. 3D opportunity: Additive manufacturing paths to performance, innovation, and growth. in *Additive Manufacturing Syposium* (2014).

51. Lipson, H. & Kurman, M. *Fabricated : the new world of 3D printing*. (2012).

52. Stedtfeld, R. D. *et al.* Gene-Z: a device for point of care genetic testing using a smartphone. (2012). doi:10.1039/c2lc21226a

53. Erkal, J. L. *et al.* 3D printed microfluidic devices with integrated versatile and reusable electrodes. *Lab Chip* **14**, 2023–2032 (2014).

54. Boubekri, N. & Alqahtani, M. Economics of Additive Manufacturing. *Int'l J. Adv. Mech. Automob. Engg.* **2**, (2015).

55. Gibson, I., Rosen, D. & Stucker, B. *Additive Manufacturing Technologies 3D Printing, Rapid Prototyping, and Direct Digital Manufacturing*. (2010).

56. Wong, K. V. & Hernandez, A. A Review of Additive Manufacturing. *ISRN Mech. Eng.*

2012, 1–10 (2012).

57. Lewis, J. A. & Gratson, G. M. Direct writing in three dimensions. *Mater. Today* **7**, 32–39 (2004).

58. Kadimisetty, K. *et al.* 3D-printed supercapacitor-powered electrochemiluminescent protein immunoarray. *Biosens. Bioelectron.* **77**, 188–193 (2016).

59. Berg, B. *et al.* Cellphone-Based Hand-Held Microplate Reader for Point-of-Care Testing of Enzyme-Linked Immunosorbent Assays. *ACS Nano* **9**, 7857–7866 (2015).

60. Nayak, S., Blumenfeld, N. R., Laksanasopin, T. & Sia, S. K. Point-of-Care Diagnostics: Recent Developments in a Connected Age. *Syst. Integr. Chem.* (2017). doi:10.1021/acs.analchem.6b04630

61. Iwai, K. *et al.* Finger-powered microfluidic systems using multilayer soft lithography and injection molding processes. *Lab Chip* **14**, 3790 (2014).

62. Amazon.com: TowerPro SG90 9G Mini Servo with Accessories: Toys & Games. Available at: https://www.amazon.com/TowerPro-SG90-Mini-Servo-Accessories/dp/B001CFUBN8/ref=sr_1_fkmr0_2?s=toys-and-games&ie=UTF8&qid=1515114742&sr=1-2-fkmr0&keywords=TowerPro+SG90+Micro+Servos+and+HS-5645MG+Digital+High+Torque+Servo+Motor. (Accessed: 4th January 2018)

63. Bauer, M. & Kulinsky, L. Fabrication of a Lab-on-Chip Device Using Material Extrusion (3D Printing) and Demonstration via Malaria-Ab ELISA. *Micromachines* **9**, 27 (2018).

64. Salentijn, G. I., Oomen, P. E., Grajewski, M. & Verpoorte, E. Fused Deposition Modeling 3D Printing for (Bio)analytical Device Fabrication: Procedures, Materials, and

Applications. *Anal. Chem.* **89**, 7053–7061 (2017).

65. van Oordt, T., Barb, Y., Smetana, J., Zengerle, R. & von Stetten, F. Miniature stick-packaging – an industrial technology for pre-storage and release of reagents in lab-on-a-chip systems. *Lab Chip* **13**, 2888 (2013).

66. Hoffmann, J., Mark, D., Lutz, S., Zengerle, R. & von Stetten, F. Pre-storage of liquid reagents in glass ampoules for DNA extraction on a fully integrated lab-on-a-chip cartridge. *Lab Chip* **10**, 1480 (2010).

67. Ota, H. *et al.* Application of 3D Printing for Smart Objects with Embedded Electronic Sensors and Systems. *Adv. Mater. Technol.* (2016). doi:10.1002/admt.201600013

68. Melnikova, R., Ehrmann, A. & Finsterbusch, K. 3D printing of textile-based structures by Fused Deposition Modelling (FDM) with different polymer materials. *IOP Conf. Ser. Mater. Sci. Eng.* **62**, 012018 (2014).

69. Siegrist, J., Egis Peytavi, R. ´ & Madou, M. *Microfluidics for biological analysis: Triumphs and hurdles of CD platforms*.

70. Al-Faqheri, W. *et al.* Vacuum/Compression Valving (VCV) Using Parrafin-Wax on a Centrifugal Microfluidic CD Platform. *PLoS One* **8**, e58523 (2013).

71. Siegrist, J. *et al.* Serial siphon valving for centrifugal microfluidic platforms. *Microfluid. Nanofluidics* **9**, 55–63 (2010).

72. Carpentras, D., Kulinsky, L. & Madou, M. A Novel Magnetic Active Valve for Lab-on-CD Technology. *J. Microelectromechanical Syst.* **24**, 1322–1330 (2015).

73. Amasia, M. & Madou, M. Large-volume centrifugal microfluidic device for blood plasma separation. *Bioanalysis* **2**, 1701–1710 (2010).

74. Kido, H. *et al.* A novel, compact disk-like centrifugal microfluidics system for cell lysis and sample homogenization. *Colloids Surfaces B Biointerfaces* **58**, 44–51 (2007).

75. Kuo, J.-N. & Li, B.-S. Lab-on-CD microfluidic platform for rapid separation and mixing of plasma from whole blood. *Biomed. Microdevices* **16**, 549–558 (2014).

76. Sayad, A. A. *et al.* A microfluidic lab-on-a-disc integrated loop mediated isothermal amplification for foodborne pathogen detection. *Sensors Actuators B Chem.* **227**, 600–609 (2016).

77. Sundberg, S. O., Wittwer, C. T., Gao, C. & Gale, B. K. Spinning Disk Platform for Microfluidic Digital Polymerase Chain Reaction. doi:10.1021/ac902398c

78. Madou, M. *et al.* LAB ON A CD. *Annu. Rev. Biomed. Eng.* **8**, 601–628 (2006).

79. Rahmanian, O. D. & DeVoe, D. L. Single-use thermoplastic microfluidic burst valves enabling on-chip reagent storage. *Microfluid. Nanofluidics* **18**, 1045–1053 (2015).

80. Oh, K. W. & Ahn, C. H. A review of microvalves. *J. Micromechanics Microengineering* **16**, R13–R39 (2006).

81. Au, A. K., Lai, H., Utela, B. R. & Folch, A. Microvalves and Micropumps for BioMEMS †. *Micromachines* **2**, 179–220 (2011).

82. Cho, H., Kim, H.-Y., Kang, J. Y. & Kim, T. S. How the capillary burst microvalve works. *J. Colloid Interface Sci.* **306**, 379–385 (2007).

83. Chen, J. M., Huang, P.-C. & Lin, M.-G. Analysis and experiment of capillary valves for microfluidics on a rotating disk. *Microfluid. Nanofluidics* **4**, 427–437 (2008).

84. Glière, A. & Delattre, C. Modeling and fabrication of capillary stop valves for planar microfluidic systems. *Sensors Actuators, A Phys.* **130–131**, 601–608 (2006).

85. Zeng, J., Deshpande, M., Greiner, K. B. & Gilbert, J. R. FLUIDIC CAPACITANCE MODEL OF CAPILLARY-DRIVEN STOP VALVES. *ASME* (2000).

86. Kazemzadeh, A., Ganesan, P., Ibrahim, F., He, S. & Madou, M. J. The Effect of Contact Angles and Capillary Dimensions on the Burst Frequency of Super Hydrophilic and Hydrophilic Centrifugal Microfluidic Platforms, a CFD Study. *PLoS One* **8**, (2013).

87. Lu, C. *et al.* New Valve and Bonding Designs for Microfluidic Biochips Containing Proteins. *Anal. Chem.* (2007). doi:10.1021/ac0615798

88. Man, P. F., Mastrangelo, C. H., Burns, M. A. & Burke, D. T. Microfabricated capillarity-driven stop valve and sample injector. in *Proceedings MEMS 98. IEEE. Eleventh Annual International Workshop on Micro Electro Mechanical Systems. An Investigation of Micro Structures, Sensors, Actuators, Machines and Systems (Cat. No.98CH36176)* 45–50 (IEEE, 1998). doi:10.1109/MEMSYS.1998.659727

89. Yildirim, E. Modeling and Analysis of a Microfluidic Capillary Valve. *J. Polytech.* **20**, 487–494 (2017).

90. Korhonen, J. T., Huhtamäki, T., Ikkala, O. & Ras, R. H. A. Reliable Measurement of the Receding Contact Angle. *Langmuir* **29**, 3858–3863 (2013).

91. Murakami, D., Jinnai, H. & Takahara, A. Wetting Transition from the Cassie–Baxter State to the Wenzel State on Textured Polymer Surfaces. *Am. Chem. Soc.* (2014). doi:10.1021/la4049067

92. Giacomello, A., Meloni, S., Chinappi, M. & Casciola, C. M. Cassie–Baxter and Wenzel States on a Nanostructured Surface: Phase Diagram, Metastabilities, and Transition Mechanism by Atomistic Free Energy Calculations. *Langmuir* **28**, 10764–10772

(2012).

93. Busscher, H. J., van Pelt, A. W. J., de Boer, P., de Jong, H. P. & Arends, J. The effect of surface roughening of polymers on measured contact angles of liquids. *Colloids and Surfaces* **9**, 319–331 (1984).

94. Bormashenko, E. *et al.* Contact Angle Hysteresis on Polymer Substrates Established with Various Experimental Techniques, Its Interpretation, and Quantitative Characterization. *Langmuir* **24**, 4020–4025 (2008).

95. Strohmeier, O. *et al.* Centrifugal microfluidic platforms: advanced unit operations and applications. *Chem. Soc. Rev.* **44**, 6187–6229 (2015).

96. Garcia-Cordero, J. L. *et al.* Optically addressable single-use microfluidic valves by laser printer lithography †. doi:10.1039/c004980h

97. Li, C., Dong, X., Qin, J. & Lin, B. Rapid nanoliter DNA hybridization based on reciprocating flow on a compact disk microfluidic device. *Anal. Chim. Acta* **640**, 93–99 (2009).

98. Noroozi, Z. *et al.* Reciprocating flow-based centrifugal microfluidics mixer. *Rev. Sci. Instrum.* **80**, 075102 (2009).

99. Aeinehvand, M. M. *et al.* Latex micro-balloon pumping in centrifugal microfluidic platforms. *Lab Chip* **14**, 988–97 (2014).

100. Thio, T. H. G. *et al.* Push pull microfluidics on a multi-level 3D CD. *Lab Chip* **13**, 3199–209 (2013).

101. Noroozi, Z. *et al.* A multiplexed immunoassay system based upon reciprocating centrifugal microfluidics. *Rev. Sci. Instrum.* **82**, 064303 (2011).

102. Kim, T.-H. *et al.* Flow-enhanced electrochemical immunosensors on centrifugal microfluidic platforms. *Lab Chip* **13**, 3747 (2013).

103. Chou, J. *et al.* Effects of sample delivery on analyte capture in porous bead sensors. *Lab Chip* **12**, 5249–56 (2012).

104. Abi-Samra, K. *et al.* Thermo-pneumatic pumping in centrifugal microfluidic platforms. *Microfluid. Nanofluidics* **11**, 643–652 (2011).

105. Noroozi, Z., Kido, H. & Madou, M. J. Electrolysis-Induced Pneumatic Pressure for Control of Liquids in a Centrifugal System. *J. Electrochem. Soc.* **158**, P130 (2011).

106. Slesarenko, V. & Rudykh, S. *Towards mechanical characterization of soft digital materials for multimaterial 3D-printing*.

107. Bauer, M. *et al.* Burst valves for commercial microfluidics: a critical analysis. *Microfluid. Nanofluidics* **23**, 86 (2019).

108. Bard, A. J., Faulkner, L. R. & Wiley, J. *ELECTROCHEMICAL METHODS Fundamentals and Applications*. (John Wiley & Sons Inc, 2001).

109. Elgrishi, N. N. *et al.* A Practical Beginner's Guide to Cyclic Voltammetry. (2017). doi:10.1021/acs.jchemed.7b00361

110. Lampinen, J., Raitio, M., Perälä, A., Oranen, H. & Harinen, R.-R. *Microplate Based Pathlength Correction Method for Photometric DNA Quantifi cation Assay*.

111. Kamath, R. *Ultra-sensitive carbon interdigitated electrode arrays for redox amplification*.

112. Matysik, F.-M. Miniaturization of electroanalytical systems. *Anal. Bioanal. Chem.* **375**, 33–35 (2003).

113. Burger, R., Amato, L. & Boisen, A. Detection methods for centrifugal microfluidic platforms. *Biosens. Bioelectron.* **76**, 54–67 (2016).

114. Gilmore, J. *et al.* Challenges in the Use of Compact Disc-Based Centrifugal Microfluidics for Healthcare Diagnostics at the Extreme Point of Care. *Micromachines* **7**, 52 (2016).

115. Kamath, R. R. & Madou, M. J. Three-Dimensional Carbon Interdigitated Electrode Arrays for Redox-Amplification. *Anal. Chem.* **86**, 2963–2971 (2014).

116. Nwankire, C. E. *et al.* Label-free impedance detection of cancer cells from whole blood on an integrated centrifugal microfluidic platform. *Biosens. Bioelectron.* (2016). doi:10.1016/j.bios.2014.12.049

117. Li, T., Fan, Y., Cheng, Y. & Yang, J. An electrochemical Lab-on-a-CD system for parallel whole blood analysis. *Lab Chip* **13**, 2634 (2013).

118. Andreasen, S. Z. *et al.* Integrating electrochemical detection with centrifugal microfluidics for real-time and fully automated sample testing. *RSC Adv.* **5**, 17187–17193 (2015).

119. Torres Delgado, S. M., Korvink, J. G. & Mager, D. The eLoaD platform endows centrifugal microfluidics with on-disc power and communication. *Biosens. Bioelectron.* **117**, 464–473 (2018).

120. Kamath, R. & Madou, M. J. Selective Detection of Dopamine against Ascorbic Acid Interference Using 3D Carbon Interdigitated Electrode Arrays. *ECS Trans.* **61**, 65–73 (2014).

121. Dam, V. A. T., Olthuis, W. & van den Berg, A. Redox cycling with facing interdigitated array electrodes as a method for selective detection of redox species. *Analyst* **132**, 365

(2007).

122. Odijk, M., Straver, M., Olthuis, W. & Berg, A. van den. Microfluidic sensor for ultra high redox cycling amplification for highly selective electrochemical measurements. in *15th International Conference on Miniaturized Systems for Chemistry and Life Sciences* 1281–1283 (Chemical and Biological Micro Systems Society, 2011).

123. Aoki, K. *Approximate models of interdigitated array electrodes for evaluating steady-state currents*. *J. Electroanal. Chem* **284**, (1990).

124. Konopka, S. J., McDuffie, B., Arvia, A. J., Bazan, J. C. & W Carrozza, J. S. *Polarographic Techniques*. *J. Amer. Chem. Soc* **10**, (1929).

125. Morita, M., Niwa, O. & Horiuchi, T. *Interdigitated array microelectrodes as electrochemical sensors*. *Electrochimica Ado* **42**, (1997).

126. Goldstein, E. L. & Van de Mark, M. R. Electrode cleaning and anion effects on ks for K3Fe(CN)6 couple. *Electrochim. Acta* **27**, 1079–1085 (1982).

127. Economou, A., Kokkinos, C. & Prodromidis, M. Flexible plastic, paper and textile lab-on-a chip platforms for electrochemical biosensing. *Lab Chip* **18**, 1812–1830 (2018).

128. da Silva, E. T. S. G., Miserere, S., Kubota, L. T. & Merkoçi, A. Simple On-Plastic/Paper Inkjet-Printed Solid-State Ag/AgCl Pseudoreference Electrode. *Anal. Chem.* **86**, 10531–10534 (2014).

129. Okorodudu, A. O. Optimizing Accuracy and Precision for Point-of-Care Tests. *Point Care J. Near-Patient Test. Technol.* **11**, 26–29 (2012).

130. Nexus Dx. IB10 sphingotest® Troponin-99 | Nexus-Dx. Available at: https://www.nexus-dx.com/ib10-sphingotest-troponin-99/. (Accessed: 7th July

2019)

131. Smith, S. *et al.* Blister pouches for effective reagent storage on microfluidic chips for blood cell counting Blister pouches for effective reagent storage on microfluidic chips for blood cell counting microfluidic chips, with an example application area being point-of-care diagnostics. **20**, 163 (2016).

132. Tang, R. *et al.* Paper-based device with on-chip reagent storage for rapid extraction of DNA from biological samples. *Microchim. Acta* **184**, 2141–2150 (2017).